



UNIVERSIDAD DE CONCEPCIÓN
FACULTAD DE CIENCIAS FÍSICAS Y MATEMÁTICAS
DOCTORADO EN CIENCIAS FÍSICAS

**Double Periodic Variable stars: a
challenge to evolutionary process of close
binary stars**

**Estrellas Variables Doble periódicas: un
desafío al proceso evolutivo de estrellas
binarias cercanas**

POR

JAIME ANDRÉS ROSALES GUZMÁN

**Tesis para optar al grado académico de Doctor en Ciencias
Físicas**

Profesor Guía: Dr. Ronald E. Mennickent Cid

Departamento de Astronomía,
Facultad de Ciencias Físicas y Matemáticas
Universidad de Concepción

**CONCEPCIÓN - CHILE
DICIEMBRE 2018**

© Se autoriza la reproducción total o parcial, con fines académicos, por cualquier medio o procedimiento, incluyendo la cita bibliográfica del documento.





Director de Tesis : Dr. Ronald Mennickent Cid

Comisión : Dr. Dominik Schleicher
Dr. Sergey Zharikov

Dedicated to the memory of Blanca Rosales...



Preface

When I set out to do a thesis related to Double Variable Periodic stars and their evolutionary processes, I felt really excited but at the same time a little confused for not having the slightest idea where to begin to explain these fabulous and enigmatic stars. This project immersed me in a world of emotions and ideas, while I performed a literary compilation of diverse authors who made reference to the subject in question. At that moment, I found the first difficulties that alluded to the little diversity of information about these binary systems, and made that the preparation of this project was slow and stormy, but I managed to avoid the difficulties in the course of time, so I decided write this thesis, considering all those undergraduate, Master and Doctorate students, also of the astronomy lovers unsatisfied of some answers to the phenomenon of the Double Periodic Variable. Then I decided to explain the obtained information in a simple way, describe the most outstanding aspects and discuss the nature of these systems. In turn, I did an effort use the technical words appropriately and highlight the concepts involved. However, as it is impossible to talk about astronomy without resorting to these technicalities. Therefore, the order in which I have organized this thesis follows a simple classical scheme from the simplest to the most advanced topics, for to do the reading a pleasant process but at the same time educational. I hope that every reader enjoy this work as much as I have enjoyed writing it. In addition I want to remind the reader that when opening this thesis or simply an astronomy book, it means to be reading in an orderly and accumulated way a knowledge gathered by generations of astronomers, who did an non easy job.



Acknowledgments

Foremost, I would like express my acknowledgments to my mother Patricia Guzmán Echeverría who always trusted in me and gave me the necessary energies to continue with my dreams and passions. Also, I want to thank everyone that at this moment are not in this life but they were fundamental in mine. I want to acknowledge to my advisor Dr. Ronald E. Mennickent Cid, because was a honor to be his Ph.D. student during the last four years, because he has taught me of consciously and unconsciously way the best of him. I appreciate all his willingness of time, ideas, and support for conduce my Ph.D., the joyfulness and enthusiasm that he has for develop the research of contagious and motivational way, even during tough times, and for the excellent example he has provided me as a successful scientist and professor. I would like to acknowledge to the honorary secretary Ms. Marcela Sanhueza Lagos for her time, interest and helpful comments. To the members of Stellar Variability Group & Search for Planets who have contributed immensely to my professional development within of the university.

My time at University was enjoyable in large part due to the many friends who that became a important part of my life. Particularly, I would like acknowledge to Francesco Mauro for every help and good moments, in addition to Evelyn Johnston, Linda Schmidtbreich and Amelia Bayo for their time and help to find a solution to my questions, in addition is a glad to render thanks to my girlfriend Inna Borsolyuk by her patience, sweetie, joyfulness, loyalty and overall for her support at the unhappy moments. I would like to thank to the ex-Chamber of Integration Chile-Ukraine (IDECU) who allowed me generate new integration agreements in the field of education between Taras Shevchenko National University of Kyiv, the Space Agency of Ukraine and the University of Concepción.

Also, I gratefully acknowledge the funding sources that made my Ph. D. studies possible such as Physics Department and the Astronomy Department during my first year of Ph.D., and I must emphasize that this doctoral thesis was possible thank to observations conduced under CNTAC proposal CN2015A-123, to the scholarship from the Faculty of Physical Sciences and Mathematics of the University of Concepción, to the support from the Chilean BASAL Centro de Excelencia en Astrofísica y Tecnologías Afines (CATA) grant PFB-06/2007, the grant from Gemini-CONICYT Project 32140015, support from project FONDECYT 1110347, support from Astronomy Department of the

VIII

University of Concepción, the fund from project ALMA-CONICYT 31130006 and finally to the support of Sociedad Chilena de Astronomía (SOCHIAS) who was fundamental for to attend to different national and international conferences.



Resumen

En esta tesis hemos realizado un detallado análisis fotométrico, espectroscópico y de modelación numérica en diversas estrellas azules variables de doble período, llamadas Double Periodic Variable (DPV). Primero realizamos una búsqueda exhaustiva de datos fotométricos en el catálogo de estrellas variables ASAS en la banda V, y seleccionamos las DPV que mostraron los períodos orbitales más extremos posibles con el objetivo de poder restringir los límites del período orbital de las DPV. A través del software IRAF utilizamos la tarea Phase Minimization Dispersion (PDM-IRAF) y hemos determinado el período orbital de cada sistema. Con la ayuda de un código diseñado por Zbigniew Kołaczkowski¹ pudimos remover ambas frecuencias y armónicos asociados al ciclo orbital, el ciclo largo y/o sub-orbitales de nuestros sistemas. Una vez obtenido ambos períodos por separado, hemos determinado las efemérides y sus respectivas épocas para sus máximos fotométricos.

Mediante el uso de múltiples espectrógrafos tales como CORALIE del Observatorio La Silla de la ESO, ECHELLE del Observatorio San Pedro Mártir y CHIRON del Observatorio Interamericano Cerro Tololo, hemos realizado un análisis espectroscópicos de los sistemas en el cual hemos seleccionado algunas líneas de absorción características que representaban el movimiento de cada componente. Estas líneas de absorción nos permitieron medir las velocidades radiales, calcular la razón de masa y los parámetros orbitales de cada sistema. Una vez bien conocidas las velocidades radiales, realizamos una separación espectroscópica de cada componente para un posterior análisis utilizando el método del disentangling de (González & Levato, 2006) y determinamos los parámetros físicos de cada estrella realizando una comparación mediante un test de chi-cuadrado entre el espectro promedio y un espectro sintético. Luego analizamos emisiones en los perfiles H α y H β para comprender el comportamiento de los discos de acreción que presentaron las estrella más calientes llamada gainer.

Realizamos diversos estudios para comprender si estos sistemas estaban en rotación sincrónica, analizamos sus densidades medias y período orbitales críticos y restringimos las masas de cada componente. También utilizamos códigos especialmente diseñados para sistemas binarios con discos de acreción y mediante algunos parámetros físicos obtenidos previamente, pudimos realizar

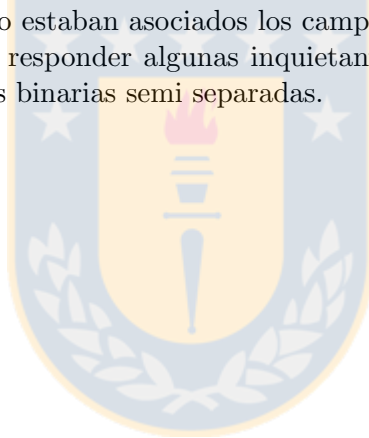
¹† deceased

un análisis de la curva de luz a través del método inverso y determinar los parámetros fundamentales de cada componente por separado.

Hemos determinado la distancia utilizando un método clásico mediante el uso de magnitudes aparentes, absorción interestelar y correcciones bolométricas, entre otros. También construimos la distribución de energía espectral considerando flujos compuestos y dejamos el parámetro de distancia como un parámetro libre con el objetivo de determinar nuevamente la distancia y asegurarnos de haber obtenido con gran precisión este valor.

También implementamos modelos teóricos de estrellas solas, para comparar y estimar en que etapa evolutiva se encontraba cada componente estelar. No obstante, el método utilizado no fue de gran precisión por lo que implementamos un modelo teórico binario que incorporó un disco de acreción y logramos determinar con gran precisión el proceso evolutivo completo de una DPV.

Finalmente seleccionamos la DPV con el período más largo para poder analizar de manera detallada cada mecanismo asociado al proceso evolutivo de las DPV, y comprender como estaban asociados los campos magnéticos en las DPV, estimamos y pudimos responder algunas inquietantes preguntas acerca de estas enigmáticas estrellas binarias semi separadas.



Abstract

In this thesis we performed a detailed photometric, spectroscopic and numerical modeling analysis in several blue variable stars of double period, called Double Periodic Variable (DPV). First we did an exhaustive search of photometric data in the ASAS variable star catalogue in the V-band, and we selected the DPVs that showed the more extreme orbital periods possible with the aim to restrict the limits for the orbital period of a DPV. Through the IRAF software we used the Phase Minimization Dispersion (PDM-IRAF) task and we have determined the orbital period of each system. With the help of a code designed by Zbigniew Kołaczkowski² we removed both frequencies and harmonics associated with the orbital cycle, the long cycle and/or sub-orbitals of our systems. Once that we obtained both periods separately, we determined the ephemeris and their respective epochs for their photometric maximums.

Through the use of multiple spectrographs such as CORALIE from La Silla Observatory of ESO, ECHELLE from the San Pedro Mártir Observatory and CHIRON from the Cerro Tololo Inter-American Observatory, we have performed an spectroscopic analysis of the systems in which we have selected some characteristic absorption lines which represents the movement of each component. These absorption lines allowed us to measure the radial velocities, calculate the mass ratio and the orbital parameters of each system. Once the radial velocities are well known, we perform a spectroscopic separation of each component for further analysis using the disentangling method of (González & Levato, 2006) and we determine the physical parameters of each star by a comparison using a chi-square test between the average spectrum and a synthetic or theoretical spectrum. Then we analyzed the emissions of the H α and H β profiles to understand the behavior of the accretion disks which is presented in the hotter stars called gainer.

We carried out several studies to understand if these systems were in synchronous rotation, we analyzed their critical orbital periods and the mean densities, in addition we constraints the masses of each component. Also we used a code specially designed for binary systems with accretion disks and through some physical parameters previously obtained, we performed an analysis of the light curve through the inverse method and determined the fundamental parameters of each component separately.

²† deceased

We have determined the distance using a classical method using the apparent magnitudes, interstellar absorption and bolometric corrections, among others. We also constructed the spectral energy distribution considering the distance as free parameter and we determined again the distance to ensure if we have obtained this value with great precision.

We also implemented theoretical models of single stars, to compare and estimate in which evolutionary stage was located each star. However, the method used was not quite accurate so we implemented a theoretical binary model using MESA code that incorporated an accretion disk and we have determine with great accuracy a complete evolutionary track of a DPV.

Finally we selected the DPV with the larger period to analyze in detail each mechanism associated with the evolutionary process of the DPV, and understand how the magnetic fields were associated in the DPVs, in addition we estimated and answer some disturbing questions about these enigmatic binary stars semi-detached.



Contents

Preface	V
Acknowledgments	VII
Resumen	IX
Abstract	XI
List of figures	XVII
List of tables	XXIII
1 Introduction	1
1.1 Orbital motion: Two bodies	3
1.2 Close binary stars	5
1.2.1 Configuration of the system	6
1.3 Mass tranfer	8
1.3.1 Conservative mass transfer	8
1.3.2 Non conservative mass transfer	9
1.4 Stellar dynamo	11
1.4.1 Pre Maxwell equations	11
1.4.2 Decay of magnetic fields	12
1.4.3 Dynamo model and Spruit's constraint	13
1.5 Double Periodic Variables	15
1.6 The aim of this work and its structure	16
2 Photometric search of DPVs using ASAS catalogue	19
2.1 New Galactic Double Periodic variables	19
2.2 DD CMa: A New Galactic Double Periodic Variable of extreme short period	21
2.3 TYC 5353-1137-1: an enigmatic Double Periodic Variable of semiregular amplitude	24
3 A new sub-orbital period in DD CMa with partial evidence of accretion disk	29
3.1 Abstract	29

3.2	Introduction	30
3.3	Photometric analysis	31
3.4	Spectroscopic observations	33
3.5	Spectroscopic analysis	33
3.5.1	Radial velocities	33
3.5.2	Spectral disentangling	37
3.5.3	Determination of gainer physical parameters	38
3.5.4	The H α emission line profile	39
3.5.5	Gainer, mass ratio and circumstellar matter	39
3.5.6	Mass constraints from spectroscopy	41
3.6	Light curve model and system parameters	42
3.6.1	The fitting procedure	42
3.6.2	The best light-curve model	42
3.7	Distance determination	43
3.8	Conclusions	44
4	On the orbital and stellar parameters of the hot Algol HD 50526, its accretion disk and evolutionary stage	49
4.1	Abstract	49
4.2	Introduction	50
4.3	Photometric ephemeris	51
4.4	Spectroscopic observations	52
4.5	Spectroscopic analysis	54
4.5.1	Spectral disentangling	54
4.5.2	Determination of donor physical parameters	54
4.5.3	Radial velocities for the donor	55
4.5.4	Temperature indicators: He I 4471 and Mg II 4482	58
4.5.5	The H α emission line profile	60
4.5.6	Gainer, mass ratio and circumstellar matter	62
4.5.7	Mass constrains from spectroscopy	64
4.6	Light-curve model and system parameters	64
4.6.1	The fitting procedure	64
4.6.2	The best light-curve model	67
4.7	Reddening, distance and spectral energy distribution	68
4.7.1	Distance determination	68
4.7.2	Position in the H-R Diagram	69
4.7.3	Spectral Energy Distribution (SED)	71
4.8	Conclusions	73
5	Spectroscopic and photometric study of the eclipsing interacting binary V495 Centauri	81
5.1	Abstract	81
5.2	Introduction	82
5.3	Photometric ephemeris	82
5.4	Spectroscopic observations	84

5.5	Spectroscopic analysis	84
5.5.1	Spectral disentangling	84
5.5.2	Determination of donor physical parameters	85
5.5.3	Radial velocities for the donor	85
5.5.4	The H α emission line profile	90
5.5.5	Gainer, mass ratio and circumstellar matter	90
5.5.6	Mass constraints from spectroscopy	92
5.6	Light-curve model and system parameters	93
5.6.1	The fitting procedure	93
5.6.2	The best light-curve model	93
5.7	Reddening, distance and spectral energy distribution	95
5.7.1	Distance determination	95
5.7.2	Position in the H-R Diagram	97
5.7.3	Spectral Energy Distribution (SED)	98
5.8	Conclusions	99
6	Evolutionary process of the Double Periodic Variable: V495 Centauri	107
6.1	Abstract	107
6.2	Introduction	107
6.3	On the model	108
6.3.1	Mass transfer	110
6.3.2	Mass loss	110
6.3.3	Internal structure and rotation	111
6.3.4	The fitting procedure	113
6.4	Evolution of the DPV 495 Cen in the HR diagram	116
6.5	Structural changes in the components of V495 Cen during binary evolution	120
6.6	Stellar dynamo in the donor star	121
6.7	Discussion	123
6.8	Conclusions	124
7	Conclusions	127
	References	131
	Curriculum Vitae	137
7.1	List of publications	137



List of Figures

1.1	(Left) Mesh surface representation of Roche’s potential in a binary star with a mass ratio 2, in a co-rotating frame (Credit: van der Sluys, M., (Materie-overdracht)). (Right) The contours with drop-shaped are equipotential surfaces and represents the lobes of Roche of each of the stars. The Lagrange points where the gravitational forces cancel each other out are labeled as L_1 , L_2 and L_3 respectively.	6
1.2	Three cases of configuration of a binary system, where the colors represents every possible configuration of eclipsing detached (green), eclipsing semidetached (blue) and eclipsing contact (red). The black line corresponds the inner critical Roche equipotentials, wherein the potential ϕ is in units of $G(M_1+M_2/a)$ and the horizontal scale is in units of the semi-major axis a	8
2.1	Disentangled ASAS V -band light curves of the new confirmed Double Periodic Variables.	20
2.2	Disentangled ASAS V -band light curves of the new candidate Double Periodic Variables.	21
2.3	Disentangled ASAS V-band light curve of the new confirmed Double Periodic Variable.	23
2.4	(Left) The ASAS photometry reveals a gradual decrease of the DPV TYC 5353-1137-1 brightness during 2500 days, followed by an increase in the amplitude of photometric variation over the last 1000 days of 42% (Right). The red line corresponds to a 3rd-order polynomial representing the mean magnitude.	25
2.5	Disentangled ASAS V-band light curve of the new confirmed Double Periodic Variable. The orbital phase has been separated in three datasets (-2450000.0), representing the variation of the amplitude.	26
2.6	The long cycle phase has been disentangled and separated in three datasets (-2450000.0). The first dataset shows less amplitude in the light curve of the long cycle (blue), during the second epoch occurs an effect of switch off (red), and the third dataset shows a remarkable increase in the amplitude of variability (green). Note the different y-axis scales in the panels.	27

3.1	Histogram of magnitude for DD CMa using 100 bins for 466 ASAS A-type data, showing a skewed distribution towards the left side. The dashed red line corresponds to a normal distribution of 466 random data with mean $\mu = 11.533$ and sigma $\sigma = 0.053$	32
3.2	Disentangled ASAS V-Band light curve for the orbital phase with orbital period $P_o = 2.0084(1)$ d (left), a long period $P_l = 89.18(16)$ d (right) and the third sub-orbital period $P_{sub} = 0.3335$ d (down) for DD CMa after disentangling.	32
3.3	Radial velocities of the donor using HeI (4713, 4921 ,5875 ,6678) and for the gainer H α and H β measured through Gaussian fits. Both fits were using a sinusoidal adjustment assuming a circular orbit.	35
3.4	Disentangled H α profile of gainer star, showing slightly homogeneous and similar peaks, probably caused by the accretion disk.	37
3.5	Surface color map of chi-square analysis with 6 freedom degrees obtained for the gainer star, and with all other parameters at their optimized values to find the best theoretical normalized spectrum. The best obtained value $\Delta\chi_6^2 = 0.177$ is represented by a red dot at T= 21000 K and $\log g = 4.5$ dex.	38
3.6	Detailed comparison between the observed (black line) and theoretical (red line) gainer spectrum.	39
3.7	Comparison of H α profiles centered at 6562.8 Å and with the donor contribution subtracted, during a complete orbital cycle.	40
3.8	Equivalent width of H α profile of the gainer star during a complete orbital cycle (Top). The continuum black line is fitted 4rd order polynomial to the mean EW, while the blue line corresponds to sinusoidal fit using least squares with of three free parameters. (Bottom) Violet and red intensities (V/R) ratio of H α profile measured from the continuum of the gainer with donor contribution subtracted, and the black line corresponds to 5rd order polynomial fit. Every polynomials fits presents a confidence interval region of 95% with respect to the mean, wherein is bigger at the regions without values.	40
3.9	Observed (LCO), synthetic (LCC) light-curves and the final O-C residuals between the observed and synthetic light curves of the DD CMa; fluxes of donor, gainer and of the accretion disk, normalized to the donor flux at phase 0.25; the views of the model at orbital phases 0.18, 0.53, 0.68 and 0.98, obtained with parameters estimated by the light curve analysis.	47
4.1	HD 50526 ASAS V-band phased light curves after disentangling. Orbital phase (up) and long period phase (down). Phases were calculated according to times of light curve minimum and maxima respectively, as given by equation (1) and (2).	51
4.2	Histogram of magnitudes for HD 50526 using 50 bins for 269 ASAS A-type data. The dashed red line corresponds to normal distribution of 269 random data with mean $\mu = 8.275$ and sigma $\sigma = 0.044$	52
4.3	(Left) Number of spectra per bin of 0.05 for the orbital phase. (Right) Number of spectra per bin of 0.04 for the long cycle phase.	53

4.4	Disentangled H α line after applying the González & Levato method for gainer star.	54
4.5	Chi-square analysis to find the best theoretical normalized spectrum with respect to the observed spectrum. The dots mesh of χ^2 was computed with three freedom degrees and with all parameters at their optimized values for donor star, presenting a minimum value in $\Delta\chi^2 = 1.642$ from a total of 20012 data.	55
4.6	Synthetic spectrum model (red line) has been veiled according to factor $\eta = 0.44$ and over plotted on donor spectrum previously disentangled (black line).	56
4.7	A detailed comparison of H β between the observed (black line), synthetic (red line) spectrum and a A0II spectral type star from UVES-POP (Blue line).	56
4.8	Orbital period as function of the eccentricity calculated by Monte Carlo simulations. Solid black line correspond to 1σ , dashed gray line to 2σ and the red dot to the minimum χ^2	58
4.9	Radial velocities of MgI 4482 (donor) and HeI 4471 (gainer) measured by Gaussian fits. The best fits are shown for both orbits.	59
4.10	(Left) Theoretical Equivalent widths of He I 4471 and EW ratio of between He I 4471 and Mg I 4482 lines as a function of the effective temperature for $z=0.02$, $v_{\text{sini}}= 150 \text{ km s}^{-1}$, $v_{\text{mic.}}=2.0 \text{ km s}^{-1}$, $v_{\text{mac.}}=10 \text{ km s}^{-1}$. (Right) Observed EW_{4471} and $\text{EW}_{4471/4482}$ versus orbital phases for CORALIE and ECHELLE data of the gainer star. The continuum line is a fitted 4rd order polynomial to the mean EW with a confidence interval region of 95% of the mean EW, the green symbols at $\phi_o = 0.75$ corresponds to the equivalent width disentangled.	60
4.11	(Top) From left to right, comparison of H α spectra during a complete orbital phase (donor subtracted) for the gainer star.(Bottom) left to right, analysis of H α spectra close to the maximum of the long cycle (donor subtracted). The orbital and long cycle phases were labeled to left and right of every spectra.	61
4.12	Equivalent width of H α profile from gainer star for several orbital (Top) and long cycle epochs (Bottom) with donor subtracted, using Coralie and Echelle spectrographs. The continuum line is a fitted 4rd order polynomial to the mean EW with a confidence interval region of 95%.	62
4.13	(Top) Comparison of normalized fluxes centered in the H α profiles during a complete orbital phase of the gainer star, (Bottom) Violet and Red intensities (V/R) ratio of H α profile, measured from the continuum of the gainer star.	63
4.14	Observed (LCO) and synthetic (LCC) light-curves of DPV HD50526 obtained by analyzing photometric observations; final O-C residuals between the observed and synthetic light curves; fluxes of the donor, gainer and of the accretion disk, normalized to the donor flux at phase 0.25; the views of the model at orbital phases 0.05, 0.30 and 0.80, obtained with parameters estimated by the light curve analysis.	66

4.15	Hertzsprung-Russell diagram of binary evolutionary track. The donor star onsets with a mass $M_{i,d} = 5.20 M_{\odot}$ while the gainer with $M_{i,g}=1.8 M_{\odot}$ for an initial orbital period $P_{i,o}=2.10$ days. The stellar tracks were calculated with $Z=0.02$ and the color bar shows the central hydrogen mass fraction for both components. The track was represented using circles that show the change of the stellar radius for both components. The orange lines connects the best model solution with the observed data.	70
4.16	Comparison between the theoretical normalized extinction curve (red) and the observed (blue) obtained by IRSA. The great effect of varying that occurs in R_v changes the shape of the extinction curve at the shorter wavelengths. Therefore, is not correct to extrapolate the values close to the FUV but we can affirm that the effect is less than the theoretical k	72
4.17	Best fit of spectral energy distribution, considering a composed flux by two stars without considerer the contribution of the disc.	73
5.1	Histogram of magnitude for V495 Cen with 50 bins	83
5.2	V495 Cen ASAS V-band light curve after disentangling. Orbital period (up) and long period (down). Phases were calculated according to times of light curve minimum and maxima, given by equation (1) and (2)	84
5.3	The $H\alpha$ line on HJD 2457062.80354576 ($\phi_o = 0.24, \phi_l = 0.68$) and the best synthetic spectrum for the donor.	85
5.4	A detailed comparison between the observed and synthetic (best model: smoothed line in red colour) donor spectrum.	86
5.5	Colour map of χ^2 with two degrees of freedom and with all other parameters at their optimized values for donor star corresponding to value of $\Delta\chi^2 = 8.26$ from a total 12134 data.	86
5.6	The radial velocities of the donor obtained by cross correlation of a region plenty of metallic lines and the best fit, given for Eq. 4.	88
5.7	He I 5015 for HJD 2457062.78265893 ($\Phi_o = 0.24, \Phi_l = 0.68$, up) and for HJD 2457078.7407534 ($\Phi_o = 0.72, \Phi_l = 0.70$, below). The dotted (red) arrow indicates the donor star component while the solid (black) arrow indicates the component attributed to the gainer.	89
5.8	Radial velocities of the He I 5015 C1 component and He I 5875 C2 component measured by gaussian fits. For comparison we show the velocities measured with the cross correlation method, applied to a region plenty of metallic lines (red dots). The best fits are shown for both orbits.	89
5.9	The behavior of $H\alpha$ line sorted by phases. The radial velocities were over plotted in each spectrum to compare with the movement of the donor (blue dots) and gainer (red triangles).	90
5.10	(Left) Variation of the $H\alpha$ profile at different orbital phases. (Right) $H\alpha$ profile average with representative sizes. The width of the absorption was measured at the height of the continuum but was raised to facilitate the visibility of the data.	91

5.11	The equivalent width of the $H\alpha$ emission line as a function of the orbital phase. Black dots correspond to spectra obtained with slicer mode, while the blue dots are spectra obtained in fiber mode.	92
5.12	The solid line is given by equation 8 and the dashed lines show the synchronous ($q = 0.158$) and the observed (sub-synchronous, $q = 0.119$) cases. .	93
5.13	From top to bottom we show the observed (LCO) and synthetic (LCC) light-curves of V495 Cen obtained by analyzing photometric observations, final O-C residuals between the observed and optimum synthetic light curves, flux of donor, gainer and of the accretion disc, normalized to the donor flux at phase 0.25. The views of the optimal model at orbital phases 0.05, 0.50 and 0.80 obtained with parameters estimated by the light curve analysis. . .	96
5.14	Hertzsprung-Russell diagram of evolutionary track for non-rotating single stars models (Ekström et al., 2012). The blue line corresponds to $6.0M_{\odot}$ while the red line to $4.35M_{\odot}$. Lines represent stellar tracks without rotation calculated at $Z= 0.014$	98
5.15	The best fit to the spectral energy distribution (SED) considers a two-star composite spectrum; it reproduces well the bluer part but exhibits a significant excess from the near-infrared that is probably formed in the circumstellar material. The black and orange theoretical spectrum is given by equation 14.	100
6.1	Mass loss/transfer fraction. α correspond to the fraction of mass lost from the vicinity of the donor as fast wind, β mass lost from the vicinity of the accretor, δ is the mass lost from the circumbinary coplanar toroid and ϵ is the fraction of accreted mass.	109
6.2	Best model for V495 Cen of 8 freedom degree with all optimized parameters values for both stars, with a $\Delta\chi_{0.95,8}^2 = 0.212$	114
6.3	Evolution of the orbital period as a function of the mass of the primary star (donor) of V495 Cen.	115
6.4	Orbital velocities curve for both components as a function of their masses. The primary component (black line) increases their orbital velocity during the loss mass process known as spin-up and later decrease reaching the current value. The secondary (dashed red line) component shows a diminutions of their radial velocity and a mass gain.	115
6.5	Schematic behavior of radius and mass for both stars. The gainer star (dashed red line) decreases its radius, while the donor star (black line) expands to fill the Roche lobe.	116
6.6	Theoretical variation of mass transfer until reaching the helium depletion for initial masses $M_{i,d} = 3.40 M_{\odot}$, $M_{i,g} = 3.18 M_{\odot}$ with initial orbital period $P_{i,o} = 3.9$ d.	116

- 6.7 Evolutionary track of primary or donor star (black line) and its companion (red line). The important points of the evolution were labeled together to the initial masses. The dashed green line correspond to evolutionary track of a single star of initial mass $M_{i,s} = 3.40 M_{\odot}$ using the same initial parameters of the donor star until the central helium depletion ($X_{He,c} < 0.2$). The dashed blue line is the evolutive track for a single star of mass $5.76 M_{\odot}$ with the similar characteristics of the gainer star. 117
- 6.8 Hertzsprung-Russel (H-R) diagrams showing the binary evolution. The color bar shows the central hydrogen and helium mass fraction for both components and confirms a rejuvenation of the gainer retaining their size during great part of their lifetime, whereas that the donor star suffers a rapid evolution exhausting their helium during the mass transfer phase. 118
- 6.9 Change of the orbital period as a function of the time, labeled with the more important stage related to mass transfer and their change during the mass inversion. 119
- 6.10 \dot{M}_d curve for the best evolutionary model of the donor star. The vertical dashed line (black) indicates the optically thick mass transfer, the continuum the mass ratio $q=1$, i.e. $m_1=m_2$ and the continuum blue line corresponds to the end of the phase of optically thick mass transfer. 119
- 6.11 (Left) Kippenhahn diagrams showing the evolution of internal structure of both stars, accompanied (Right) by a zoom with some principal events labeled. (Up) diagram of donor star with initial mass $M_{d,i} = 3.40 M_{\odot}$, (Down) diagram of gainer star with initial mass $M_{g,i} = 3.18 M_{\odot}$. Both model stop when the donor star reaches core helium depletion $X_{He,c} < 0.2$. The x-axis give the age after ignition of hydrogen in units of Myr. The different layers are characterized by their values of M/M_{\odot} , convection mixing in hatched green, semi convection mixing in red, overshooting mixing in crosshatched purple, thermohaline mixing in hatched yellow, the solid black line shows the surface of each star and brown zone corresponds to rotational mixing. 120
- 6.12 Three profiles of the magnetic fields generated by the Tayler-Spruit dynamo in the poloidal (radial) and toroidal (azimuthal) components to the donor star. From top to bottom the profiles are hydrogen depletion, mass transfer and current stage of the system. The Eulerian diffusion coefficient (yellow) out of the convective zone is stopping and allow to the Spruit-Tayler (ST) diffusion coefficient (Brown-dashed) work within radiative zone. The poloidal magnetic field (black) is modeled by the diffusion ST coefficient, while the toroidal magnetic field (green) is dominant as is expected. The angular momentum and velocity are represented in blue and red, respectively. 123

List of Tables

2.1	New confirmed Double Periodic Variables and their orbital (P_o) and long (P_l) periods. Epochs for the minimum brightness of the orbital light curve and the maximum brightness of the long-cycle light curve are also given. . .	20
2.2	New candidates Double Periodic Variables and their orbital (P_o) and long (P_l) periods. Epochs for the minimum brightness of the orbital light curve and the maximum brightness of the long-cycle light curve are also given. Brightness values are from the ASAS database.	21
2.3	New confirmed Double Periodic Variable and their orbital (P_o) and long period (P_l). Both epoch for the minimum brightness of the orbital light curve and the maximum brightness of the long-cycle light curve are given. .	22
2.4	Parameters of the newly confirmed DPV TYC 5353-1137-1 and its orbital (P_o) and long period (P_l). Epoch for both the minimum brightness of the orbital light curve and the maximum brightness of the long-cycle light curve are given.	26
3.1	Parameters of the Double Periodic Variable DD CMa and its sub-orbital period (P_s) incorporated, the orbital (P_o) and long period (P_l), with their respective epochs for the minimum and maximum brightness.	31
3.2	Summary of spectroscopic observation, wherein N corresponds to the number of spectra, HJD at mid-exposure for the first spectrum series is given, ϕ_o and ϕ_l are the orbital and long cycle phase respectively, and are calculated according to the Eq. 3.2 and Eq. 3.3. The espectral resolution $R \sim 25000$ (fiber mode).	33
3.3	Radial velocities of the donor and their respective errors, using $H\alpha$ (6562.8 Å) and $H\beta$ (4861.33 Å)	34
3.4	Radial velocities of the gainer and their respective errors, using He I (4713 Å), He I (5875 Å)	35
3.5	Orbital parameters for the gainer of DD CMa obtained through minimization of χ^2 given by equation 3.4. The value $\tau^* = \tau - 2450000$ is given and the maximum and minimum are one isophote of 1σ	36
3.6	Free parameters of the sinusoidal and polynomial fits obtained for equivalen width (EW) and violet and red intensities of the $H\alpha$ profile of the gainer star. 41	41

3.7	Results of the analysis of DD CMa light-curves obtained by solving the inverse problem for the Roche model with an large accretion disk partially obscuring the more-massive (hotter) gainer in critical non-synchronous rotation regime.	46
4.1	Orbital elements for the donor of HD 50526 obtained through minimization of χ^2 given by equation (1). The value $\tau^* = \tau - 2450000$ is given and the maximum and minimum are one isophote 1σ	58
4.2	Results of the analysis of DPV HD 50526 V-filter light curve obtained by solving the inverse problem for the Roche model with an accretion disk around the more massive (hotter) gainer in synchronous rotation regime. . .	65
4.3	Comparisson between the results of the theoretical model for HD 50526 obtained with MESA code, with a confidence interval of 95% and 16 freedom degree, versus the inverse problem for the Roche model analyzing the light curve in V-filter.	70
4.4	Summary of spectroscopic observation using CORALIE spectrograph, where N is number of spectra per date. The HJD at mid-exposure for the first spectrum series is given, the orbital (Φ_o) and long cycle (Φ_l) phases were calculated using the Eq. 1 and Eq. 2 respectively with a spectral resolution of $R \sim 60000$	75
4.5	Summary of spectroscopic observation using ECHELLE spectrograph, where N is number of spectra per date. The HJD at mid-exposure for the first spectrum series is given, the orbital (Φ_o) and long cycle (Φ_l) phases were calculated using the Eq. 1 and Eq. 2 respectively with a spectral resolution of $R \sim 18000$	76
4.6	Summary of spectroscopic observation using CHIRON spectrograph, where N is number of spectra per date. The HJD at mid-exposure for the first spectrum series is given, the orbital (Φ_o) and long cycle (Φ_l) phases were calculated using the Eq. 1 and Eq. 2 respectively with a spectral resolution of $R \sim 80000$ (Slicer mode).	77
4.7	Radial velocities of the donor and their respective errors, using Mg 4482 Å .	78
4.8	Radial velocities of the gainer and their respective errors, using HeI 4471 Å	79
4.9	Photometry points extracted from Vizier Catalogue with a search radius of 2 arsec to build the Spectral Energy Distribution	80
5.1	Orbital elements for the donor of V495 Cen obtained through minimization of χ^2 given by equation (1). The value $\tau^* = \tau - 2450000$ is given and the maximum and minimum are one isophote 1σ	88
5.2	Results of the analysis of the V-band light-curve of V495 Cen obtained by solving the inverse problem for the Roche model with an accretion disc around the more-massive (hotter) gainer in the synchronous rotation regime.	94

5.3 Summary of spectroscopic observation. N is number of spectra. The HJD at mid-exposure for the first spectrum series is given, Φ_o and Φ_l refer to the orbital and long-cycle phase, respectively, and are calculated according to Eq. 1 and Eq. 2. Spectral Resolution $R \sim 80000$ (with image slicer) and $R \sim 25000$ (fiber mode). 101

5.4 Radial velocities of the donor and their errors. 102

5.5 Radial velocities of the gainer and their errors. 103

5.6 Radial velocities of He I 5875 and their errors 104

5.7 Photometry points extracted from Vizier Catalogue with a search radius of 2 arsec to build the Spectral Energy Distribution 105

6.1 Evolutive stages for DPV V495 Cen until ^4He depletion of the donor star and their main feautres. 122

7.1 Results of mass/radius ratio of three different DPVs at their current stage respectively. 127





Chapter 1

Introduction

The ancient Egyptians wrote a Calendar of Lucky and Unlucky Days, 3000 years ago, wherein they related their mythological events with some astronomical events. This was called the Cairo Calendar (CC) dated to 1244-1163 B.C. In this calendar the lucky events were related to a period of 2.85 days, whose value is equal to period described by Algol's regular variability. But at that epoch, Algol was represented as Horus which signified both divinity and kingship and they tried gives textual descriptions of the daily prognoses through of this star [Jetsu & Porceddu \(2015\)](#). To date, we know that Algol is a star known colloquially as the Demon star which derives from Arabic ra's al-ghūl (head (ra's) of the ogre(al-ghūl)) located in the constellation of Perseus. Initially it was considered as a variable star, later a binary system but now is know that is composed for three stars , i.e. it is a multiple system composed by β Per A, β Per B and β Per C. The AB system has an orbital period $P_{AB,o} = 2.867$ days and its apparent magnitude at the visual vary between 2.09 and 3.30 mag pursuant to VSX¹.

For understanding, what mean variable stars is necessary know these stars presents changes in their brightness. These changes can vary from a thousandth of a magnitude to several magnitudes during periods of a fraction of seconds or even years, the reasons why variable stars change their brightness depend on the type of the variable star. e.g., an eclipsing binary will dim when it is eclipsed by a faint companion, and then brighten when the faint star moves out of the way. Even some variable stars are actually extremely close pairs of stars, exchanging mass when one of these has filled the Roche lobe. The different causes on their brightness variation can be classified in two different categories:

- **Intrinsic variable stars:** The variability is caused by physical changes such as pulsation or eruption in the star or stellar system.
- **Extrinsic variable stars:** In this case the variability is caused by a star that eclipse to its companion, the transit of an extra-solar planet, or simply by the effects of stellar rotation.

¹<https://www.aavso.org/vsx/index.php?view=search.top>

Also, exist a large list of variable stars, in which they differs in their variations type, periods, sizes, masses, etc. All of them have been the result of accumulated information by whole generations of astronomers around the world. Thus, I will mention only the most studied and known to date, such as:

- Pulsating variables
 - Cepheids
 - RR Lyrae
 - RV Tauri
 - Long period
 - Mira
 - semiregular
 - irregular variables
- Cataclysmic variables
 - Supernovae
 - Novae
 - Dwarf Novae
 - SU Ursae Majoris
 - Symbiotic stars
- Eruptive variables
 - R Coronae Borealis
- Eclipsing Binary stars
 - Eclipsing binary
 - Eclipsing Algol type
 - Eclipsing Beta Lyrae type
 - Eclipsing W ursa Majoris type
- Rotating stars
- Irregulars



However, every variable star of the same category will be different of other. Therefore, before starting to analyze a binary system is necessary to know some general characteristics of these systems and the physics behind of the calculations. The next sections within of this chapter are a brief review about close binary stars, for most details see [Hilditch \(2001\)](#); [Eggleton \(2006\)](#).

1.1 Orbital motion: Two bodies

The binary systems could be considered fundamental for to find solutions for the problems of the celestial mechanics, due that these systems provide information about stellar masses and their radii. When one of the components is more massive than the other, the movement of this is tiny if it is compared with its companion, so the less massive star seems to turn around of the most massive. The name that receives this orbit is named as relative orbit, and the equations of motions of both stars are:

$$M_1 \ddot{\vec{r}}_1 = -\frac{GM_1 M_2}{r^2} \hat{r}; \quad M_2 \ddot{\vec{r}}_2 = -\frac{GM_1 M_2}{r^2} \hat{r}, \quad (1.1)$$

where G is the Gravitational constant, M_1 and M_2 are the primary and secondary masses respectively and r corresponds to the separation between the two stars. To obtain the relative motion of a star, that corresponds to a ellipse in which the primary component occupies one of the focus, simply we must subtract the two equations of motions (eq. 1.1) of both stars:

$$\ddot{\vec{r}}_1 - \ddot{\vec{r}}_2 = -\frac{GM_1 M_2}{r^2} \hat{r}, \quad (1.2)$$

therefore, if $\mu = M_1 M_2 / (M_1 + M_2)$ (reduce mass), then the motion of either body in its relative orbit would be as if the orbiter has a mass μ and the central mass was the total mass of the system. The determination of this relative orbit, allow us to know some constants or elements of the orbits whose character is only geometric and others are related to the time. However, the orbits of both components around of the center mass is commonly called as absolute orbits, these orbits are ellipses of equal eccentricity than the relative orbit, wherein the center mass is the common focus to both stars, named barycenter. Thus the two barycentric equations of motion are:

$$\ddot{\vec{R}}_1 = -\frac{GM_2^3}{(M_1 + M_2)^2} \frac{\vec{R}_1}{R_1^3}, \quad \ddot{\vec{R}}_2 = -\frac{GM_1^3}{(M_1 + M_2)^2} \frac{\vec{R}_2}{R_2^3}, \quad (1.3)$$

where R_1 and R_2 are the motion vectors of each body relative to the barycenter of the system. The relationship between barycentric and the relative orbits of each component, is bound to: the orbital periods of the system P, of the primary star P_1 , and secondary star P_2 , in addition to semi-major axis, the orbital eccentricity and the time. Consequently the three periods $P_1 = P_2 = P$ are equal. Thus we can write the Kepler's third law as $M = 4\pi^2 a^3 / P^2$ and when it is applied in the three orbits, results the follow:

$$\text{Relative orbit:} \quad a = a; \quad M = G(M_1 + M_2) \quad (1.4)$$

$$\text{Barycentric orbit of } M_1: \quad a = a_1; \quad M = GM_2^3/(M_1 + M_2)^2 \quad (1.5)$$

$$\text{Barycentric orbit of } M_2: \quad a = a_2; \quad M = GM_1^3/(M_1 + M_2)^2, \quad (1.6)$$

for the particular case of circular orbits, the speed of a body in motion around the center of mass is constant. But for the cases of eccentric orbits, the speed is continuously varying as function of the position and time. In these cases the Kepler's second law states that the radius vector sweeps out equal areas in equal intervals of time. If we use of the geometry of an ellipse and other parameters such true anomaly (ϕ), eccentric anomaly (E) and eccentricity in addition of the Kepler's third law, we can build an auxiliary circle that touches the ellipse in the periastron and apastron, allowing us to specify the angular position of the star as a function of time in the elliptical orbit with the mathematical expression called Kepler's equation:

$$E - e \sin E = \frac{2\pi}{P}(t - T), \quad (1.7)$$

the parameter P is the orbital period and τ is the time of periastron passage, also we must emphasize that the right side of the eq. 1.7 is determined directly from observations. To resolve the previous equation, we must relate the the eccentric anomaly with the true anomaly, through of a trigonometric relationship of half angles:

$$\tan\left(\frac{\theta}{2}\right) = \sqrt{\frac{1+e}{1-e}} \tan\left(\frac{E}{2}\right), \quad (1.8)$$

But as we have seen, these parameters are related to the absolute size of the orbits and to the masses of the stars. Thus, we can derive the relationships between measured radial velocities and the orbital parameters of a star as:

$$V_{rad} = K[\cos(\theta + \omega) + e \cos(\omega)] + \gamma, \quad (1.9)$$

where θ is the true anomaly, $K = (2\pi a \sin i)/P(1 - e^2)^{1/2}$ corresponds to half amplitude of the radial velocity, γ is the velocity of the system center mass, ω the periastron longitude and e the orbital eccentricity. For a spectroscopic binary, the velocity curves of both components can be determined directly from observation, doing measurements of displacement of some absorption lines. This allow us derivate for each star their respective masses M_1 or M_2 , in addition the projected semi-major axis, which is can be derived from the half-amplitude of the follow form:

$$a_{1,2}\sin i = \frac{(1 - e^2)^{1/2}}{2\pi} K_{1,2} P, \quad (1.10)$$

if we remember that $M_1 a_1 = M_2 a_2$ and $G(M_1 + M_2) = 4\pi^2 a^3 / P^2$, then we can get an expression for the minimum masses:

$$M_{1,2}\sin i = \frac{1}{2\pi G} (1 - e^2)^{3/2} (K_1 + K_2)^2 K_{2,1} P, \quad (1.11)$$

however, in some cases of spectroscopic binary stars just is possible detect single absorption lines, but the radial velocity variation of the single spectrum allows obtain the orbital period P and the eccentricity e , in addition also the amplitude K of the radial velocity variation, or equivalently the projected semi-major axis. Therefore, the information on masses is contained in a single function, called the mass function, composed by both masses with an unknown orbital inclination:

$$f_2 = \frac{M_1^3 \sin^3 i}{(M_1 + M_2)^2} = 1.0361 \times 10^{-7} (1 - e^2)^{3/2} \left(\frac{K_2}{\text{km s}^{-1}} \right)^3 \frac{P_o}{\text{days}} M_\odot, \quad (1.12)$$

whose meaning represents the minimum possible mass for the unseen star, for a system with unknown orbital inclination and elliptical orbit. Thus we can write a relationship between masses called mass ratio and is represented by the following equation:

$$q = \frac{M_2}{M_1}, \quad (1.13)$$

therefore the masses of both stars can be calculated only if we can determinate the orbital inclination of the system.

1.2 Close binary stars

As we could see a binary system is composed by two stars orbiting around of their common barycenter. However, if a binary system is orbiting in a plane along our line of sight, their components will eclipse each other. These type of system are called eclipsing binaries and are detected by their changes on the brightness during the eclipses. If both components are close enough each other, then one of them can gravitationally distort its companion, or even occur a mutual distortion. In some particular cases, theses systems can exchange mass, and alter the evolutionary process of each one.

Therefore, to explain the restricted problem of two masses moving in circular orbits around of their common center mass, is possible write a three-dimensional hypothetical

surface which could be constructed around the two masses that represents the region of the space where the motion of a third particle would be zero relative to the coordinate system, which this would rotate uniformly with the two masses in their circular orbits. This hypothetical model, was proposed by French mathematician Edouard Roche and was called Roche lobe, so named in his honor. The Roche lobe has a shape similar to a drop of water stretched with the apex of the drop pointing towards the companion and located at the point of Lagrange L1 (see Fig. 1.1), which can be calculated by the following equation:

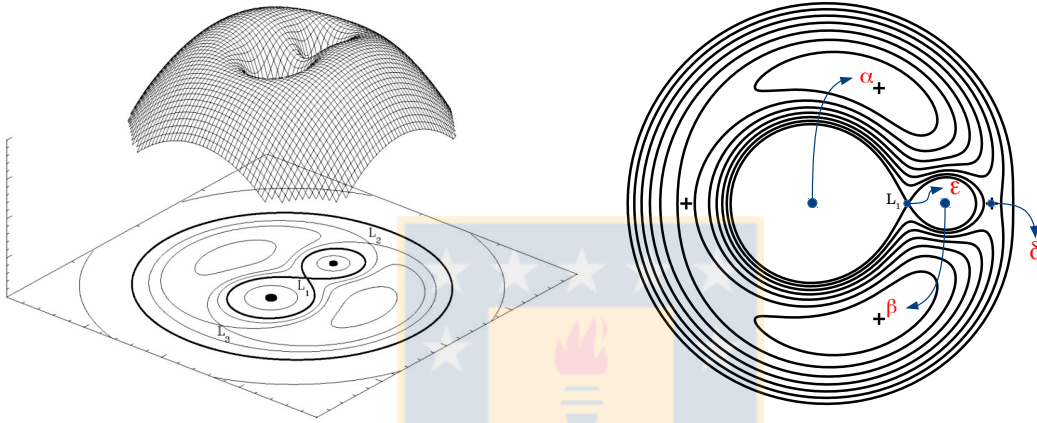


Figure 1.1: (Left) Mesh surface representation of Roche's potential in a binary star with a mass ratio 2, in a co-rotating frame (Credit: van der Sluys, M., ([Materie-overdracht](#))). (Right) The contours with drop-shaped are equipotential surfaces and represents the lobes of Roche of each of the stars. The Lagrange points where the gravitational forces cancel each other out are labeled as L₁, L₂ and L₃ respectively.

$$\phi = -\frac{GM_1}{r_1} - \frac{GM_2}{r_2} - \frac{\omega^2}{2} \left[\left(x - \frac{M_2}{(M_1 + M_2)} \right)^2 + y^2 \right], \quad (1.14)$$

where $r_1 = (x^2 + y^2 + z^2)^{1/2}$ and $r_2 = [(x-1)^2 + y^2 + z^2]^{1/2}$.

1.2.1 Configuration of the system

As we know, a star within of the main sequence increases in size during its evolution and it may exceed the Roche lobe. This mean that the matter approaches to region of gravitational pull of its companion, causing that the matter will transfer through a process called Roche lobe overflow (RLOF), see Fig. 1.2. The matter in falling toward the most massive star can be absorbed by direct impact or through an accretion disc. Resulting these in

another classification based on the distance between the stars and their relative sizes:

- **Detached binaries (ED)** : are binary stars where every star is within of Roche lobe, i.e., the area where the gravitational pull of the itself star is greater than of the companion. Thus, the stars do not have an important effect over on each other and every one can evolution of separate and independent way during the hydrogen burning. Here the evolution is slow (nuclear timescale, eq. 1.15) and both star evolves of stable way along of the main sequence. However, there is other cases that during the late stages of core Hydrogen burning, occurs a short break after hydrogen burning called case AB and later continues as Case B.

The great most belong to this category (Fig. 1.2, green).

$$t_{nuc} = (7 \times 10^9) \frac{M}{M_{\odot}} \frac{L_{\odot}}{L} \quad (yr), \quad (1.15)$$

- **Semidetached binaries (ESD)** : in this case one component has filled the Roche lobe, called donor star and it has leaved the main sequence, while the companion yet not. This process occurs before to the helium ignition and the gas on the surface of the star that has filled the Roche lobe, start the mass transfer towards its companion driving by the fast expansion of the donor in a thermal timescale (eq. 1.16) due to the donor is crossing the Hertzsprung-gap while is burning hydrogen in the shell (Fig. 1.2, blue), whose case is called CASE B. However, some stars at the same case b stops because stars recedes inside Roche Lobe upon loss of Hydrogen envelope, and later resumes on envelope expansion in Helium shell burning phase which is called Case BB.

$$t_{th} = \frac{GM^2}{RL} = (3.0 \times 10^7) \left(\frac{M}{M_{\odot}} \right)^2 \frac{R_{\odot}}{R} \frac{L_{\odot}}{L} \quad (yr), \quad (1.16)$$

- **Contact binaries (EC)** : in this type of binary stars, the donor star has filled the Roche lobe after the core helium ignition and both stars interact before to the donor star ends its life, i.e., both components has filled the Roche lobe and the upper part of the stellar atmospheres form a common envelope that surrounds both stars. As the sheath friction slows orbital movement, the stars could eventually merge. In high mass stars the mass transfer occurs in a dynamical timescale (eq. 1.17) and it is often unstable (Fig. 1.2, red).

$$t_{dyn} = \left(\frac{2R^3}{GM} \right)^{1/2} \approx 40 \left[\left(\frac{R}{R_\odot} \right)^3 \frac{M_\odot}{M} \right]^{1/2} \quad (min), \quad (1.17)$$

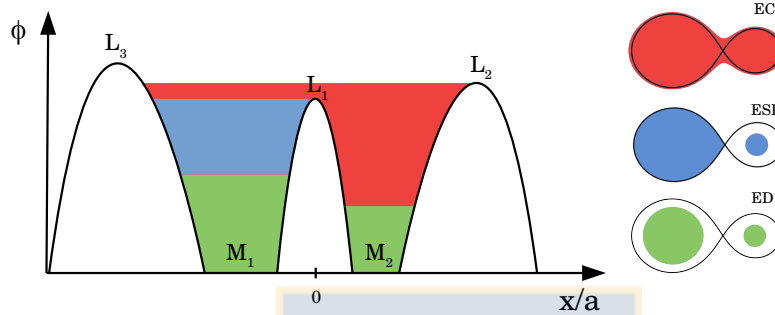


Figure 1.2: Three cases of configuration of a binary system, where the colors represents every possible configuration of eclipsing detached (green), eclipsing semidetached (blue) and eclipsing contact (red). The black line corresponds the inner critical Roche equipotentials, wherein the potential ϕ is in units of $G(M_1+M_2/a)$ and the horizontal scale is in units of the semi-major axis a .

1.3 Mass transfer

The phenomenon of mass transfer in close binary stars is bound to the evolution of the stars that make up the system. During long time the stars living most part of their life at the main sequence, but during the transitions from an evolution stage to another, the stars expands and contract, providing processes of mass transfers. This mass in falls towards the companion and can be absorbed by direct impact or doing a spiral, forming a disc around of the accretor called accretion disc. The mass transfer are governed by two modes; the conservative mass transfer and non conservative mass transfer.

1.3.1 Conservative mass transfer

In this mode all mass lost by one component, called donor star is gained by its companion, and so the total mass of the binary is conserved $M_{tot}=M_1+M_2$, together with the total orbital angular momentum J_{orb} . This mass transfer type implies that the total angular momentum of the binary system is composed by:

$$J_o = \left[\frac{GM_1^2 M_2^2 a (1 - e^2)}{M_{tot}} \right]^{1/2}, \quad (1.18)$$

so if remember that $\dot{M}_{tot} = 0$ and we use the Kepler's third law, we can define the initial masses as M_{1i} , M_{2i} , and the orbital period as P_i . At the same way P , M_1 and M_2 are after start the mass transfer we obtain:

$$\frac{\dot{P}}{P_i} = \frac{dp/dt}{P} = 3 \left(\frac{M_{1i} M_{2i}}{M_1 M_2} \right)^2 \left(-\frac{\dot{M}_1}{M_1^2 M_2} - \frac{\dot{M}_2}{M_1 M_2^2} \right) M_{1i} M_{2i}, \quad (1.19)$$

Due it is a conservative mass transfer, then ($\dot{M}_1 = -\dot{M}_2$). Thus we obtain:

$$\frac{\dot{P}}{P_i} = 3 \frac{P}{P_i} \left(\frac{M_1 - M_2}{M_1 M_2} \right) \dot{M}_1 \quad (1.20)$$

$$\frac{\dot{P}}{P} = \frac{3(M_1 - M_2)}{M_1 M_2} \dot{M}_1, \quad (1.21)$$

The solution suggests that P depends of \dot{M} . But is important emphasize that the bracketed term $(M_1 - M_2)$ could change when occur the mass inversion, i.e. $M_1 < M_2$. Then if the most massive star transfers mass towards the companion, the orbital period will decrease its value until that both mass are equal. Later to the mass inversion, the orbital period will increase again.

1.3.2 Non conservative mass transfer

During the mass transfer process can occurs some nonconservative mechanisms. These can be caused by stellar wind, whose process is independent if the donor filled or not the Roche lobe. In addition there are fast events, which involves a Roche lobe over flow (RLOF) and another catastrophic mass loss, such as in novae and supernovae in one of both components of the system. We can represent the non conservative mass transfer by a spherically symmetric wind that does not interact with the companion. Contrary to the conservative mass transfer, we must write that $\dot{M}_1 < 0$ and $\dot{M}_2 = 0$ and using the Kepler's third law, and this can be differentiated to obtain the change of the orbital period:

$$P^2 = \frac{4\pi^2 a^3}{G(M_1 + M_2)} \quad (1.22)$$

$$\frac{\dot{P}}{P} = \frac{1}{2(M_1 + M_2)} \left(\frac{3\dot{a}(M_1 + M_2)}{a} - \dot{M}_1 \right), \quad (1.23)$$

if we consider that the lineal velocity of the donor is constant and follows the relationship $a_1 = aM_2/(M_1 + M_2)$, it tells us that $a(M_1 + M_2) = \text{constant}$, thus $\dot{a}(M_1 + M_2) + a\dot{M}_1 = 0$ and we get:

$$\frac{\dot{P}}{P} = \frac{-2\dot{M}_1}{M_1 + M_2}, \quad (1.24)$$

this means that for $\dot{M}_1 < 0$ which is caused by a stellar wind, the orbital period must increase, independent if the donor are losing mass. Another way and more rigorous of wind-driven mass transfer and RLOF was proposed by [Tout & Hall \(1991\)](#), where the system has an orbital eccentricity equal to zero, the donor star is losing mass to rate \dot{M}_1 and the accreted mass by the companion will be \dot{M}_2 and the rest will be lost from the system, i.e. $\dot{M} < 0$, $\dot{M}_1 < 0$ and $\dot{M}_2 > 0$. Therefore the lost angular momentum caused by the escaping material, will be the sum of the fraction of orbital angular momentum lost by the donor loser and that contributed by any mechanisms:

$$\dot{J} = \dot{M}a_1^2 2\pi/P + KJ, \quad (1.25)$$

wherein KJ represents any other mechanisms, and $J = 2\pi a_2 M_1 M_2 / P (M_1 + M_2)$ in addition $a_1/a = M_2/(M_1 + M_2)$, thus it can be written as:

$$\frac{\dot{J}}{J} = \frac{M_2}{M_1} \frac{\dot{M}}{M_1 + M_2} + K \quad (1.26)$$

$$\frac{\dot{J}}{J} = \frac{\dot{M}_1}{M_1} + \frac{\dot{M}_2}{M_2} + \frac{\dot{a}}{2a} - \frac{\dot{M}}{2(M_1 + M_2)} \quad (1.27)$$

$$\frac{\dot{P}}{P} = \frac{3\dot{a}}{2a} - \frac{\dot{M}}{2(M_1 + M_2)} \quad (1.28)$$

$$\frac{\dot{P}}{P} = -\frac{2\dot{M}}{M_1 + M_2} - \frac{3\dot{M}_2(M_1 - M_2)}{M_1 M_2} + 3K, \quad (1.29)$$

The result is a complete equation that gives us the previous results obtained: The first term to right hand of the equation is the conservative mass transfer via RLOF (see eq. 1.20), when we imposed $\dot{M} = K = 0$ and $\dot{M}_1 = \dot{M}_2$. The second term provides us the simple wind-driven mass-loss equation (see eq. 1.24), when was imposed that $\dot{M}_2 = K = 0$ and $\dot{M} = \dot{M}_1$. In addition, it allows the introduction of an additional angular-momentum-loss mechanism, via the K term, which might be via gravitational-wave radiation or magnetic braking.

1.4 Stellar dynamo

1.4.1 Pre Maxwell equations

The movement of a conductive plasma within a star of the main sequence, due to the convection, creates stellar magnetic field. The stellar convection occurs in form of hot bubbles divergent and ascending, and in form of cold bubbles converging submerging inwards. The divergent movement and convergent is caused by the stratification of the density. Thus the movement purely radial will be transformed in velocities of latitude and azimuth. To understand the associated magnetic fields in a star of the main sequence is necessary to review the basic equations of the electromagnetic theory, called Maxwell equations:

$$\nabla \cdot \mathbf{E} = \frac{\rho_c}{\epsilon} \quad (1.30)$$

$$\nabla \cdot \mathbf{B} = 0 \quad (1.31)$$

$$\nabla \times \mathbf{E} = -\frac{\partial \mathbf{B}}{\partial t} \quad (1.32)$$

$$\nabla \times \mathbf{B} = \mu \mathbf{j} + \frac{1}{c^2} \frac{\partial \mathbf{E}}{\partial t} \quad (1.33)$$

Wherein \mathbf{E} is the electric field, \mathbf{B} the magnetic field, \mathbf{j} the current density and $\mu = 4\pi \times 10^{-7}$ is the permeability in the free space, ρ_c is the charge density and finally $\epsilon = (\mu c^2)^{-1}$ is the dielectric constant. The Faraday's law equation (1.32) says that if a magnetic field varies then an electric field is produced. Thus, an electrically conducting body, the electric field drives a current, which is the basis of dynamo action (Jones , 2008).

Now if the fluid is in non-relativistic movement, then the Ampeère's/Maxwell's law can be written as:

$$\epsilon^{ijk} \partial_j B_k = \mu_0 J^i, \quad (1.34)$$

in general an electric magnetic field that crosses through an electric conducting will generate a current:

$$\mathbf{J}' = \sigma \mathbf{E}', \quad (1.35)$$

the apostrophe (') is to emphasize that in the Ohm's law is expected that it contains a conductive substance at rest. Therefore, for a fluid in non relativistic movement \mathbf{u} , the Lorentz transformation for the current density $\mathbf{J}' = \mathbf{J}$ and the electric field $\mathbf{E}' = \mathbf{E} + \mathbf{u} \times \mathbf{B}$

$$J = \sigma(E + u \times B) \quad (1.36)$$

$$E = -u \times B + \frac{1}{\mu_0 \sigma} (\nabla \times B) \quad (1.37)$$

now if we inserts the equation 1.37 within of Faraday's law with $\mu = 1/\mu_0\sigma$, we will obtain the Magnetohydrodinamical induction equation:

$$\frac{\partial \mathbf{B}}{\partial t} = \nabla \times (\mathbf{u} \times \mathbf{B} - \eta \nabla \times \mathbf{B}) \quad (1.38)$$

the first term on the right hand side represents the inductive action of fluid flowing across a magnetic field, while the second term represents dissipation of the electrical currents sustaining the field. Now if we replaces the temporary derivative by $1/\tau$ and the spacial derivate by $1/l$, we obtain a dimensionless ratio called as Magnetic Reynolds number:

$$R_m = \frac{(U_o B/l)}{\mu B/l^2} = \frac{U_o l}{\eta} \quad (1.39)$$

this dimensionless equation measures the importance of induction versus dissipation over length scale of order l , wherein the magnetic diffusivity is $\eta = 1/\mu_0\sigma \text{ m}^2\text{s}^{-1}$. When $R_m \gg 1$, induction by the flow dominates the evolution of \mathbf{B} , while $R_m \ll 1$ the induction make a negligible contribution and \mathbf{B} simply decays away under the influence of Ohmic dissipation.

1.4.2 Decay of magnetic fields

To understand the dynamo models is fundamental to study the magnetic field decay by Ohmic dissipation, due to the absence of movement of fluids. i.e., $R_m \ll 1$ and the induction equation then reduces to:

$$\frac{\partial \mathbf{B}}{\partial t} = \eta \nabla^2 \mathbf{B} - (\nabla \eta) \times (\nabla \times \mathbf{B}) \quad (1.40)$$

for the constant η , the equation 1.40 would look like a simple heat diffusion equation, with η playing the role of thermal diffusion.

Now we will focus in how the magnetic fields shows symmetry with respect to a axis, generally rotative. If we use the spherical polar coordinates (r, θ, ϕ) with the polar axis coinciding with the field's symmetry, then:

$$B(r, \theta, t) = \nabla \times (\mathbf{A}(r, \theta, t) \hat{e}_\phi) + \mathbf{B}(r, \theta, t) \hat{e}_\phi \quad (1.41)$$

The left hand side of the equation 1.41 contains the meridional component called vector potential, which defines the poloidal component of the magnetic field, while the azimuthal component corresponds to the right hand side of the equation and represents the toroidal magnetic field \mathbf{B} .

In the case of a pure diffusivity decay and for a magnetic diffusivity η these depends of the radius (r), wherein $\bar{\omega} = r \sin(\theta)$, then both components are completely separated as:

$$\frac{\partial A}{\partial t} = \eta \left(\nabla^2 - \frac{1}{\bar{\omega}^2} \right) \quad (1.42)$$

Due to the currents vanishing in the vacuum, i.e. in the exterior of the star ($r > R$). Thus, we need calculate for $r < R$ and obtain the same solution as was computed for $r > R$, in addition must satisfy the following condition:

$$\mu_0 \mathbf{J} = \nabla \times \mathbf{B} = 0 \quad (1.43)$$

which is translates into:

$$\left(\nabla^2 - \frac{1}{\bar{\omega}^2} \mathbf{A}(r, \theta, t) \right) = 0 \quad (1.44)$$

$$\mathbf{B}(r, \theta, t) = 0 \quad (1.45)$$

Wherein the solution of the equation 1.45 have a the general form of:

$$\mathbf{A}(r, \theta, t) = \sum_{l=1}^{\infty} a_l \left(\frac{R}{r} \right)^{l+1} Y_{l0}(\cos(\theta)) \quad r > R \quad (1.46)$$

where Y_{l0} corresponds to the spherical harmonics solutions of azimuthal order $m=0$, l a positive integer, modes with negative l being discarded to ensure proper behavior as $r \rightarrow \infty$.

1.4.3 Dynamo model and Spruit's constraint

A physic model of the magnetic field to great scale, must reproduces a magnetic field, axysymmetric for a good approximation and antisymmetric over the stellar equatorial plane. Also must generates a cyclic variation of the magnetic field, characterized by a polarity inversions with a period of oscillation of n years, to explain a dynamo model. To date we know that the differential rotation is an important mechanism to build a magnetic field in large scale. In addition the presence of stratification contributes to break the entropy and reflectional symmetry, generating a electromotive force which can produce large-scale magnetic fields. However the magnetic fields can be created in stably stratified layer in a differentially rotating star. A magnetic instability in the toroidal field replaces the role of convection in closing the field amplification loop [Spruit \(2002\)](#).

One of most relevant magnetic instability is the Tayler instability, together the differential rotation and the stratified layers are the ideal ingredients to apply into the problem of angular momentum transport. Spruit makes use of these ingredients to explain a dynamo

process based on the magnetic fields, toroidal and poloidal, assuming that the rotation rate is a function of the radial coordinate and the initial magnetic field must be sufficiently weak to allow that the poloidal magnetic field will be wounded by the differential rotation, allowing that toroidal magnetic field will be greater than the poloidal magnetic field, and when this occurs that the differential rotation is enough large to maintain a dynamo process. However an instability without thermal diffusion overestimates the intensity of the field required for generate this process, if the stratification is due to the thermal gradient. While the viscosity and magnetic fields are diffused by Coulomb interactions, here the viscosity is of the same order as the magnetic diffusivity, and at the same time it is the mechanism that controls the magnetic diffusion. This translate in that the instabilities may appear more easily. Independent of the intensity of the azimuth field, and the condition derived by Spruit was:

$$\frac{\omega_A}{\Omega} > \left(\frac{N}{\Omega}\right)^{1/2} \left(\frac{\kappa}{r^2\Omega}\right)^{1/4} \left(\frac{\eta}{\kappa}\right)^{1/2}, \quad (1.47)$$

wherein N corresponds to the buoyancy frequency, Ω the rotation rate, κ the thermal diffusivity, r the radial length scale and η the magnetic diffusivity $\omega_A \ll N \ll \Omega$ and $\eta \ll \kappa$. At the moment that the dynamo process onset due to the Taylor instability of an azimuthal field, the differential rotation provokes an increase of the energy and the small scale field due to the stratification is generated by the azimuthal component. Therefore, depending of saturation's level of this instability we can determine the amplitude of the small scale processes. In addition the speed with which these are generated depends of the stretching of the small scale magnetic field by the differential rotation, causing that the intensity of the magnetic field depends of the stretching and regeneration rate.

Now, If the field strength is sufficiently above the critical field for Taylor instability there is a range of radial length scales on which it can operate and the minimum shear rate q required to produce the critical magnetic field strengths for Taylor instability and drive convective motions are given by:

$$q_0 = \left(\frac{N}{\Omega}\right)^{7/4} \left(\frac{\eta}{r^2 N}\right)^{1/4}, \quad (1.48)$$

$$q_1 = \left(\frac{N}{\Omega}\right)^{7/4} \left(\frac{\eta}{r^2 N}\right)^{1/4} \left(\frac{\eta}{\kappa}\right)^{3/4}, \quad (1.49)$$

where q corresponds to the dimensionless differential rotation rate. When the thermal diffusion is neglected, corresponds to q_0 , while q_1 is considered when the effects of stratification is dominated by the composition gradient. But once produced the magnetic fields by the dynamo process, the azimuthal stress becomes in the follows expressions:

$$S_0 = \frac{B_{r0}B_{\phi0}}{4\pi} = \rho\Omega^2 r^2 q^3 \left(\frac{\Omega}{N}\right)^4, \quad (1.50)$$

$$S_1 = \rho\Omega^2 r^2 q \left(\frac{\Omega}{N}\right)^{1/2} \left(\frac{\kappa}{r^2 N}\right)^{1/2}, \quad (1.51)$$

where Spruit assumes that $\tau_T < \tau$ in the expression $f = 1 + \tau/\tau_T$ and that causes that the thermal diffusion will be neglected and the equation 1.48 will be higher than equation 1.49, considered as artifact due from the algebraic simplification. Therefore should use $N_e = N$ to corrects both expressions.

1.5 Double Periodic Variables

The discovery of the first Double Periodic Variables (DPV) based on an inspection of the OGLE-II database of a group of blue variable stars in the Large Magellanic Cloud (LMC) and the Small Magellanic Cloud (SMC) conducted by [Mennickent et al. \(2003\)](#), opened a new path to the understanding of the close binaries stars. These systems shown two closely linked photometric variations wherein the enigmatic long period is in average is 33 times longer than the orbital period ([Mennickent et al., 2016](#); [Mennickent, 2017](#); [Poleski et al., 2010](#); [Pawlak et al., 2013](#)). A principal characteristic of the DPV to difference of the Algol stars is the remarkable constancy of their orbital periods, while that the Algol stars undergoing to the mass transfer due to RLOF ([Garrido et al., 2013](#)). However an interesting property of some interacting binary systems is that show variations of the wind generated in the stream-disc impact region ([Mennickent et al., 2016](#); [van Rensbergen et al., 2008](#)), which appear in the well studied DPV V393 Scorpii by [Mennickent et al. \(2012\)](#), showing a cyclically variable bipolar wind, while that a recently research by [Garcés L et al. \(2018\)](#) observed changes on the light curves of some DPV and these could be related to changes in disc size/temperature and spot temperature/position.

Nowadays this enigmatic second variability is associated to a mechanism based on cycles of magnetic dynamo in the donor star by [Schleicher & Mennickent \(2017\)](#); [Mennickent et al. \(2018\)](#). The dynamo cycle P_{cycle} is related to the rotation period P_{rot} ([Soon et al., 1993](#); [Baliunas et al., 1996](#)) of the follow form:

$$P_{\text{cycle}} = D^\alpha P_{\text{rot}}, \quad (1.52)$$

where the dynamo number $D = C_\alpha \times C_\Omega = \alpha\Delta d^3/\eta^2$ is controlled by the quantities C_α and C_Ω called dynamo numbers. The measure of the helicity is represents by α , $\Delta\Omega$ corresponds to the large scale differential rotation, while d is the characteristic length scale of convection and finally η the turbulent magnetic diffusivity of the star. But for the purpose of express a dynamo model for DPVs Schleicher & Mennickent used the Rossby number Ro as $D = Ro^2$, and through a series of considerations for interacting binary systems finally

they can express the dynamo cycle as:

$$P_{cycle} = P_{rot} \left(11.5 \left(\frac{2\sqrt{2}}{15} \right)^{1/3} \frac{R_{\odot}}{yr} \right)^{-2\alpha} \times \left(\frac{L_2^{2/3} R_2^{2/3}}{M_2^{2/3}} \left(\frac{l_m}{H_p} \right)^{-4/3} \left(\frac{P_{Kep}}{\epsilon_H R_2} \right)^2 \right)^{-\alpha} \quad (1.53)$$

where the dynamo cycle is a function that depends of rotational period, the luminosity L which can be estimated from the effective temperature and Stefan-Boltzmann constant, radius R , mass M , the mixing length l , scale height H_P is the pressure scale height, P_{Kep} the Keplerian orbital period of a test particle on the surface of the donor star, and ϵ_H fraction of the Roche radius.

1.6 The aim of this work and its structure

The principal aim of this thesis is to find an explanation and solution to an enigmatic second photometric period observed in a special type of semi-detached interacting binary system, undergoing to loss/transfer of mass, discovered by [Mennickent et al. \(2003\)](#) and called as Double Periodic Variable stars.

This thesis aims to help understand how much material is lost by these binary systems, the preferred channels for the loss of mass, either by equatorial outflows or a hotspot winds. Through the MESA code and the fundamental parameters obtained for each DPV we have created a model of stellar evolution in which the processes involved in the evolution of a DPV from the ZAMS to the exhaustion of Helium are explained in detail, considering the mechanism of mass transfer/loss, stellar spin-up, winds, magnetic braking and tidal friction and the main instabilities that lead to the evolution of these systems. Finally, we have analyzed, using the Tayler-Spruit dynamo model, the toroidal and poloidal magnetic fields of the donor star and we have observed how they are generated and what mechanisms enhance them.

To carry out this work it was necessary to obtain high quality photometric data from the ASAS catalog and spectroscopic data from various telescopes and instruments. With the data obtained, we have identified lines of the hot and cold stellar components and determined their spectral types. We have also measured the radial velocities of each component using unraveled spectra and determined a dynamic solution for the stellar masses. With these paramaters we have used a code designed by Djurasevic, specially developed to use the two spectral types as input and solve the inverse problem of the unraveled orbital light curve for a binary system with and without an accretion disk. The best model allowed us to determine the stellar contributions and the accretion disk in each orbital phase. Then we investigated the residual spectra that contain the contribution of the accretion disk and we have measured the parameters as a function of the orbit phase, including the equivalent widths, discrete absorption components, asymmetries of absorption lines and emissions.

In the Chapter 2, We have carried out a detailed and exhaustive search of DPV stars within the ASAS catalog. In 2014 we conducted a visual inspection to find new long-period DPVs in the sections Eclipsing Detached, Semi-detached. In this work we have reported the galactic DPVs V495 Cen and V4142 Sgr. Both show a very well defined total primary eclipse, whose orbital periods were the longest found during that year, and we were able to visually identify its second photometric variability. Turning these two objects into interesting candidates to understand the evolution of DPVs. Three years later (2017) we carried out a new search by analyzing short-period variable stars, where we were able to identify the first DPV of the shortest and most known orbital period, in addition to three DPV candidates that were subsequently discarded due to their photometric characteristics. In addition, during the same year I have attended to the MESA Summer School, conducted by the University of California of Santa Bárbara (UCSB) to perfect myself in numerical modeling of stellar evolution and thus be able to develop the first evolutionary models of DPV stars. However, the following year (2018) in an unusual search within a miscellaneous category cataloged Misc by ASAS, we have discovered a new and enigmatic category of DPVs, which have a semi-circular amplitude, in which we have noticed an unusual ignition effect and off of the long cycle. Converting TYC 5353-1137-1 into the first short period DPV that presents a fascinating characteristic and converting it into a monitoring and research object to understand the stellar dynamo model.

In Chapter 3 we presents a brief photometric and spectroscopic analysis of the Double Periodic Variable DD CMA. This DPV shown an unusually sub-orbital period related to possible cyclic changes on the accretion disk, in addition we determined orbital and fundamental parameters of the system. In addition the performed analysis on the $H\alpha$ profile suggests us an accretion disk in formation stage and escaping material caused by the direct impact of the stream on the accretion disk.

In Chapter 4 we carried out a detailed photometric and spectroscopically analysis of the DPV HD 50526. This system was analyzed to understand the long-term variability through a high-resolution spectroscopic study with different spectrographs from the years 2008 to 2015. We have determined their fundamental parameters and noted a rapidly rate variation of V/R during the orbital period, which was interpreted as evidence of material ejected from the system.

In Chapter 5 we analyze a DPV of intermediate mass, characterized by the larger orbital period known to date, the DPV V495 Cen. In this system we determined the orbital and fundamental parameters through a spectroscopic and photometric analysis, and we noted that the mass transfer impacts the external edge of the accretion disc and presents a persistent $V < R$ asymmetry of the $H\alpha$ emission, which suggests the presence of a possible wind originated on the hotspot region.

In Chapter 6 we have developed and implemented a stellar evolution model based on the photometric and spectroscopic study the DPV V495 Cen, using the MESA code. Here we have evolved a binary system of intermediate mass wherein the gainer star can not accrete at high rate, because is limited by the Eddington accretion rate, which allowed us simulate an accretion disc and analyze the behavior of magnetic fields, instabilities, among other things.

Finally, in Chapter 7 we made a general conclusion of the Double Periodic Variables, the mechanism related to their evolution and brief discussion about the futures research

that we should carry out, finally we have added a section or Glossary to facilitate the understanding of the reader with some technical languages used in this thesis.



Chapter 2

Photometric search of DPVs using ASAS catalogue

2.1 New Galactic Double Periodic variables

Mennickent, R. E., Rosales, J.

Astronomy Department, University of Concepción, Concepción, Chile.

Published: Commissions 27 and 42 of the IAU Information Bulletin on Variable Stars

We have searched in the ASAS¹ catalogue of semi-detached eclipsing binaries (Pojmanski, 1997) for interacting binaries of the type Double Periodic Variable (DPV). These are intermediate-mass binaries characterized by a long photometric period lasting about 33 times the orbital period (Mennickent et al., 2003, 2012; Mennickent, 2013; Poleski et al., 2010). This long periodicity has been interpreted as evidence of mass loss cycles (Mennickent et al., 2008, 2012). We performed a visual inspection of the light curves provided by ASAS, and selected DPV candidates characterized by long-term tendencies in the upper and lower boundaries of the forest of data points. We determined the orbital and long periods by using the PDM IRAF² program (Stellingwerf, 1978). Errors for the orbital periods were estimated by visually inspecting the light curves phased with trial periods near the minimum of the periodogram. Then we disentangled the two main photometric frequencies by using a code specially designed for this purpose by Zbigniew Kolaczowski. The code adjusts the orbital signal with a Fourier series consisting of the fundamental frequency plus their harmonics. Then it removes this signal from the original time series letting the long periodicity present in a residual light curve. The program fits this remaining signal with another Fourier series consisting of a fundamental frequency and harmonics and removes it. As result we obtain the cleaned light curve with no additional frequencies and two light curves for the isolated orbital and long frequencies. Following this procedure we found two new DPVs and 3 DPV candidates. In the second group the long cycle is observed almost once and it is of low amplitude, so the classification is uncertain. The result of this search is summarized in Tables 2.1 and 2.2. The disentangled light curves are shown

¹<http://www.astrouw.edu.pl/asas/>

²IRAF is distributed by the National Optical Astronomy Observatories, which are operated by the Association of Universities for Research in Astronomy, Inc., under cooperative agreement with the National Science Foundation.

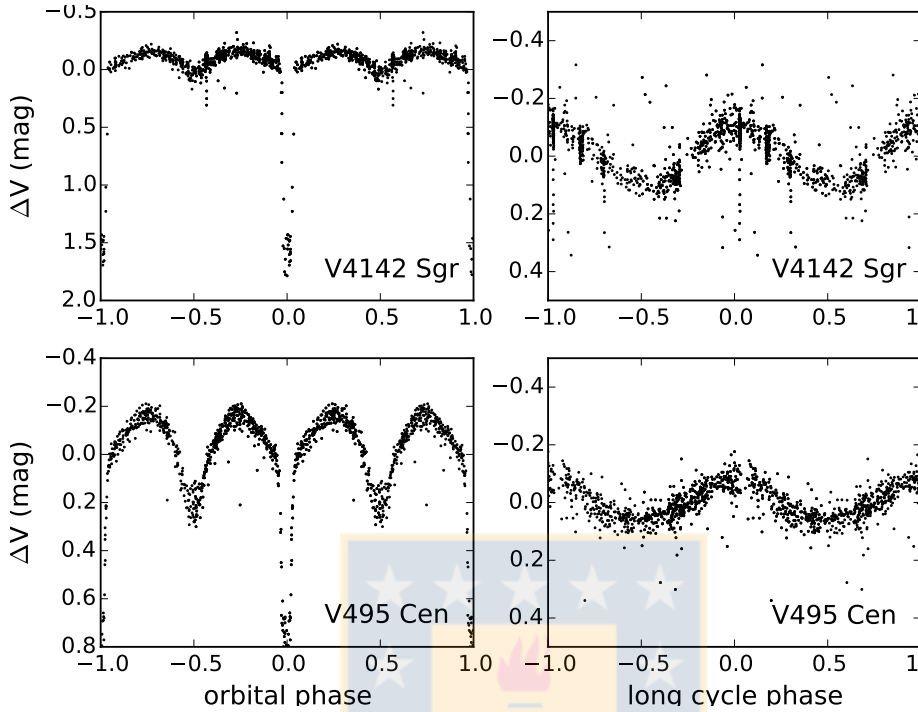


Figure 2.1: Disentangled ASAS V-band light curves of the new confirmed Double Periodic Variables.

in Figures 2.1 and 2.2. The two confirmed new DPVs are V495 Cen and V4142 Sgr. They show a total primary eclipse and have relatively long orbital periods. They are ideal targets for follow up spectroscopic studies and light curve modeling. All stars in Table 2.1 show longer orbital period than those 11 Galactic DPVs reported by Mennickent et al. (2012). For the suspected DPVs half of the orbital period was also a possible solution; we followed the ASAS choice, giving a period ratio around 33. We checked the WISE image survey3 (Wright et al., 2010), especially in the band W4, and find that none of these targets show evidence of close nebulosity, which could be relevant when discussing systemic mass loss and evolutionary stage.

Table 2.1: New confirmed Double Periodic Variables and their orbital (P_o) and long (P_l) periods. Epochs for the minimum brightness of the orbital light curve and the maximum brightness of the long-cycle light curve are also given.

ASAS-ID	Other ID	RA (2000)	DEC (2000)	P_o (days)	P_l (days)	$T_0(\min_o)$ -2450000	$T_0(\max_l)$ -2450000	$V(ASAS)$ (mag)
130135 – 5605.5	V0495 Cen	13 : 01 : 35	-56 : 05 : 30	33.490(18)	1283	4609.8460	4894.6	9.90
180745 – 2824.1	V4142 Sgr	18 : 07 : 45	-28 : 24 : 06	30.633(27)	1206	4726.5550	3546.7	10.95

2.2. DD CMA: A NEW GALACTIC DOUBLE PERIODIC VARIABLE OF EXTREME SHORT PERIOD

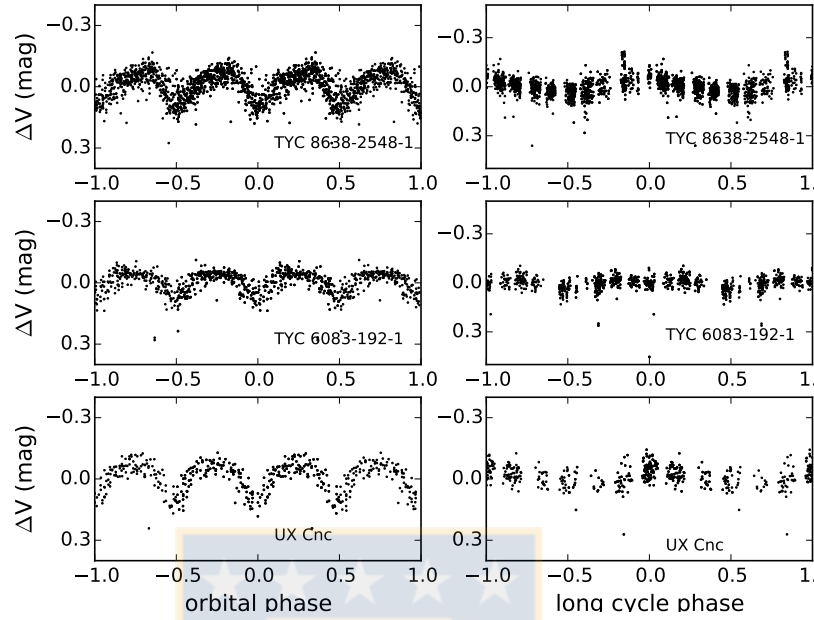


Figure 2.2: Disentangled ASAS V -band light curves of the new candidate Double Periodic Variables.

Table 2.2: New candidates Double Periodic Variables and their orbital (P_o) and long (P_l) periods. Epochs for the minimum brightness of the orbital light curve and the maximum brightness of the long-cycle light curve are also given. Brightness values are from the ASAS database.

ASAS-ID	Other ID	RA (2000)	DEC (2000)	P_o (days)	P_l (days)	$T_0(\min_o)$ -2450000	$T_0(\max_l)$ -2450000	$V(ASAS)$ (mag)
090329 + 0735.7	UX Cnc	09 : 03 : 29	07 : 35 : 42	84.761(10)	2158	2715.5975	2703.4	11.75
111014 + 2007.1	TYC 6083-192-1	11 : 10 : 14	-20 : 07 : 06	90.386(60)	3497	3125.4230	3799.8	9.37
114033 - 5641.8	TYC 8638-2548-1	11 : 40 : 33	-56 : 41 : 48	101.295(22)	3400	3423.3300	2471.0	10.51

2.2 DD CMA: A New Galactic Double Periodic Variable of extreme short period

Rosales G., J., Mennickent, R. E.

Astronomy Department, University of Concepción, Concepción, Chile.

Published: Commissions 27 and 42 of the IAU Information Bulletin on Variable Stars

We have performed a new search for interacting binaries of the type Double Periodic Variables

(DPVs) in ASAS³ (Pojmanski, 1997). We have considered Eclipsing Algols Semi-detached and Detached (EA/SD and EA/ED respectively) within the minimum orbital period of a classical DPV. The DPVs are intermediate binary stars that show closely linked photometric variations being the long period roughly 33 times longer than the orbital period (Mennickent et al., 2003, 2016; Poleski et al., 2010). The nature of the second period is unknown but suspected to reflect the strength variations of a wind generated in the stream-disc impact region (Mennickent et al., 2012, 2016; van Rensbergen et al., 2008). DPVs are considered as one specific evolutionary step for more massive Algols, one possibly involving mild mass transfer and systemic mass loss (Mennickent et al., 2008). But an interesting property of these objects is the surprising constancy of their orbital periods, which is not expected in Algols undergoing RLOF mass transfer (Garrido et al., 2013). Also the DPVs seem to be hotter and more massive than classical Algols and seem to have always a B-type component; their orbital periods typically run between 3 and 100 days. DPVs have been found in the Galaxy (MW), the Large Magellanic Cloud (LMC) and the Small Magellanic Cloud (SMC).

We carried out a visual inspection in ASAS for orbital period less than 3 but longer than 2 days. At this opportunity we have found only one new candidate to DPVs from 821 objects and determined the orbital and long period by using the PDM IRAF⁴ software (Stellingwerf, 1978). Also we have estimated the errors for the orbital period and long cycle by visual inspection of the light curves phased with trial periods near the minimum of the periodogram given by PDM. We disentangled the two main photometric frequencies using a code specially designed for this purpose by Zbigniew Kolaczowski. The code adjusts the orbital signal with a Fourier series, this code is able to disentangle both frequencies if we give us the fundamental frequency plus their harmonics. Then it removes this signal from the original time series letting the long periodicity present in a residual light curve. As result we obtain both isolated light curves without additional frequencies. The results of the search is presented in Table 2.3, and the disentangled light curves are shown in Figures 2.3. DD CMa was confirmed as the DPV that shows the shortest long-period found until moment, which makes it very peculiar. It is possible that under certain circumstances this short orbital period might let small room for the existence of an accretion disc and this fact makes this system particularly important to test models for the long-cycle based on disc winds. We believe that DD CMa is an optimal target for photometric monitoring and spectroscopic studies to help understand the mass loss process and evolutionary stage of the Algols and specifically the DPVs. Also we have searched for the presence of close nebulosity around this system with the WISE image service³ (Wright et al., 2010) especially in the band in W4 (22 mm), and we have confirmed the absence of nebulosity, which is relevant when discussing systemic mass loss and evolutionary stage in close binary stars with mass loss process.

Table 2.3: New confirmed Double Periodic Variable and their orbital (P_o) and long period (P_l). Both epoch for the minimum brightness of the orbital light curve and the maximum brightness of the long-cycle light curve are given.

ASAS-ID	Other ID	RA (2000)	DEC (2000)	P_o (days)	P_l (days)	$T_0(\min_o)$ -2450000	$T_0(\max_l)$ -2450000	$V(ASAS)$ (mag)
072409 - 1910.8	DD CMa	07 : 24 : 09	-19 : 10 : 48	2.0084(1)	89.18(16)	2763.46515	4207.411	11.41

³<http://www.astrouw.edu.pl/asas/>

⁴IRAF is distributed by the National Optical Astronomy Observatories, which are operated by the Association of Universities for Research in Astronomy, Inc., under cooperative agreement with the National Science Foundation.

2.2. DD CMA: A NEW GALACTIC DOUBLE PERIODIC VARIABLE OF EXTREME SHORT PERIOD

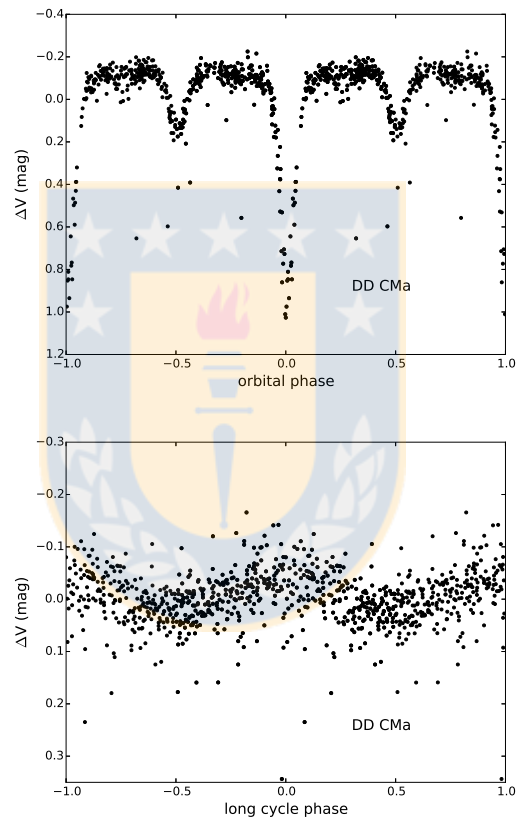


Figure 2.3: Disentangled ASAS V-band light curve of the new confirmed Double Periodic Variable.

2.3 TYC 5353-1137-1: an enigmatic Double Periodic Variable of semiregular amplitude

Rosales G., J., Mennickent, R. E.

Astronomy Department, University of Concepción, Concepción, Chile.

Published: Commissions 27 and 42 of the IAU Information Bulletin on Variable Stars

To date the Double Periodic Variables (DPVs) discovered by Mennickent et al. (2003) in the Large Magellanic Cloud (LMC) and the Small Magellanic Cloud (SMC) have been interpreted as semi-detached interacting binaries stars with a B-type component surrounded by an optically thick disk, these stars seem to experience regular cycles of mass loss (Mennickent et al., 2008) and are characterized by an orbital photometric variability on timescales of 2 to 100 days. These systems show a long period which is on average 33 times longer than the orbital period (Mennickent et al., 2016; Mennickent, 2017; Poleski et al., 2010). Currently, the DPVs found are Algol type eclipsing (DPV/E) and ellipsoidal (DPV/ELL) system.

Therefore, we have performed a new search for DPVs of short period in the ASAS⁵ catalog (Pojmanski, 1997), focusing on those stars with orbital periods between 2 to 3 days which also show variations in their brightness. From a total of 244 objects, we have found another candidate to DPV, one whose mean brightness is gradually decreasing. By fitting a 3rd order polynomial to the mean magnitude (red line) and then moving it to zero for a second analysis, a gradual decrease over 2500 days was revealed. During the last 1000 days of this decrease, a 42% increase in the variation between the minimum and maximum values of the magnitude was observed (Fig. 2.4). We determined the orbital period by using the PDM IRAF⁶ software (Stellingwerf, 1978) and estimated the errors for the orbital period and long cycle by visual inspection of the light curves phased with trial periods near the minimum of the periodogram given by PDM. The two main frequencies of the system were disentangled using the code written by Zbigniew Kołaczkowski and described by Mennickent et al. (2012). This code was specially designed to adjust the orbital signal with a Fourier series and disentangle both frequencies using the fundamental frequencies and harmonics we supplied. The code removed this signal from the original time series thus allowing long periodicity to appear in a residual light curve, and we obtained both isolated light curves without additional frequencies, as shown in (Fig. 2.5, 2.6). We presented the search results and ephemeris in Table 2.4 and Fig. 2.4 (Left) both of which illustrate the gradual brightness decrease in the ASAS photometry. In the right panel of this figure we show the photometric variation ΔV shifted to average zero and, finally, the disentangled light curves in Fig. 2.5 and 2.6.

This enigmatic DPV presents a semiregular amplitude of the light curve when it is phased using the orbital period at three different photometric datasets (Fig 2.5). The changes in the orbital light curve could be related to changes in disc size/temperature and spot temperature/position as proposed by Garcés L et al. (2018) for the DPV OGLE-LMC-DPV-097. Posteriorly, we disentangled the light curve of the long period and phased it. For that, we used the same time intervals as those used for the orbital period as a way to analyze possible variations in the amplitude of the light

⁵<http://www.astrouw.edu.pl/asas/>

⁶IRAF is distributed by the National Optical Astronomy Observatories, which are operated by the Association of Universities for Research in Astronomy, Inc., under cooperative agreement with the National Science Foundation.

2.3. TYC 5353-1137-1: AN ENIGMATIC DOUBLE PERIODIC VARIABLE OF SEMIREGULAR AMPLITUDE

curve of this enigmatic phenomenon in the DPVs, and we apparently observed an effect of switch off-on of the long-cycle in the dataset of HJD between 2500 and 4000 (Fig. 2.6), this is observed for the first time in these type of systems. Therefore, we consider TYC 5353-1137-1 to be an optimal target for further photometric monitoring and spectroscopic studies, due to that will help us to test the mechanism based on cycles of the magnetic dynamo in the donor proposed by [Schleicher & Memickent \(2017\)](#), the cause of mass loss in some Algol stars and the evolutionary process of the DPVs.

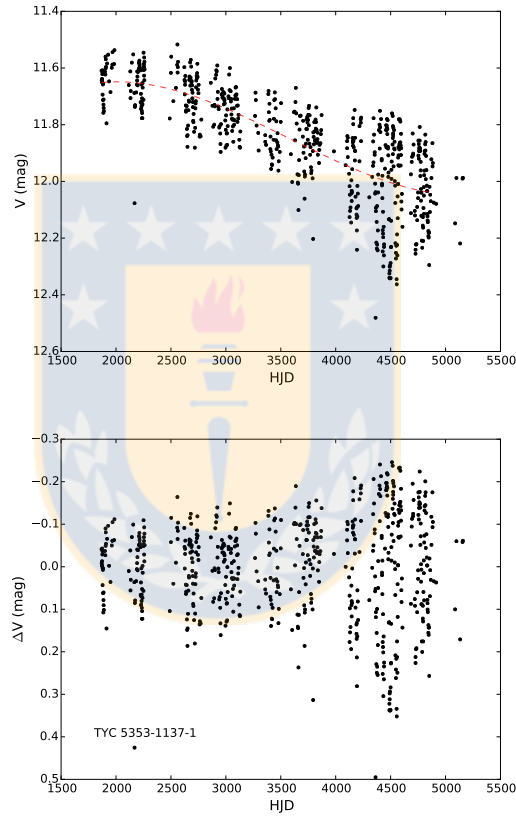


Figure 2.4: (Left) The ASAS photometry reveals a gradual decrease of the DPV TYC 5353-1137-1 brightness during 2500 days, followed by an increase in the amplitude of photometric variation over the last 1000 days of 42% (Right). The red line corresponds to a 3rd-order polynomial representing the mean magnitude.

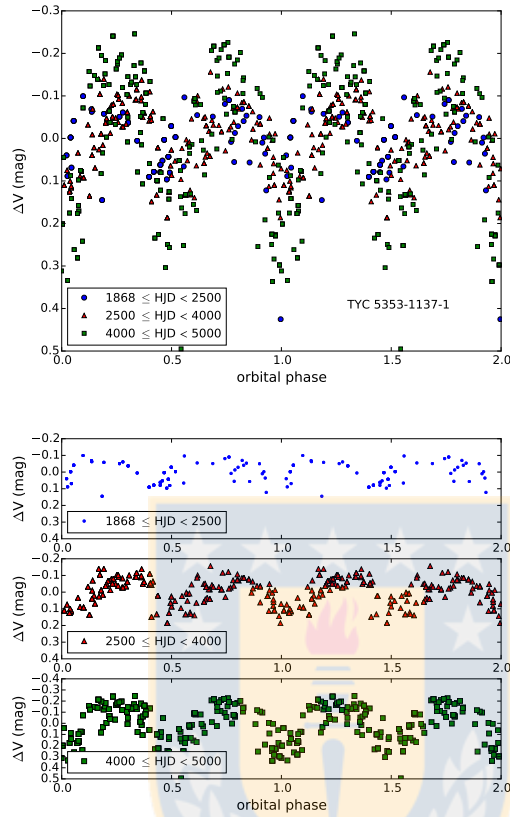


Figure 2.5: Disentangled ASAS V-band light curve of the new confirmed Double Periodic Variable. The orbital phase has been separated in three datasets (-2450000.0), representing the variation of the amplitude.

Table 2.4: Parameters of the newly confirmed DPV TYC 5353-1137-1 and its orbital (P_o) and long period (P_l). Epoch for both the minimum brightness of the orbital light curve and the maximum brightness of the long-cycle light curve are given.

ASAS-ID	Other ID	RA (2000)	DEC (2000)	P_o (days)	P_l (days)	$T_0(\min_o)$ -2450000	$T_0(\max_l)$ -2450000	V (ASAS) (mag)
060418-1009.4	TYC 5353-1137-1	06:04:18.0	-10:09:24.0	2.028(1)	60.455(6)	4491.602390	4404.77653	11.56

2.3. TYC 5353-1137-1: AN ENIGMATIC DOUBLE PERIODIC VARIABLE OF SEMIREGULAR AMPLITUDE

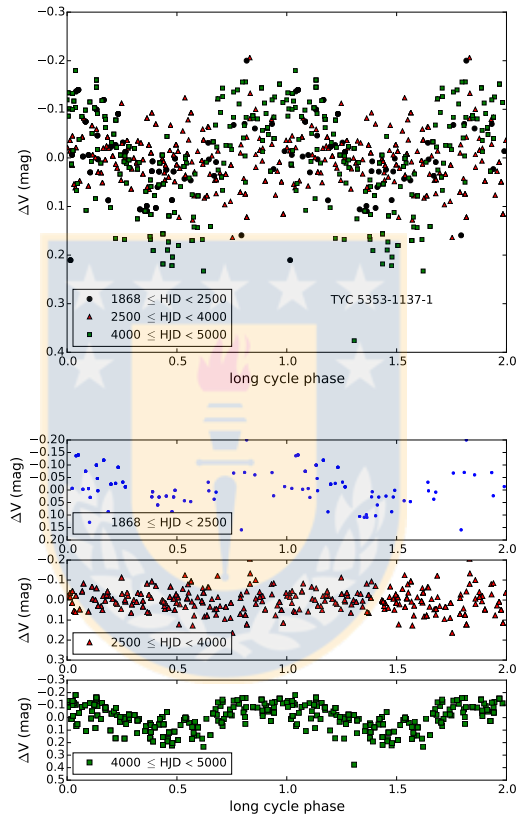


Figure 2.6: The long cycle phase has been disentangled and separated in three datasets (-2450000.0). The first dataset shows less amplitude in the light curve of the long cycle (blue), during the second epoch occurs an effect of switch off (red), and the third dataset shows a remarkable increase in the amplitude of variability (green). Note the different y-axis scales in the panels.



Chapter 3

A new sub-orbital period in DD CMa with partial evidence of accretion disk

Rosales, J.A.¹, Mennickent, R.E.¹, Djurašević, G.^{2,3}, González, F.⁴, Araya, I.⁵, Curé, M.⁶, Cabezas, M.⁷

¹ *Departamento de Astronomía, Universidad de Concepción, Casilla 160-C, Concepción, Chile.*

² *Astronomical Observatory, Volgina 7, 11060 Belgrade 38, Serbia.*

³ *Isaac Newton Institute of Chile, Yugoslavia Branch, 11060 Belgrade, Serbia.*

⁴ *Instituto de Ciencias Astronómicas, de la Tierra y del Espacio (CONICET-Universidad Nacional de San Juan), CC 49, 5400 San Juan, Argentina*

⁵ *Núcleo de Matemáticas, Física y Estadística, Facultad de Estudios Interdisciplinarios, Universidad Mayor, Chile.*

⁶ *Instituto de Física y Astronomía, Facultad de Ciencias, Universidad de Valparaíso, Chile.*

⁷ *Astronomical Institute of the Academy of Sciences of the Czech Republic, Bocniřll 1401/1, Prague, 14100, Czech Republic.*

In preparation for: Monthly Notices of the Royal Astronomical Society

3.1 Abstract

We presents a detailed photometric and spectroscopic analysis of the Double Periodic Variable DD CMa whose main characteristic is that presents an extremely-short orbital period of $P_o = 2.0084 \pm 0.0001$ d. In addition we detected a sub-orbital period $P_s = 0.335 \pm 0.001$ d using ASAS light curve which could be related to cyclic changes on the accretion disk of the gainer star. The equivalent width of H α profile shows a cyclical variation of $0.5P_o$ the orbital period with a mean 1.4229 ± 4.805 Å, possibly related to escaping material caused by the direct impact of the stream on the accretion disk. Through a spectroscopic analysis we determined the fundamental parameters and features for a slightly evolved donor star of $M_2 = 1.81 \pm 0.06 M_\odot$ and temperature $T_2 = 9670 \pm 200$ K. The hot star has a mass $M_1 = 6.60 \pm 0.07 M_\odot$ and $T_1 = 21000 \pm 1000$ K and is surrounded by and small optical and geometrically thick accretion disk of extension $R_d = 5.4 \pm 0.1 R_\odot$ and outer side temperature $T_d = 8410 \pm 200$ K. The system is seen under inclination $84^\circ.1 \pm$

$0^\circ.1$ at a distance $d = 1553.427 \pm 506.499$ pc.

3.2 Introduction

The first double-lined spectroscopic binary was discovered the previous millennium by the astronomer [Pickering \(1890\)](#), since that date many more spectroscopic binaries of those type continue to appear. One hundred thirteen years later, [Mennickent et al. \(2003\)](#) discovered for first time a new type of spectroscopic binary stars, based on a inspection of the OGLE-II database of a group of blue variable stars in the Large Magellanic Cloud(LMC) and the Small Magellanic Cloud (SMC), which were dubbed Double Periodic Variable stars (DPV). These DPV stars showed a second photometric variability which was linked of some way to orbital period of the system, whose enigmatic value is in average 33 times the orbital period ([Mennickent et al., 2016](#); [Mennickent, 2017](#); [Poleski et al., 2010](#); [Pawlak et al., 2013](#)). Years later the first spectroscopic studies of these DPVs started to appear, wherein was reported the evidence of cyclically variable bipolar wind ([Mennickent et al., 2012](#)), and sub-orbital frequencies in the residuals of the V-band light curve which were interpreted as pulsations of the hot companion ([Barría et al., 2013](#)). In addition these show a constancy in their orbital periods, even undergoing Roche Lobe Over Flow (RLOF) mass transfer ([Garrido et al., 2013](#)), cannot be explained in terms of the mechanism of mass and angular momentum loss proposed by [van Rensbergen et al. \(2008, 2011\)](#). However, the second variability in Algol-type stars is not something new, even already had been reported by the astronomer [Soderhjelm \(1980\)](#) in β Per and he tried to explain that this variation was not related to the orbit of the system. Years later, other astronomers such as [Sarna et al. \(1997\)](#); [Meintjes \(2004\)](#); [Peterson et al. \(2010\)](#) tried to explain the second observed photometric variability by means of a mechanism of cyclical magnetic activity produced in the outer zone of convection of the star, which would cause changes in the orbital period at a scale of 10 years. From that moment, new studies started to analyze the possibility of dynamos existence in Algol-type stars and describe episodes of magnetized mass transfer in the cataclysmic variable AE Aquarii, in addition appears the first reports of magnetic activity in the most evolved star of a close binary Algol-type. Currently [Schleicher & Mennickent \(2017\)](#) have proposed an explanation based on magnetic cycles of stellar dynamos in the most evolved star, based on the Applegate mechanism ([Applegate & Patterson, 1987](#)). Whose evidences have already begun to appear in systems such as V393 Scorpii ([Mennickent et al., 2012](#)) and V495 Centaurii ([Rosales Guzmán et al., 2018](#)).

Normally in the spectrum of a Double Periodic Variable (DPV), two set of spectral lines can be observed which oscillates in opposite directions, which we called as double lined spectroscopic binary or a DPV sb2. DD CMa is a DPV that at first glance seems to be a spectroscopic binary sb1, in addition it is poorly studied to date and was catalogued as Eclipsing Algol Semi-Detached (EA/SD). The eclipsing interacting binary DD CMa (ASAS ID 072409 -1910.8, $\alpha_{2000} = 07 : 24 : 09$, $\delta_{2000} = -19 : 10 : 48$, $V = 11.56 \pm 0.11$ mag, $B-V = 0.1 \pm 0.19$ mag)¹ is a system characterized by an extreme short orbital period of 2.0084 ± 0.0001 days and a long period of 89.18 ± 0.16 days. Those values were determined by [Rosales G. & Mennickent \(2017\)](#) using the ASAS² catalogue ([Pojmanski, 1997](#)).

In Section 2 we present a new photometric analysis of DD CMa. In Section 3 we present a summary of spectroscopic data acquired and methods of data reduction. In Section 4 we give the orbital parameters of the system, and present the physical parameters of both stars through a minimization of deviation between a theoretical normalized spectrum a the observed one. In Section 5 we have modeled the light curve a through an inverse method using a theoretical light curve of a binary system considering the light contribution of both components and an accretion

¹<http://simbad.u-strasbg.fr/simbad>

²<http://www.astrouw.edu.pl/asas/?page=acvs>

disk. In Section 6 we have analyzed the reddening and determined the distance of the system. Finally, in Section 7 we presents the main results of our research.

3.3 Photometric analysis

The photometric nature of DD CMa is of a typical Algol, although it does not present great differences with other systems, we noted a peculiar characteristic in its photometry. Thus, we implemented a new photometric analysis to the ASAS light curve, using the 466 better-quality data-points labeled as A-type, and performed a statistical analysis using histogram of 100 bins and compared with a normal distribution of 466 random data (dashed red line), a mean $\mu = 11.533$ and sigma $\sigma = 0.053$. We noted that the photometry present a non-normal distribution and it is skewed towards the left, in addition the extra contribution could be related to the third period (Fig. 3.1). Later, over this data set was implemented a polynomial fit of order 30 to verify the existence of a new short cycle between the orbital phases $0.1 < \phi_o < 0.4$ and $0.6 < \phi_o < 0.9$, which is observed on the light curve of the orbital phase (Left - Fig. 3.2).

After that we noted a new eclipse on the light curve and through an algorithm developed by Kolaczowski to disentangle multi-periodic light curves, first we determined the main frequency f_1 which usually is the orbital through of least-square fit applied over the light curve using a fitting function consisting in a sum of sine functions of variable amplitudes and phases representing the main frequency and their additional harmonics. Later we analyzed the residuals to find a new periodicity f_2 and their new harmonics and periodicity are include in the new fitting procedure to obtain the best light curve based on Fourier components of frequencies. So in this way, we have disentangled and obtained a third sub orbital frequency not reported at our previous report [Rosales G. & Mennickent \(2017\)](#) (Right - Fig. 3.2), whose full amplitude in V-band is $\sim 16.7\%$ the mean total brightness.

To estimate the errors in our measurements, the data set was analyzed by Phase Minimization Dispersion (PDM-IRAF) ([Stellingwerf, 1978](#)) and were estimated a visual inspection of the light curve phased with trial periods close the minimum of the periodogram given by PDM, revealing us a new sub-orbital period $P_{sub} = 0.3335 \pm 0.0001$ d, frequency $f_3 = 2.9985 \pm 0.0009$ d⁻¹ and the epoch of minimum $HJD_3 = 2763.520 \pm 0.10$ d. Is important emphasize that due the orbital period is extreme short, might let small space for the existence of an accretion disc. In addition, the third sub orbital frequency could be interpreted as cyclic changes in the accretion according to ([Garcés L et al., 2018](#)) disk or pulsation coming from the hottest star, similar to the case reported by [Barría et al. \(2013\)](#).

Table 3.1: Parameters of the Double Periodic Variable DD CMa and its sub-orbital period (P_s) incorporated, the orbital (P_o) and long period (P_l), with their respective epochs for the minimum and maximum brightness.

ASAS-ID	Other ID	RA (2000)	DEC (2000)	P_s (days)	P_o (days)	P_l (days)	$T_0(\text{sub.})$ (-2450000)	$T_0(\text{min}_o)$ (-2450000)	$T_0(\text{max}_l)$ (-2450000)	V (ASAS) (mag)
072409-1910.8	DD CMa	07:24:09	-19:10:48	0.3335(1)	2.0084(1)	89.18(16)	2763.520	2763.46515	4207.411	11.41

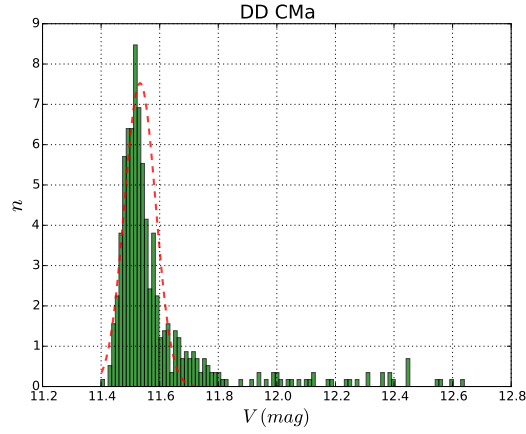


Figure 3.1: Histogram of magnitude for DD CMa using 100 bins for 466 ASAS A-type data, showing a skewed distribution towards the left side. The dashed red line corresponds to a normal distribution of 466 random data with mean $\mu = 11.533$ and sigma $\sigma = 0.053$.

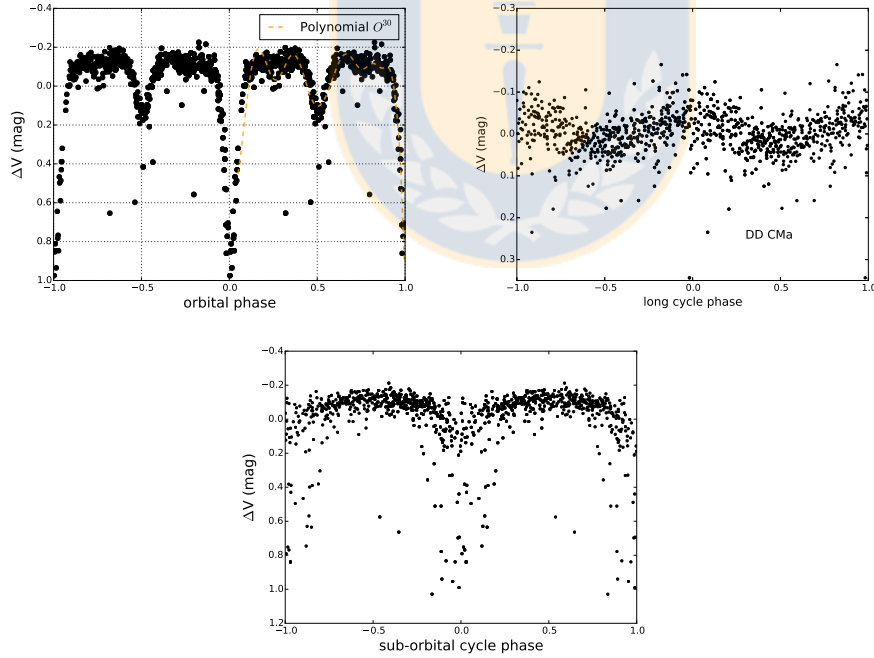


Figure 3.2: Disentangled ASAS V-Band light curve for the orbital phase with orbital period $P_o = 2.0084(1)$ d (left), a long period $P_l = 89.18(16)$ d (right) and the third sub-orbital period $P_{sub} = 0.3335$ d (down) for DD CMa after disentangling.

3.4 Spectroscopic observations

We conducted a spectroscopic observation for DD CMa (proposal ID CN2018A-4), using the CHIRON spectrograph in Cerro Tololo Interamerican Observatory obtaining a set of 10 spectra obtained the year 2018 and well distributed with a mean SNR ≈ 73.05 (Table 3.1). The corrections of every spectrum with flat, bias, and wavelength were done with IRAF, and normalized to the continuum and corrected by heliocentric rest frame. Due that the strength of measurements of the radial velocities are not affected (RVs) by the sky, then we have not developed a flux calibration. Our observation cover around of $\approx 60\%$ of the orbital variability and the long-term periodicity, with a spectral range from 4505 to 6859 Å. In addition we determined the following ephemeris for the light curves and these will be used in the analysis of the rest paper:

$$HJD_{min,orbital} = 2452763.46515 + 2.0084(1) \times E, \quad (3.1)$$

$$HJD_{min,sub.} = 2452763.520 + 0.3334(1) \times E, \quad (3.2)$$

$$HJD_{max,long} = 2454207.411 + 89.18(16) \times E, \quad (3.3)$$

Table 3.2: Summary of spectroscopic observation, wherein N corresponds to the number of spectra, HJD at mid-exposure for the first spectrum series is given, ϕ_o and ϕ_l are the orbital and long cycle phase respectively, and are calculated according to the Eq. 3.2 and Eq. 3.3. The spectral resolution $R \sim 25000$ (fiber mode).

UT-dat	Observatory/Telescope	Instrument	N	exptime (s)	HJD	ϕ_o	ϕ_l	S/N	R
29-01-2018	CTIO/1.5m	CHIRON	1	3600	2458148.70016472	0.3558129455727794	0.1947652469175054	93.52	25000
30-01-2018	CTIO/1.5m	CHIRON	1	3600	2458149.64994756	0.8287181636451351	0.2054154245355377	74.26	25000
12-02-2018	CTIO/1.5m	CHIRON	1	3600	2458162.67824674	0.3156227542940542	0.3515053458167614	76.97	25000
13-02-2018	CTIO/1.5m	CHIRON	1	3600	2458163.58789418	0.7685442042402428	0.3617054740974481	49.83	25000
26-02-2018	CTIO/1.5m	CHIRON	1	3600	2458176.57952628	0.2371919338734187	0.5073842372752324	87.41	25000
27-02-2018	CTIO/1.5m	CHIRON	1	3600	2458177.57591138	0.7333008264404270	0.5185569789194560	55.64	25000
12-03-2018	CTIO/1.5m	CHIRON	1	3600	2458190.53965503	0.1880626517186101	0.6639230211922680	85.44	25000
13-03-2018	CTIO/1.5m	CHIRON	1	3600	2458191.52936314	0.6808470125156418	0.6750208919057030	59.95	25000
26-03-2018	CTIO/1.5m	CHIRON	1	3600	2458204.50431538	0.1411896932609124	0.8205126191989152	68.86	25000
27-03-2018	CTIO/1.5m	CHIRON	1	3600	2458205.48963719	0.6317900766525781	0.8315613051150805	78.63	25000

3.5 Spectroscopic analysis

3.5.1 Radial velocities

We found a set of characteristic absorptions lines that represent the movement of both stellar components, wherein we have measured the radial velocity of donor and gainer separately of manual form. We used a deblending method of IRAF to deblend a group or blend of lines into single components, which allow us to adjust several functional forms, in which we used the Gaussian fits for the absorption lines. We have identified a set of absorption lines for the gainer He I (4713), H β (4861.33), He I(4921.92), He I (5875), H α (6562.817), He I(6678.149), while for the donor were H β (4861.33) and H α (6562.817), later we measured their radial velocities and in addition the velocities were corrected to the absolute heliocentric system, the donor velocities are given in Table 3.3.

The measured radial velocities for the component less massive (donor) were obtained using H α and H β , while for the more massive and hotter companion we measured He I (4713), He I(4921), He I (5875) and He I (6678), see Table 3.4. The radial velocities for the donor were fitted using a sine function implementing a Marquart-Levenberg method of non-linear least squares, wherein the solutions and respective errors are obtained through an iterative succession of local linearization of the problem. We obtained an amplitude $K_2 = 267.825 \pm 7.268 \text{ km s}^{-1}$ and a zero point $0.376 \pm 5.328 \text{ km s}^{-1}$, for the case of the gainer the RV were fitted using a sine function of amplitude $K_1 = 73.271 \pm 1.150$ and zero point 0.376 ± 0.727 , both solutions assume a circular orbit (Fig. 3.3). The radial velocity curve shown a lag in their phases, probably this caused by the sub-orbital period and the brightness contribution of the disc in the absorption lines.

Table 3.3: Radial velocities of the donor and their respective errors, using H α (6562.8 Å) and H β (4861.33 Å)

	HJD	RV (km s ⁻¹)	error (km s ⁻¹)
H α	2458148.70016472	242.898	9.164
	2458149.64994756	-236.882	9.167
	2458162.67824674	288.011	9.167
	2458163.58789418	-284.783	9.173
	2458176.57952628	231.391	9.166
	2458190.53965503	183.955	9.164
	2458191.52936314	-179.023	9.172
H β	2458148.70016472	238.646	8.144
	2458149.64994756	-273.431	8.148
	2458162.67824674	285.829	8.145
	2458176.57952628	260.598	8.136
	2458190.53965503	187.982	8.139
	2458191.52936314	-183.892	8.142

We have used a public subroutine written by Charbonneau (1995) in Fortran 77 and based on a genetic algorithm called PIKAIA³ to obtain the orbital parameters for DD CMA. The task consists in finding the single parameter set that minimizes the difference between the model's predictions and the data producing a series of theoretical velocities and finding the best parameters through a minimization of chi-square defined as:

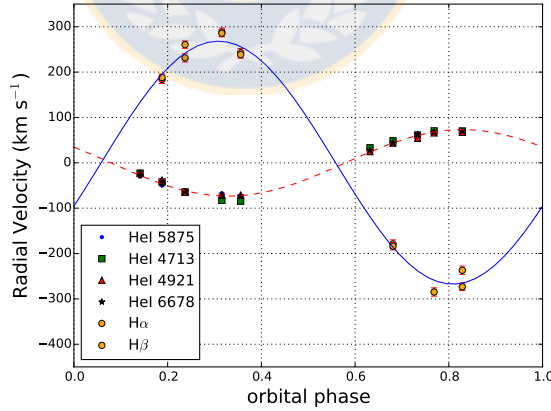
$$\chi^2(P_o, \tau, \omega, e, K_2, \gamma) = \frac{1}{N-6} \sum_{j=1}^N \left(\frac{V_j^{obs} - V(t_j; P_o, \tau, \omega, e, K_2, \gamma)}{\sigma_j} \right)^2, \quad (3.4)$$

wherein N corresponds to the number of observations, the parameter V_j^{obs} is the radial velocity

³<http://www.hao.ucar.edu/modeling/pikaia/pikaia.php>

Table 3.4: Radial velocities of the gainer and their respective errors, using He I (4713 Å), He I (5875 Å)

	HJD	RV (km s ⁻¹)	error (km s ⁻¹)
He I (4713)	2458148.70016472	-84.617	2.125
	2458149.64994756	70.206	2.125
	2458162.67824674	-82.994	2.125
	2458163.58789418	70.370	2.125
	2458176.57952628	-64.143	2.125
	2458177.57591138	61.244	2.131
	2458190.53965503	-42.313	2.128
	2458191.52936314	48.467	2.125
	2458204.50431538	-22.786	2.127
	2458205.48963719	33.042	2.126
He I (5875)	2458149.64994756	71.5111	0.8409
	2458162.67824674	-67.3785	0.8374
	2458163.58789418	69.0041	0.8413
	2458176.57952628	-60.3940	0.8379
	2458177.57591138	57.1871	0.8390
	2458190.53965503	-49.9766	0.8368
	2458191.52936314	45.3391	0.8399
	2458204.50431538	-30.0559	0.8373
	2458205.48963719	24.0909	0.8376

Figure 3.3: Radial velocities of the donor using HeI (4713, 4921, 5875, 6678) and for the gainer H α and H β measured through Gaussian fits. Both fits were using a sinusoidal adjustment assuming a circular orbit.

observed in the data set, and $V(t_j; P_o, \omega, e, K_2, \gamma)$ is the radial velocity at the time t_j . The other parameters such as P_o represents the orbital period, τ the time passage per the periastron, ω is the periastron longitude, e the orbital eccentricity and K_2 the half-amplitude of the radial velocity of

the center mass of the system. The theoretical radial velocities are computed through the equation 2.45 given by [Hilditch \(2001\)](#) defined as:

$$V(t) = \gamma + K_2(\cos(\omega + \theta(t)) + e\cos(\omega)), \quad (3.5)$$

to resolve the equation 3.5 first is necessary to know the angular parameter θ called true anomaly, for this we must solve the equation 3.7 obtaining a solution for the eccentric anomaly E , and later using this solution we solve the equation 3.6, finally we are enabled to obtain the theoretical radial velocity using the equation 3.5.

$$\tan\left(\frac{\theta}{2}\right) = \sqrt{\frac{1+e}{1-e}} \tan\left(\frac{E}{2}\right), \quad (3.6)$$

$$E - e\sin(E) = \frac{2\pi}{P_o}(t - \tau), \quad (3.7)$$

Through this test of chi-square implemented by PIKAIA which make a variation of the six parameters we obtained a global optimization, later was necessary to develop a Monte Carlo Simulation to get reliable error estimates on the global solution, see Table 3.5.

Table 3.5: Orbital parameters for the gainer of DD CMa obtained through minimization of χ^2 given by equation 3.4. The value $\tau^* = \tau - 2450000$ is given and the maximum and minimum are one isophote of 1σ .

Parameter	Best Value	Lower limit	Upper limit
$P_o(d)$	1.756	1.754	1.757
τ^*	8149.794	8149.760	8149.827
e	0.098	0.069	0.127
$\omega(rad)$	0.745	0.632	0.867
$K_2(kms^{-1})$	72.056	69.733	74.383
$\gamma(kms^{-1})$	-6.437	-7.999	-4.899
N	39		
χ^2	9.313		

Is necessary remember that the photometry obtained with ASAS measures the power of the optical radiation of the visible spectrum, while the spectroscopy of CHIRON it is based on detecting the absorption or emission of electromagnetic radiation at certain wavelengths. To determine the orbital period of the system we have used both methods and we noted that there is a small difference of 0.252 ± 0.001 d with respect to the photometric value at the moment to use PIKAIA and implement a Monte Carlo simulation on the global solution. We emphasize that the simulation search the minimum possible value, adjusting and compensating their evaluations with respect to

the number N , wherein the absolute error decrease as $1/\sqrt{N}$ and probably this difference between orbital periods is due to we have ten spectra of which was not covered homogeneously the orbital phase and we selected four absorption lines with a total of 39 Radial velocities, while for the photometry we have 466 data points covering completely the orbital phase.

However, the result of of 0.252 days reinforces the idea of that the component more brilliant probably presents cyclically changes on the accretion disc. The difference between the photometric orbital period and the best value given in the Table 3.5 say us that the sub orbital period is around 0.252 d, that mean that it is a 34% smaller than the obtained through photometry. For the next sections we will use the orbital period from photometric analysis and the orbital parameters given in the Table 3.5 as a first approximation.

3.5.2 Spectral disentangling

Every spectrum was unraveled using an iterative method proposed by [González & Levato \(2006\)](#), which allows to calculate the spectra and RVs of two stellar components of a binary system, using alternately the spectra of one component to calculate the spectrum of the other. In this way, each step eliminates spectral characteristics of the spectra observed to finally measure the RVs of each component in an isolated manner. The method used will depend on the previous result, so it is executed iteratively until convergence is assured. For that we have used the theoretical radial velocities obtained from the sinusoidal fits in the previous section and performed five iterations for both components, attaining successfully unraveling both spectra and obtaining an observed average spectrum from the gainer and donor star, which is called as template.

Later that the spectra were disentangles, we have analyzed the $H\alpha$ emission for the gainer star and we noticed the presence of slightly double peak $H\alpha$ emission, which confirms the interacting binary nature, in addition confirm us that there a enough space between both components for the presence of an accretion disk. Therefore, it is evidence that the DD CMa is semi-detached system with a circumstellar disk in formation and the $H\alpha$ profile of the hot star show a central absorption, revealing the presence of obscuring material through the line of sigh (Fig. 3.4).

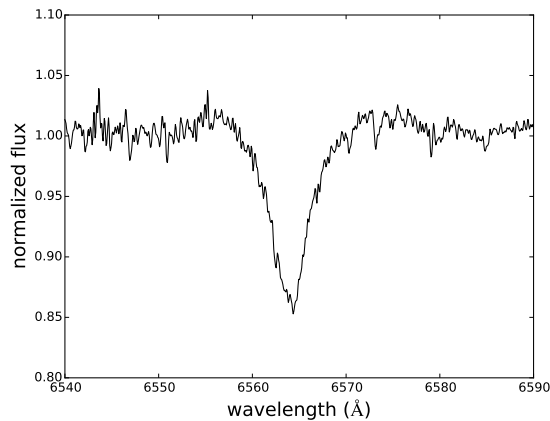


Figure 3.4: Disentangled $H\alpha$ profile of gainer star, showing slightly homogeneous and similar peaks, probably caused by the accretion disk.

3.5.3 Determination of gainer physical parameters

The determination of the physical parameters was performed through a detailed analysis of certain characteristic absorption lines that represents to the gainer star. Due that the most contribution at the spectra comes from of the hot component, we used the observed average spectrum of the gainer star (Template $\mathfrak{5}$) and analyzed through a χ^2 test statistic comparison with theoretical spectra constructed using a stellar spectral synthesis program called SPECTRUM⁴, which has been written in C and uses atmospheric models computed of ATLAS9⁵ (Castelli & Kurucz, 2004) in Local Thermodynamic Equilibrium (LTE). This consists in the minimization of the deviation between theoretical normalized spectrum and the observed spectrum of the gainer star, which must be corrected by a veiling factor. The theoretical model were computed using 2 groups of effective temperatures from $9000 \leq T_{1,eff} \leq 11000$ K with steps of 250 K and the other group $11000 \leq T_{2,eff} \leq 39000$ K with steps of 1000 K, surface gravity from 1.5 to 5.0 dex with steps of 0.5 dex, macro-turbulent velocity from 0 to 10 km s⁻¹ with steps of 1 km s⁻¹, v_{sini} from 0 to 80 km s⁻¹ with steps of 5 km s⁻¹ and two groups of micro-turbulent velocity by default of 0.0 and 2.0 km s⁻¹ a fixed parameter of stellar metallicity [M/H]=0 with a fixed mixing length parameter $l/H=1.25$ for default from the grid, in addition we incorporated a correction by veiling factor from 0.0 to 0.9 with steps of 0.05 (dimensionless), it is a factor of constant proportionality between the theoretical spectrum and the observed. The implemented method converged successfully to a minimum chi-square at effective temperature of the gainer $T_g = 21000 \pm 1000$ K, surface gravity $\log g = 4.5 \pm 0.5$ dex, $v_{mac} = 2.0 \pm 0.5$ km s⁻¹, $v_{mic} = 2.0$, $v_{1r} \sin i = 60 \pm 5$ km s⁻¹, [M/H]=0 and $l/H=1.25$, and $\eta = 0.30 \pm 0.05$ with six freedom degrees and a best value of $\chi_6^2 = 0.177$ (Fig. 3.5 and 3.6).

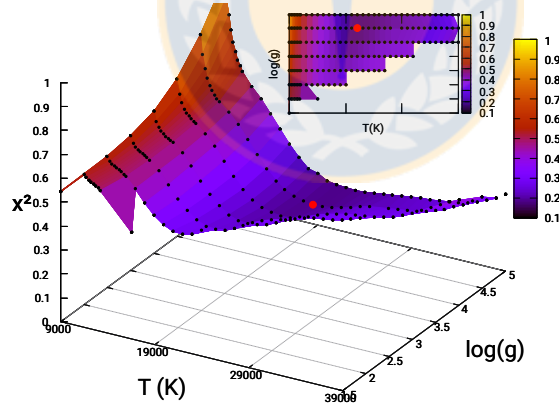


Figure 3.5: Surface color map of chi-square analysis with 6 freedom degrees obtained for the gainer star, and with all other parameters at their optimized values to find the best theoretical normalized spectrum. The best obtained value $\Delta\chi_6^2 = 0.177$ is represented by a red dot at $T= 21000$ K and $\log g = 4.5$ dex.

⁴<http://www.appstate.edu/~grayro/spectrum/spectrum.html>

⁵<http://wwwuser.oats.inaf.it/castelli/grids.html>

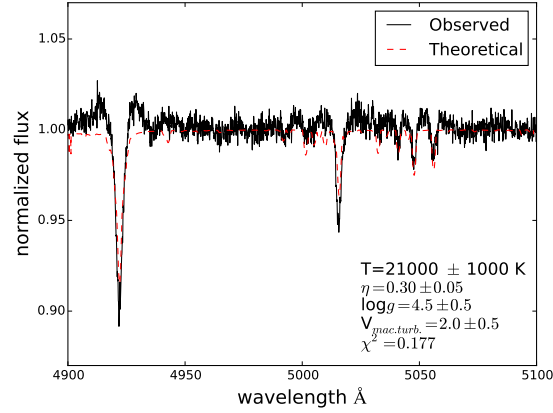


Figure 3.6: Detailed comparison between the observed (black line) and theoretical (red line) gainer spectrum.

3.5.4 The H α emission line profile

We analyzed the H α profile of the hot star (gainer) which presents a slightly double peaks emission. Both emission peaks has similar intensities, but probably it is due to an accretion disk. We performed a measure of intensity of the spectra with donor contribution subtracted and centered in 6562.8 Å (Fig. 3.7). In addition we quantified the parameter V/R defined as $V/R = (I_v)/(I_r - 1)$ which is in terms of the peaks intensities relative to the normalized continuum, and we noted that this ratio tends slightly to vary with the orbital period (Fig. 3.8 - bottom panel). Thus, we performed a polynomial fitting of 5rd order considering a confidence interval region of 95% of the mean V/R to analyze the behavior of obtained values. i.e. we incorporated a band of confidence which provide a representation of the uncertain about of the regression line. The results suggest us that the accretion disk is in a formation stage, but too presents a increase of the values between the orbital phases $0.6 \leq \phi \leq 0.9$. This minimum increase indicate us a possible material escaping from the system, which would be related to the impact of stream in the hot spot of the disk. The equivalent width (EW) of H α profile shows a cyclical behavior which varies with the orbital period and similar characteristics, for that we have performed a polynomial fitting of 4rd order ($f(x)=a+bx+cx^2+dx^3+ex^4$) with a confidence interval region of 95% with respect to the mean EW and we noted a increase in the quadrature $\phi_o = 0.733$, in addition we performed a sinusoidal fitting ($g(x)=a+b\cos(2\pi x + c)$) with a orbital period fixed at $0.5 P_o$ (dashed line Fig. 3.8) and we obtained a mean EW is 19.4229 ± 4.805 Å and an amplitude of 21.4656 ± 6.433 Å (Table 3.6).

3.5.5 Gainer, mass ratio and circumstellar matter

Apparently DD CMA is a double-lined spectroscopic binary, i.e. is a SB2 type. At the most of the obtained spectra, principally is observed the more brilliant component, in which its companion

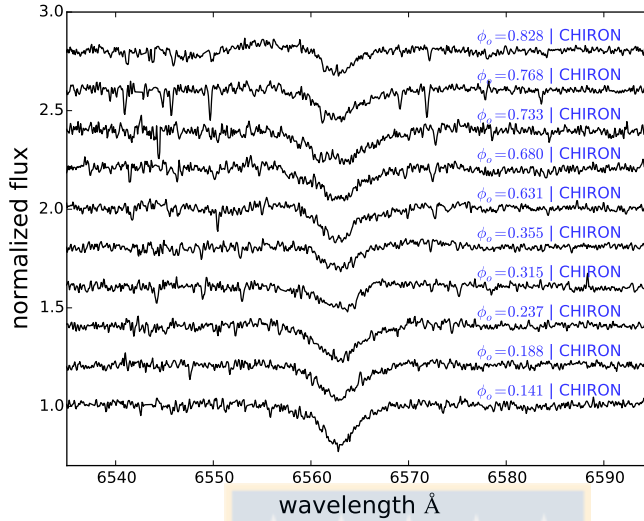


Figure 3.7: Comparison of $H\alpha$ profiles centered at 6562.8 \AA and with the donor contribution subtracted, during a complete orbital cycle.

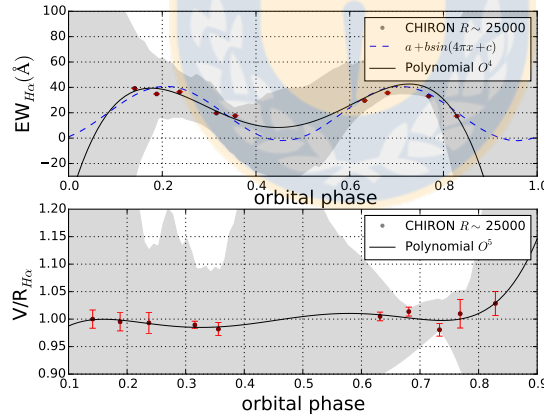


Figure 3.8: Equivalent width of $H\alpha$ profile of the gainer star during a complete orbital cycle (Top). The continuum black line is fitted 4th order polynomial to the mean EW, while the blue line corresponds to sinusoidal fit using least squares with of three free parameters. (Bottom) Violet and red intensities (V/R) ratio of $H\alpha$ profile measured from the continuum of the gainer with donor contribution subtracted, and the black line corresponds to 5th order polynomial fit. Every polynomials fits presents a confidence interval region of 95% with respect to the mean, wherein is bigger at the regions without values.

is slightly observed shifting the form of the $H\alpha$ and $H\beta$ profiles. Thus, we have assume that the velocity obtained in the Section 3.5.1 represents both components and we have computed a mass

Table 3.6: Free parameters of the sinusoidal and polynomial fits obtained for equivalent width (EW) and violet and red intensities of the H α profile of the gainer star.

Type	a (Å)	err (Å)	b (Å)	err (Å)	c (Å)	err (Å)	d (Å)	err (Å)	e (Å)	err (Å)
Sinusoidal	19.423	4.805	-21.466	6.433	14.673	0.188	-	-	-	-
Polynomial	-52.678	59.800	1299.990	694.600	-6036.630	2647.000	10220.800	3952.000	-5679.300	2015.000

ratio of $q = 0.274 \pm 0.012$.

Due that the system presents a extremely-short orbital period is possible that the gainer star is in critical non-synchronous rotation regime. Is for that we need some idea of the geometry of the critical surface, which depends of the mass ratio q and the orbital separation a , and using the approximate analytic formula proposed by [Eggleton \(1983\)](#) we can know the ratio between the effective radius and the orbital separation using the following equation:

$$\frac{R_L}{a} = \frac{0.49q^{2/3}}{0.6q^{2/3} + \ln(1 + q^{1/3})}, \quad (3.8)$$

wherein R_L is the effective radius and a the orbital separation, thus we computed that ratio is $R_L/a = 0.274 \pm 0.153$. In addition, we computed the relation between the mean density $\bar{\rho}$ (g cm^{-3}) as a lobe-filling star and the critical orbital period (days) using the following equation:

$$P_{cr}\sqrt{\bar{\rho}} = \left(\frac{3\pi}{G}\right)^{1/2} \left(\frac{q}{1+q}\right)^{1/2} x_L^{-3/2}, \quad (3.9)$$

where x_L corresponds to the R_L/a ratio and it is in units of the orbital separation. We obtained that the critical orbital period as a function of the mean density $P_{cr}\sqrt{\bar{\rho}} = 0.444 \pm 0.090$. Then for a binary as DD CMa of a period of few days, is necessary understand that in term of $\bar{\rho}$ which can be determined solely by the following equation which depend only of the orbital period of the system:

$$\bar{\rho} = \frac{3M_d}{4\pi R_2^3} \cong \frac{3^5}{8GP^2}, \quad (3.10)$$

thus the obtained value to the mean density is $\bar{\rho} = 0.04748 \pm 0.00005 \text{ g cm}^{-3}$, which it means that the star belongs to the upper main sequence and filled its Roche lobe ([Kippenhahn et al., 2012](#); [Frank et al., 2002](#)).

3.5.6 Mass constraints from spectroscopy

Until now just we have determined some parameters using the mass ratio of the system, but too we can estimate the mass of each one using the mass function, which represents the minimum possible mass for the unseen star and unknown orbital inclination in an elliptical orbit ([Hilditch, 2001](#)). Due that the system presents a short orbital period is highly probable that the eccentricity is null or close to zero, i.e. a circular orbit. This we can estimate the mass function through following equation:

$$f = 1.0361 \times 10^{-7} (1 - e^2)^{3/2} \left(\frac{K_2}{\text{km s}^{-1}} \right)^3 \frac{P_o}{\text{days}} M_\odot, \quad (3.11)$$

wherein the parameter e corresponds to the eccentricity, K_2 the half amplitude of the RV of the donor and P_o the orbital periods measured in days. Thus, using an eccentricity $e = 0.098 \pm 0.015$ and $K_2 = 267.825 \pm 7.268$, we obtained that the mass function of the donor is $f = 3.959 \pm 0.154 M_\odot$. Therefore, with the known mass function of the donor and the 1.3a and 1.3b equations of [Eggleton \(2006\)](#), we can estimate the mass for both components:

$$M_d \sim 1.25q(1+q)^2 f, \quad (3.12)$$

$$M_g \sim 1.25(1+q)^2 f, \quad (3.13)$$

where the mass ratio is $q = M_2/M_1$. We computed and the estimated that mass of the donor is $M_d \sim 2.201 M_\odot$ while for the gainer is $M_g \sim 8.032 M_\odot$.

3.6 Light curve model and system parameters

3.6.1 The fitting procedure

The main physical parameters of every component of DD CMA were obtained performing a fitting to the V-band light curve, using the inverse problem solving method based in the algorithm developed by [Djurašević \(1992, 1996\)](#). The inverse method consist in a determination of the optimal values yielding the best fit between the observed light curve and the theoretical, resolving in an iterative cycle of corrections to the model elements based on a nonlinear least-square method, which depends of some determined parameters previously of independent way at the previous sections. The algorithm disentangling the orbital light-curve for a binary with or without accretion disk, and later this providing us the the flux contribution of each component separately, and the stellar and disc parameters.

The used initial parameters were the computed at the Section 3.5.3 for the gainer star and we adopted a semi detached configuration with a donor star filling the Roche lobe, including an optically thick accretion disk around of the gainer, in addition we considered a hot spot located on the edge side of the disk. We must emphasize that the model used follow results of hydrodynamical simulations of gas dynamics in interacting close binary stars by [Bisikalo et al. \(1998, 1999, 2003\)](#) and has been tested in several studies for DPV stars (e.g. [Mennickent et al. \(2012\)](#); [Barría et al. \(2013\)](#); [Garrido et al. \(2013\)](#); [Mennickent et al. \(2015\)](#); [Rosales Guzmán et al. \(2018\)](#))

3.6.2 The best light-curve model

The best found model for DD CMA given in the Table 3.7, suggest us that the system has an inclination $i^\circ = 84.1 \pm 0.1$, which explain the central absorption in $H\alpha$ provoked by the accretion disk and we are not seen a luminous disk in our line sight. In addition the gainer star has a temperature of $T_g = 21000 \pm 1000$ K, $R_g = 3.32 \pm 0.08 R_\odot$ and is surrounded by an accretion disc of radius $R_d = 5.4 \pm 0.1 R_\odot$ and central vertical thickness $d_c = 0.2 \pm 0.1 R_\odot$ and an edge thickness is $d_e = 1.3 \pm 0.1 R_\odot$, i.e. is surrounded by a concave accretion disk with temperature $T_d = 8410 \pm 200$ K. In addition presents a hot spot with temperature of $T_{hs} = 10428 \pm 418$ K and a bright spot

$T_{bs} = 9251 \pm 402$ K. While the companion its temperature is $T_d = 9670 \pm 200$ K and has radius $R_d = 3.72 \pm 0.07 R_{\odot}$ which quite similar to the gainer.

In the Figure 3.9 we shown the observed light curve, synthetic and the O-C residual between the synthetic light curves and the observed of DD CMa, in addition a view of the system during the quadratures $\phi_o = 0.18, 0.53, 0.68$ and 0.98 , wherein observe the hot spot, bright spot and the deformed cold star or donor.

3.7 Distance determination

In this section we determined the distance of DD CMa using a classical method proposed by Clausen (2004). With this method we can determine the distance based on the distance modulus of both components observed in V band, using the following equation:

$$(m_{d,g} - M_{d,g})_0 = 5 \log(R_{d,g}/R_{\odot}) + (m_{d,g} - A_V) - M_{bol\odot} + 10 \log(T_{d,g}/T_{\odot}) + BC_{d,g}, \quad (3.14)$$

wherein the subindex d, g represents the index for the donor or gainer star, A_V corresponds to the interstellar absorption, $M_{bol\odot}$ is the bolometric magnitude of the Sun and BC is the bolometric corrections which must be applied over each component. We obtained from the dust map IRSA⁶ the color excess $E(B-V)_{SF} = 0.7227 \pm 0.0137$ (Schlafly & Finkbeiner, 2011) using a circle of $2'$ (arcmin). To performs the compute we assumed a visual extinction to the reddening ratio $A_V/E(B-V) = 3.1$ as constant value and we get an interstellar absorption $A_{SF} = 2.2404 \pm 0.0190$. The individual normalized flux contributions were computed in the Section 3.6.2, wherein the contribution from the donor star corresponds to $f_d = 1.050 \pm 0.042$, the gainer has a value of $f_g = 2.4 \pm 0.042$, while the disk contributes with $f_{di} = 0.25 \pm 0.042$. Therefore, we can calculate the apparent magnitudes through of following equation:

$$m_{d,g} - m_t = -2.5 \log \frac{f_{d,g}}{f_t}, \quad (3.15)$$

wherein m_t corresponds to the total apparent magnitude of the system $V = 11.56 \pm 0.11$ SIMBAD⁷. Thus, to solve the equation 3.12 is necessary solve the equation 3.13. We have obtained that the apparent magnitude of the donor is $m_d = 12.928 \pm 0.122$ mag, while the gainer star is $m_g = 12.030 \pm 0.117$ mag, previous bolometric correction according to the values published by Torres (2010) using a $\log(T_d) = 3.985 \pm 0.021$ and $\log(T_g) = 4.322 \pm 0.0476$ and the following bolometric corrections $BC_d = -0.182 \pm 0.078$ and $BC_g = -2.000 \pm 0.165$ according to Flower (1996). Using the computed values for both components we determined the distance modulus using the follow equation:

$$d_{d,g}(pc) = 10^{((m_{d,g} - M_{d,g})_0 + 5)/5}, \quad (3.16)$$

⁶<https://irsa.ipac.caltech.edu/applications/DUST/>

⁷<http://simbad.u-strasbg.fr/simbad/>

thus we computed distance for each component separately, where the distance of the donor is $d_d = 1408.857 \pm 186.650$ pc and for the gainer $d_g = 1697.997 \pm 470.853$ pc, respectively. Therefore the average distance obtained with this method for DD CMa corresponds to $d = 1553.427 \pm 506.499$ pc. However, initially Gaia⁸ has published a distance with DR1 of $d_{Gaia} = 6466.260 \pm 18405.098$ pc and later with DR2 published a second distance of $d_{Gaia} = 2624.743 \pm 254.080$ pc. We think that the differences between our distance and the published by Gaia DR2 is due to applied method and is possible that our system is at a distance that corresponds to the upper limit of the computed error.

3.8 Conclusions

In this work we presented a complete and detailed spectroscopically and photometrically study of the Double Periodic Variable DD CMa, wherein we conclude:

- From a second photometric analysis we found a sub-orbital period whose value possibly could be related to cyclic changes in the accretion disk from the gainer star with a value of $P_{sub} = 0.3335 \pm 0.0001$ d.
- From the analysis with Monte Carlo simulation on the radial velocities we found the best values for orbital parameters given in Table 3.5.
- Through of χ^2 test statistic implemented on the theoretical modeled spectrum, we determined the physical parameter of the gainer star given in Section 3.5.3. We determined that the gainer temperature is $T_g = 21000 \pm 1000$ K, its surface gravity $\log g = 4.5 \pm 0.5$ dex and presents a rotational velocity $v_{1r, sini} = 60 \pm 5$ km s⁻¹, a macro-turbulence velocity $v_{mac} = 2.0 \pm 0.5$ km s⁻¹ for a metallicity of $[M/H] = 0.0$, which converged successfully to the best value $\chi_6^2 = 0.177$ with six freedom degree.
- The slightly or almost nil increase of V/R ratio between the orbital phases $0.6 \leq \phi_o \leq 0.9$, is not conclusive yet to suggest the presence of a small accretion disk with the presence of escaping material caused by the impact of the stream on accretion disk, and it requires a new spectroscopic and photometric monitoring. However, from the analysis of the equivalent width performed for H α profile shown a cyclical variation of $0.5P_o$ orbital period with mean 19.4229 ± 4.805 Å and an amplitude of 21.4656 ± 6.433 Å, which reinforces the hypothesis of cyclic variation on the structure of the accretion disk.
- We developed an analysis of DD CMa light curve using the inverse problem and we obtained the fundamental parameters given in the Table 3.7. Where we determined the donor mass $M_2 = 1.81 \pm 0.06 M_\odot$, its temperature $T_2 = 9670 \pm 200$ K and radius $R_2 = 3.72 \pm 0.07 R_\odot$.
- The gainer star is surrounded by an small and optical and geometrically thick accretion disk of radial extension $R_d = 5.4 \pm 0.1 R_\odot$ with a temperature $T_d = 8410 \pm 200$ K.
- During the quadratures the donor, gainer and the disk contribute with 28.4%, 64.9% and 6.7% of the total flux at the V band of the system.
- The model shown a hot spot located at the edge of the disc with a temperature $T_{hs} = 10428 \pm 418$ K and a bright spot temperature $T_{bs} = 9251 \pm 402$ K.

⁸<http://gea.esac.esa.int/archive/>

- We used a classical method to determine the distance of the system, we found that the distance for DD CMa corresponds to $d = 1553.427 \pm 506.499$ pc.



Table 3.7: Results of the analysis of DD CMa light-curves obtained by solving the inverse problem for the Roche model with an large accretion disk partially obscuring the more-massive (hotter) gainer in critical non-synchronous rotation regime.

Quantity		Quantity	
n	566		
$\Sigma(O - C)^2$	1.0170		
σ_{rms}	0.0424		
$i[^\circ]$	84.1 ± 0.1	$\mathcal{M}_h[\mathcal{M}_\odot]$	6.60 ± 0.07
F_d	0.799 ± 0.02	$\mathcal{M}_c[\mathcal{M}_\odot]$	1.81 ± 0.06
$T_d[\text{K}]$	8410 ± 200	$\mathcal{R}_h[\text{R}_\odot]$	3.32 ± 0.08
$d_e[a_{\text{orb}}]$	0.096 ± 0.004	$\mathcal{R}_c[\text{R}_\odot]$	3.72 ± 0.07
$d_c[a_{\text{orb}}]$	0.013 ± 0.04	$\log g_h$	4.21 ± 0.02
a_T	6.8 ± 0.2	$\log g_c$	3.55 ± 0.02
F_h	1.000	M_{bol}^h	-3.43 ± 0.06
$T_h[\text{K}]$	21000	M_{bol}^c	-0.30 ± 0.05
$T_c[\text{K}]$	9670 ± 200	$a_{\text{orb}}[\text{R}_\odot]$	13.61 ± 0.1
$A_{\text{hs}} = T_{\text{hs}}/T_d$	1.24 ± 0.04	$\mathcal{R}_d[\text{R}_\odot]$	5.4 ± 0.1
$\theta_{\text{hs}}[^\circ]$	23.1 ± 1.2	$d_e[\text{R}_\odot]$	1.3 ± 0.1
$\lambda_{\text{hs}}[^\circ]$	340.2 ± 4.5	$d_c[\text{R}_\odot]$	0.2 ± 0.1
$\theta_{\text{rad}}[^\circ]$	3.0 ± 5.0		
$A_{\text{bs1}} = T_{\text{bs}}/T_d$	1.10 ± 0.04		
$\theta_{\text{bs}}[^\circ]$	46.5 ± 3.7		
$\lambda_{\text{bs}}[^\circ]$	215.1 ± 5.0		
f_h	5.2 ± 0.1		
Ω_h	5.196		
Ω_c	2.408		

FIXED PARAMETERS: $q = \mathcal{M}_c/\mathcal{M}_h = 0.274$ - mass ratio of the components,

$T_h = 21000\text{K}$ - temperature of the more-massive (hotter) gainer, $F_c = 1.0$ - filling factor for the critical Roche lobe of the donor, $f_h = 5.2$; $f_c = 1.00$ - non-synchronous rotation coefficients of the gainer and donor respectively, $\beta_h = 0.25$; $\beta_c = 0.25$ - gravity-darkening coefficients of the gainer and donor, $A_h = 1.0$; $A_c = 1.0$; $A_d = 1.0$ - albedo coefficients of the gainer, donor and disk.

Quantities: n - number of observations, $\Sigma(O - C)^2$ - final sum of squares of residuals between observed (LCO) and synthetic (LCC) light-curves, σ_{rms} - root-mean-square of the residuals, i - orbit inclination (in arc degrees), $F_d = R_d/R_{yc}$ - disk dimension factor (ratio of the disk radius to the critical Roche lobe radius along y-axis), T_d - disk-edge temperature, d_e , d_c , - disk thicknesses (at the edge and at the center of the disk, respectively) in the units of the distance between the components, a_T - disk temperature distribution coefficient, $F_h = R_h/R_{zc}$ - filling factor for the critical Roche lobe of the hotter, more-massive gainer (ratio of the stellar polar radius to the critical Roche lobe radius along z-axis for a star in critical rotation regime), T_c - temperature of the less-massive (cooler) donor, $A_{\text{hs,bs}} = T_{\text{hs,bs}}/T_d$ - hot and bright spots' temperature coefficients, $\theta_{\text{hs,bs}}$ and $\lambda_{\text{hs,bs}}$ - spots' angular dimensions and longitudes (in arc degrees), θ_{rad} - angle between the line perpendicular to the local disk edge surface and the direction of the hot-spot maximum radiation, f_h - non-synchronous rotation coefficients of the gainer in critical rotation regime, $\Omega_{h,c}$ - dimensionless surface potentials of the hotter gainer and cooler donor, $\mathcal{M}_{h,c}[\mathcal{M}_\odot]$, $\mathcal{R}_{h,c}[\text{R}_\odot]$ - stellar masses and mean radii of stars in solar units, $\log g_{h,c}$ - logarithm (base 10) of the system components effective gravity, $M_{\text{bol}}^{h,c}$ - absolute stellar bolometric magnitudes, $a_{\text{orb}}[\text{R}_\odot]$, $\mathcal{R}_d[\text{R}_\odot]$, $d_e[\text{R}_\odot]$, $d_c[\text{R}_\odot]$ - orbital semi-major axis, disk radius and disk thicknesses at its edge and center, respectively, given in the solar radius units.

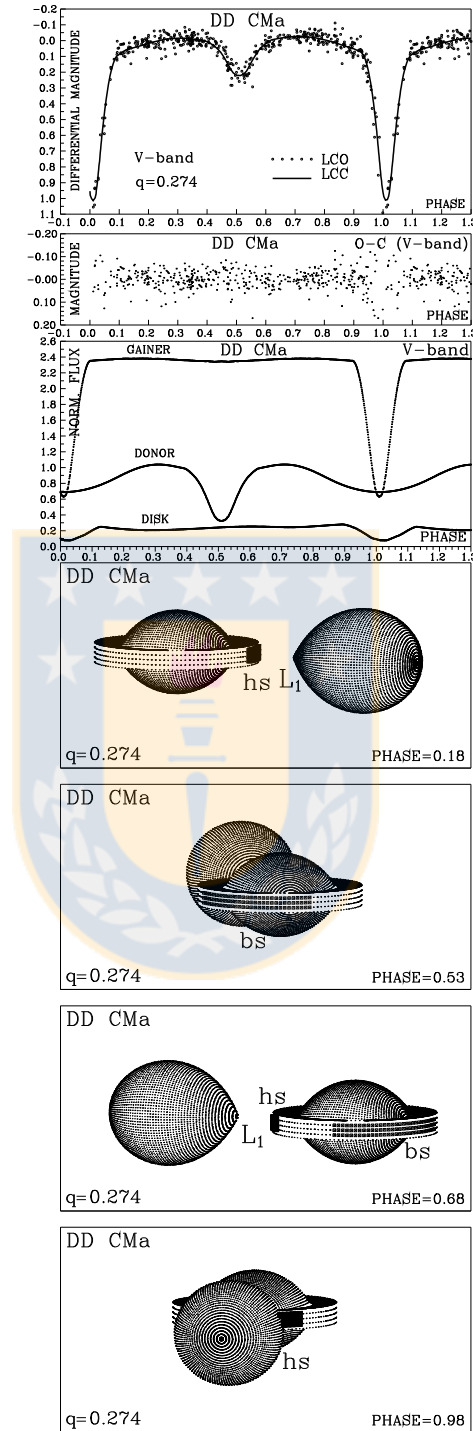


Figure 3.9: Observed (LCO), synthetic (LCC) light-curves and the final O-C residuals between the observed and synthetic light curves of the DD CMa; fluxes of donor, gainer and of the accretion disk, normalized to the donor flux at phase 0.25; the views of the model at orbital phases 0.18, 0.53, 0.68 and 0.98, obtained with parameters estimated by the light curve analysis.



Chapter 4

On the orbital and stellar parameters of the hot Algol HD 50526, its accretion disk and evolutionary stage

Rosales, J.A.¹, Mennickent, R.E.¹, Djurašević, G.^{2,3}, †Kołaczkowski, Z.⁴, Zharikov, S⁵., Araya, I.⁶, Curé, M.⁷

¹ *Departamento de Astronomía, Universidad de Concepción, Casilla 160-C, Concepción, Chile.*

² *Astronomical Observatory, Volgina 7, 11060 Belgrade 38, Serbia.*

³ *Isaac Newton Institute of Chile, Yugoslavia Branch, 11060 Belgrade, Serbia.*

⁴ *Instytut Astronomiczny Uniwersytetu Wrocławskiego, Kopernika 11, PL-51-622 Wrocław, Poland.*

⁵ *Instituto de Astronomía, Universidad Nacional Autónoma de México, Apartado Postal 877, Ensenada, Baja California, 22800 México.*

⁶ *Núcleo de Matemáticas, Física y Estadística, Facultad de Estudios Interdisciplinarios, Universidad Mayor, Chile.*

⁷ *Instituto de Física y Astronomía, Facultad de Ciencias, Universidad de Valparaíso, Chile.*

Sent to: Monthly Notices of the Royal Astronomical Society

4.1 Abstract

HD 50526 is a Double Periodic Variable characterized by a long photometric cycle of 190.584 ± 0.089 days. We have determined an improved orbital period of 6.701 ± 0.001 days using the ASAS light curve. Through high-resolution spectroscopy and using different spectrographs from years 2008 to 2015, we have determined the features of the donor star, an evolved star of $M_d = 1.05 \pm 0.02 M_\odot$ and $T_d = 9500 \pm 250$ K. We classified the donor star as of spectral type A0I, whereas for the hot companion we estimated $M_g = 5.86 \pm 0.02 M_\odot$ and $T_g = 13510 \text{ K} \pm 500 \text{ K}$ with an orbital separation of $a_{orb} = 28.5 \pm 0.02 R_\odot$, surrounded by a concave and geometrically thick luminous disc with a center thickness of $d_c = 4.5 \pm 0.02 R_\odot$, edge thickness radius of the disk $R = 14.9 \pm 0.02 R_\odot$ and a luminosity of $L_{disc} = 806 \pm 21.988 L_\odot$. The whole system is seen under inclination $62^\circ 9'$

± 0.2 at a distance $d = 1138.5 \pm 191.4$ pc. Also it present a rapidly rate variation of V/R during the orbital period, this is interpreted as evidence of material being ejected from the system. In addition, we performed with the MESA code a model for the system that suggest an age of 141.6584 Myr, which starts with an initial orbital period of 2.10 days, donor mass $M_{i,d} = 5.2 M_{\odot}$ and gainer mass $M_{i,g} = 1.8 M_{\odot}$.

4.2 Introduction

Since the discovery of the first Double Periodic Variable stars by [Mennickent et al. \(2003\)](#), in the Large Magellanic Cloud (LMC) and the Small Magellanic Cloud (SMC), we have learnt that there is a new kind of semi-detached, mass-transferring binary stars showing two closely linked photometric variations. These systems show an enigmatic long period in average 33 times longer than the orbital period ([Mennickent et al., 2016](#); [Mennickent, 2017](#); [Poleski et al., 2010](#); [Pawlak et al., 2013](#)). But an interesting and remarkable property of the DPVs is the constancy of their orbital periods, which usually do not occur in the Algols undergoing RLOF mass transfer ([Garrido et al., 2013](#)). To date, it is known that some interacting binary systems show variations of the wind generated in the stream-disc impact region ([Mennickent et al., 2016](#); [van Rensbergen et al., 2008](#)), e.g., the interacting binary V393 Scorpii studied by [Mennickent et al. \(2012\)](#) shows evidence of a cyclically variable bipolar wind. Recently, the nature of the second photometric period in this star was associated to a mechanism based on cycles of a magnetic dynamo in the donor star ([Schleicher & Mennickent, 2017](#); [Mennickent et al., 2018](#)). Also, it is believed that the changes in the DPV orbital light curves could be related to changes in disc size/temperature and spot temperature/position ([Garcés L et al., 2018](#)). Nowadays, understanding the mechanism associated to the DPV phenomenon will be of fundamental importance for the study of the mass transfer in semidetached binaries related to Algols. Also it can provide information about the stellar dynamos, stellar densities, tidal friction strength and wind processes involved in these systems which have been studied by [de Mink et al. \(2014\)](#); [Deschamps et al. \(2015\)](#).

The eclipsing interacting binary HD 50526 (ASAS ID 065402 + 0648.8, $\alpha_{2000} = 06 : 54 : 02.0$, $\delta_{2000} = 06 : 48 : 47.9$, $V=8.23 \pm 0.01$ mag, $B-V=0.08$ mag, spectral type B9)¹, is a system characterized by a long photometric cycle of 189.5 d in the ASAS² catalogue ([Pojmanski, 1997](#)) and shows a short period of 6.7007 d published in VSX³. This object requires a new detailed study, specially for the enigmatic long period. We hope to contribute to understand the associated mechanism. In Section 2 we present a detailed photometric analysis of HD 50526. In Section 3 we present a summary of spectroscopic data acquired during the years 2008 to 2015 and our methods of data reduction. In Section 4 we give the orbital parameters of the system presented in Table 4.1. We also constrain the physical parameters of the donor through a minimization of the deviation between a theoretical normalized spectrum and the observed one, presented in the Table 4.3. In Section 5 we model the light curve with a special code considering the light contribution of both components and an accretion disc. In Section 6 we perform an analysis of the reddening, distance of the system and position in the Hertzsprung-Russel diagram. Finally, the main results of our research are summarized in Section 7.

¹<http://simbad.u-strasbg.fr/simbad>

²<http://www.astrouw.edu.pl/asas/?page=acvs>

³<https://www.aavso.org/vsx/>

4.3 Photometric ephemeris

We performed a photometric analysis of the ASAS light curve considering the 269 better-quality data points labeled as A-type by ASAS (Fig. 4.1). The data set was analyzed with the Phase Dispersion Minimization algorithm (PDM-IRAF, Stellingwerf 1978)⁴, revealing an orbital period $P_o = 6.701 \pm 0.001$ d (the error was estimated by visual inspection of the periodogram and the phased light curves at trial periods) and epoch of minimum HJD = 2453414.800 ± 0.100 d. The dataset also revealed a long period $P_l = 190.584 \pm 0.889$ d with a maximum at HJD = 2453134.481 ± 0.500 d, presenting a mean magnitude of the system of $V = 8.295 \pm 0.04$ mag (Fig. 4.2), and variations from $V_{max} = 8.14$ to $V_{min} = 8.61$ mag at the visual. The distribution of the data are almost normal when compared with a random normal distribution of mean $\mu = 8.275$ and sigma $\sigma = 0.044$ (Fig. 4.1, dashed red line), but with some data a little right away of the modal distribution.

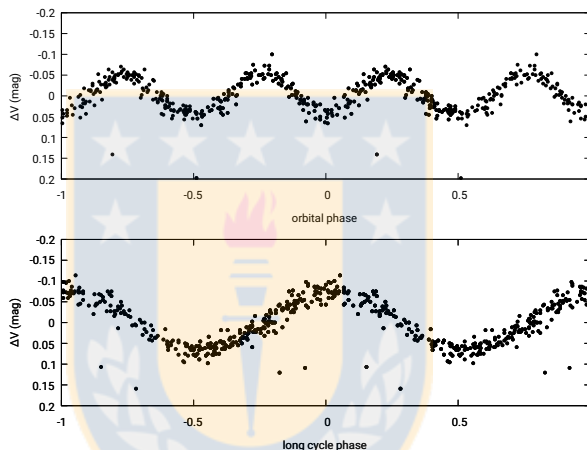


Figure 4.1: HD 50526 ASAS V-band phased light curves after disentangling. Orbital phase (up) and long period phase (down). Phases were calculated according to times of light curve minimum and maxima respectively, as given by equation (1) and (2).

Once obtained both periods, we disentangled the light curve using a code specially designed for this purpose by Zbigniew Kołaczkowski⁵. The code fits the data with a Fourier series consisting of fundamental frequencies and harmonics and removes them, the code is described by [Mennickent et al. \(2012\)](#). As result, we obtained the cleaned light curve without frequencies and two light curves for the isolated orbital and long cycles as shown in Fig. 4.1. The process reveals an orbital modulation typical of an ellipsoidal DPV (DPV/ELL) and a longer cycle characterized by a quasi-sinusoidal variability typical of Double Periodic Variables, whose full amplitude in V-band is $\sim 38\%$ the mean total brightness. We have determined the following ephemeris for the light curves and these will be used in the analysis in the rest of the paper:

$$HJD_{min,orbital} = 2453414.800(100) + 6.701(1) \times E, \quad (4.1)$$

⁴IRAF is distributed by National Optical Astronomy Observatories, which are operated by Association of Universities for Research in Astronomy, Inc., under cooperative agreement with the National Science Foundation

⁵† deceased

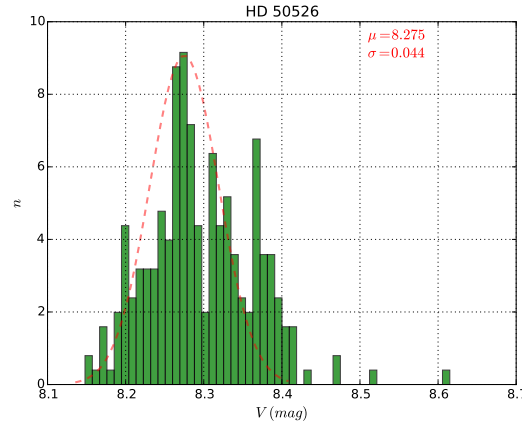


Figure 4.2: Histogram of magnitudes for HD 50526 using 50 bins for 269 ASAS A-type data. The dashed red line corresponds to normal distribution of 269 random data with mean $\mu = 8.275$ and sigma $\sigma = 0.044$.

$$HJD_{max,long} = 2453134.481(500) + 190.584(889) \times E, \quad (4.2)$$

4.4 Spectroscopic observations

We have collected a series of 140 spectra uniformly distributed on orbital phase, of high/medium spectral resolution with different spectrographs during the years 2008 and 2015. We started the year 2008 to 2009 using the CORALIE⁶ spectrograph in the ESO La Silla Observatory, and we obtained 37 spectra of signal to noise (SNR) ≈ 53 with a resolving power $R \sim 60000$ (Table 4.4). During the years 2009 to 2013 and part of the year 2015, we used the ECHELLE⁷ spectrograph in the San Pedro Mártir Observatory and we obtained 48 spectra of SNR ≈ 124 with a $R \sim 18000$ (Table 4.5). Finally, between years 2012 to 2013 we used CHIRON⁸ spectrograph in Cerro Tololo Interamerican Observatory obtaining a sample of 55 spectra of SNR ≈ 47 (slicer mode) with $R \sim 80000$ (Table 4.6). The spectral region covered were 3875-6895 Å (CORALIE), 3521-7604 Å (ECHELLE) and 4578-8782 Å (CHIRON). The correction of every spectra with flat, bias, and the wavelength calibration were done with IRAF, and we have normalized the spectra to the continuum and corrected them to the heliocentric rest frame. We have not sky subtracted and not flux calibrated our CHIRON spectra but this does not affect the strength of measurements neither the radial velocities (RVs). Our observations cover a 100% of the orbital variability, while for the long-term periodicity the coverage is $\approx 64\%$ (Fig. 4.3).

⁶<https://www.eso.org/public/chile/teles-instr/lasilla/swiss/coralie/>

⁷<http://www.astrossp.unam.mx/oanspm/>

⁸<http://www.ctio.noao.edu/noao/node/847>

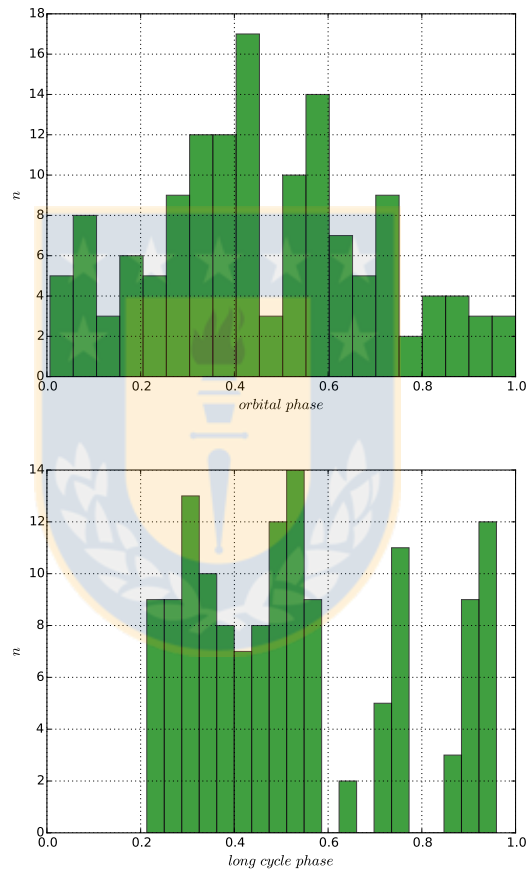


Figure 4.3: (Left) Number of spectra per bin of 0.05 for the orbital phase. (Right) Number of spectra per bin of 0.04 for the long cycle phase.

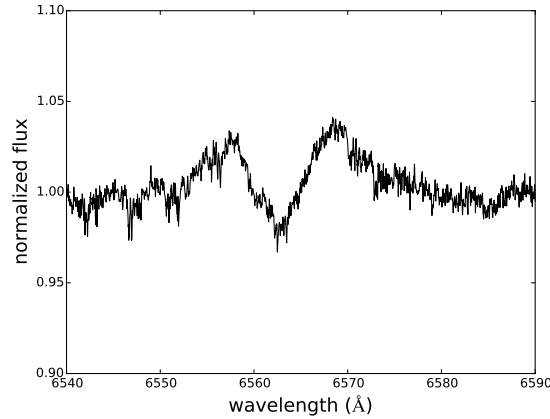


Figure 4.4: Disentangled $H\alpha$ line after applying the González & Levato method for gainer star.

4.5 Spectroscopic analysis

4.5.1 Spectral disentangling

Since chromospheric emission lines might indicate some type of activity of stellar dynamo in the donor star, according to Mennickent et al. (2012, 2018), we have selected the Mg II (4482) absorption line as a reference for the radial velocity of the cold star (Table 4.7), in addition to $H\alpha$ and $H\beta$ lines. For the case of its companion i.e. the gainer star, we selected a sample of some characteristic absorption lines (Table 4.8) that represent the movement of the hot star: HeI (4471), FeI (5887), FeI (5891), Ti (5923), FeI (5931) and FeI (5946). Particularly in this case, we used the CORALIE spectra since we have distinguished the absorption lines of each component of independent way. Later, we have disentangled the spectra obtained with the CORALIE spectrograph, using the González & Levato (2006) method that is quite good for separating the absorption-lines widths of stellar components. As we can observe in Fig. 4.4 the double emission in $H\alpha$ confirms the presence of a circumstellar accretion disc and the spectra suggest that the system is a semi detached binary experiencing a mass transfer event.

4.5.2 Determination of donor physical parameters

The determination of physical parameters of the donor is of fundamental importance to constrain the size of the system. We have constructed a grid of synthetic spectra, modeling stellar atmospheres with the SPECTRUM⁹ code and using a grid of model atmospheres given by ATLAS9¹⁰ (Castelli & Kurucz, 2004).

The grid was constructed in Local Thermodynamic Equilibrium (LTE) with effective temperatures from 3500 to 19000 K in steps of 250 K, the surface gravities run from 0.0 to 5.0 dex with steps of 0.5 dex, the micro-turbulent velocity from 0.0 to 2.0 km s⁻¹ with steps of 1 km s⁻¹, the macro-turbulences velocity from 0 to 10 km s⁻¹ with steps of 0.001 km s⁻¹, $v \sin i$ from 30 to 70 km s⁻¹ with steps of 0.5 km s⁻¹, veiling factor from 0.4 to 0.5 with steps of 0.1, and finally a fixed

⁹<http://www.appstate.edu/~grayro/spectrum/spectrum.html>

¹⁰<http://wwwuser.oats.inaf.it/castelli/grids.html>

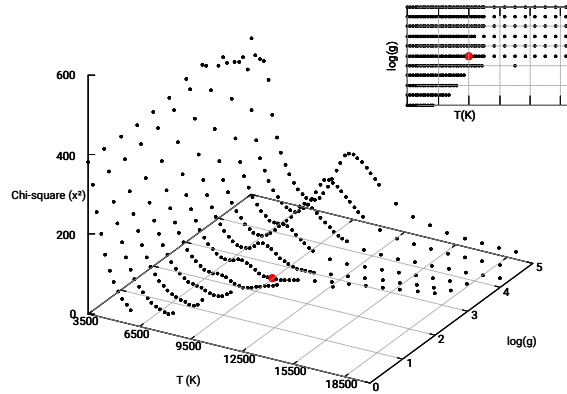


Figure 4.5: Chi-square analysis to find the best theoretical normalized spectrum with respect to the observed spectrum. The dots mesh of χ^2 was computed with three freedom degrees and with all parameters at their optimized values for donor star, presenting a minimum value in $\Delta\chi^2 = 1.642$ from a total of 20012 data.

mixing length parameter $l/H=1.25$ for default from the grid. The analysis implemented is based on a chi-square optimization algorithm, and consists in the minimization of the deviation between the theoretical normalized spectrum and the observed spectrum of the donor star previously disentangled and corrected by veiling factor $\eta = 0.44 \pm 0.01$ due to the contribution of the gainer, this is a factor of constant proportionality between the theoretical spectrum and the observed, that allowed us the determination of various physical parameters of the donor star. The implemented method yielded a chi-square minimum at at $T_2 = 9500 \pm 250$ K, $\log g_2 = 2.5 \pm 0.5$ dex, $v_{mic} = 0.0 \pm 1.0$ km s⁻¹, $v_{mac} = 0.045 \pm 0.045$ km s⁻¹, $v \sin i = 60.5 \pm 0.5$ km s⁻¹, $l/H=1.25$ (Fig. 4.5), the best theoretical model is compared with the observed spectrum in Fig. 4.6.

For better constrain the parameters of the donor star and classify it, we have compared our best synthetic spectral model with the spectrum of the star HD 47306 (Fig. 4.7) offered by the UVES-POP ESO¹¹ and classified as A0II by Houk (1978). This suggests that the donor star is similar to an early evolved A-type star.

4.5.3 Radial velocities for the donor

As we said at the Section 4, we selected some characteristic lines that represent the movement of both components, hot and cold star. The radial velocity of the donor was obtained by Gaussian fit method on a set of metallic lines MgI 4482 from spectra obtained with the CORALIE spectrograph. The velocities were corrected to the absolute heliocentric system. The orbital parameters for HD 50526 were obtained, using the genetic algorithm PIKAIA¹² of public domain developed by Charbonneau (1995) and written in Fortran-77. The code produce a series of theoretical velocities and find the best parameters through the minimization of the function χ^2 , defined as:

¹¹<http://www.eso.org/sci/observing/tools/uvespop.html>

¹²<http://www.hao.ucar.edu/modeling/pikaia/pikaia.php>

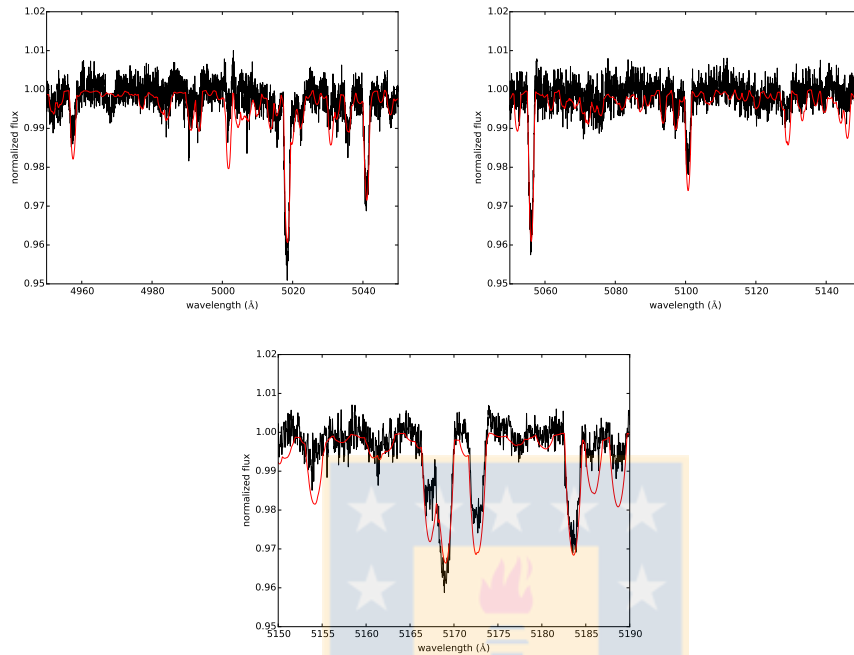


Figure 4.6: Synthetic spectrum model (red line) has been veiled according to factor $\eta = 0.44$ and over plotted on donor spectrum previously disentangled (black line).

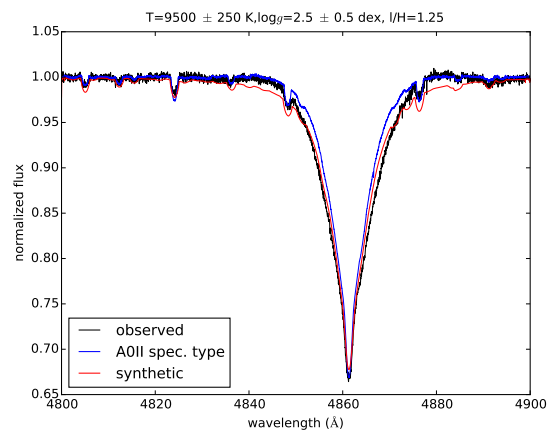


Figure 4.7: A detailed comparison of $H\beta$ between the observed (black line), synthetic (red line) spectrum and a A0II spectral type star from UVES-POP (Blue line).

$$\begin{aligned} \chi^2(P_o, \tau, \omega, e, K_2, \gamma) \\ = \frac{1}{N-6} \sum_{j=1}^N \left(\frac{V_j^{obs} - V(t_j; P_o, \tau, \omega, e, K_2, \gamma)}{\sigma_j} \right)^2, \end{aligned} \quad (4.3)$$

where the parameter N represents the number of observations, V_j^{obs} is the radial velocity observed in the data set and $V(t_j; P_o, w, e, K_2, \gamma)$ is the radial velocity at the time t_j . P_o is the orbital period, τ the time of passage per the periastron, w the periastron longitude, e the orbital eccentricity, K_2 the half-amplitude of the radial velocities for the donor, and finally γ the velocity of the center of mass of the system. Through the equation 2.45 given by [Hilditch \(2001\)](#) the theoretical radial velocity is given by :

$$V(t) = \gamma + K_2(\cos(\omega + \theta(t)) + e\cos(\omega)), \quad (4.4)$$

where the angular parameter called true anomaly θ is obtained solving the following two equations involving the angular parameter eccentric anomaly E given by the equation 2.35 of [Hilditch \(2001\)](#) as :

$$\tan\left(\frac{\theta}{2}\right) = \sqrt{\frac{1+e}{1-e}} \tan\left(\frac{E}{2}\right), \quad (4.5)$$

$$E - e\sin(E) = \frac{2\pi}{P_o}(t - \tau), \quad (4.6)$$

First, we have solved the equation (6) for eccentric anomaly E , later the equation related to the true anomaly θ (5) and finally the equation for the theoretical radial velocity (4) $V(t_j; P_o, w, e, K_2, \gamma)$ and through a Monte Carlo simulation we have estimated the error, perturbing the best fitting solution obtained with PIKAIA code and computing a χ^2 for these perturbed solutions. As criterion for deciding when to reject an elliptical ($p < 0.05$) or circular orbit ($p \geq 0.05$), we have implemented the statistical test p_1 of [Lucy & Sweeney \(1971\)](#) :

$$p_1 = \left(\frac{\sum(o-c)_{ecc}^2}{\sum(o-c)_{circ}^2} \right)^{(n-m)/2} \quad (4.7)$$

the subindex *ecc* correspond to the χ^2 obtained from the fitting of an elliptical orbit, while *circ* is the χ^2 from a circular orbit, n is the total number of observational radial velocities and m is the number of free parameters for the fitting of an elliptical orbit. Finally, we obtained orbital parameters with respective errors and are given in Table 4.1 with a p value of 0.00506 compatible with a small elliptical orbit. However, we analyzed the solution around 1σ and 2σ of error, and a circular orbit is not allowed for the system as indicated (Fig. 4.8).

The radial velocities measured for the donor and gainer star were selected from the group of lines mentioned in Section 4.1. These lines were measured through Gaussian fits and show a little

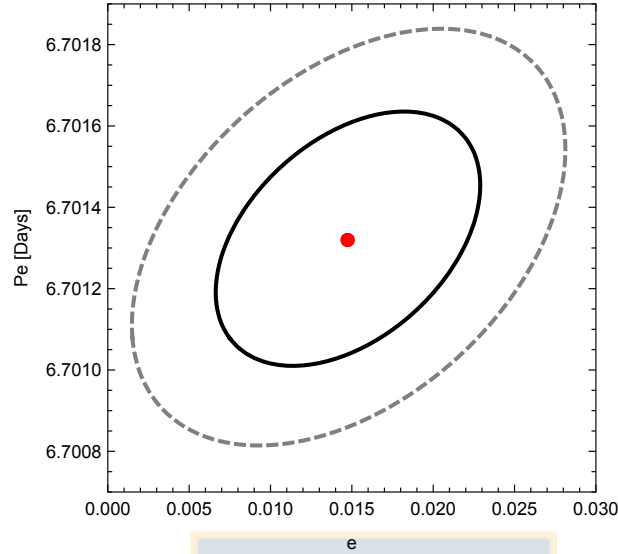


Figure 4.8: Orbital period as function of the eccentricity calculated by Monte Carlo simulations. Solid black line correspond to 1σ , dashed gray line to 2σ and the red dot to the minimum χ^2 .

scatter for the primary component (gainer). The radial velocities (RV) of the gainer star for He I 4471 was fitted with a sine function of amplitude $29.082 \pm 2.232 \text{ km s}^{-1}$ and zero point $0.000 \pm 1.749 \text{ km s}^{-1}$. The RV of the donor measured with the Mg I 4482 line, was fitted with an amplitude of $162.483 \pm 0.648 \text{ km s}^{-1}$ and a zero point $0.000 \pm 0.541 \text{ km s}^{-1}$. Both solutions assume a circular orbit (Fig. 4.9).

4.5.4 Temperature indicators: He I 4471 and Mg II 4482

An useful way of estimating the temperature of a B-type star, is considering the equivalent width (EW) and EW ratios of some absorption lines. We performed a synthetic model of EW as a

Table 4.1: Orbital elements for the donor of HD 50526 obtained through minimization of χ^2 given by equation (1). The value $\tau^* = \tau - 2450000$ is given and the maximum and minimum are one isophote 1σ .

Parameter	Best value	Low limit	Upper limit
$P_o(d)$	6.7013	6.7009	6.7017
τ^*	567.4830	567.4720	567.4960
e	0.0147	0.0070	0.0225
$\omega(rad)$	1.6265	1.6160	1.6380
$K_2(kms^{-1})$	163.2830	162.1180	164.4180
$\gamma(kms^{-1})$	0.2342	-0.6054	1.0945

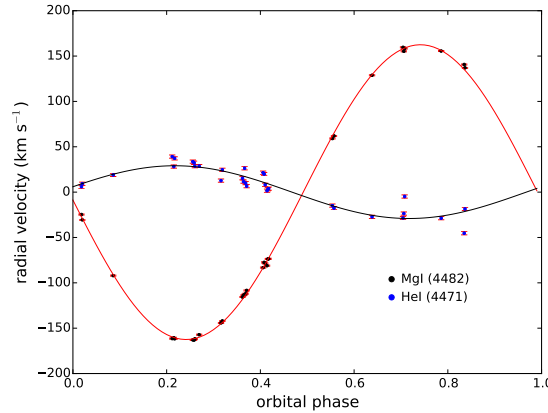


Figure 4.9: Radial velocities of MgI 4482 (donor) and HeI 4471 (gainer) measured by Gaussian fits. The best fits are shown for both orbits.

function of the effective temperature for He I 4471 and Mg II 4482 absorption lines. The models were calculated for effective temperatures from 10000 to 25000 K with steps of 1000 K, surfaces gravities from 3.0 to 4.0 dex with steps of 0.5 dex. The fixed parameters used were micro-turbulence velocity $v_{mic} = 2.0 \text{ km s}^{-1}$, macro-turbulence $v_{mac} = 10 \text{ km s}^{-1}$ and solar metallicity $z = 0.02$. The theoretical models available for a B star reaches a maximum EW around 18000 K for $\log g = 3.0$ dex, while that for surface gravities 3.5 and 4.0 dex is to 19000 K (Fig. 4.10, left).

In order to consider this method as a good temperature indicator of the hot star, first we have fitted a 4rd order polynomial to the mean equivalent width and incorporated a confidence interval of 95% around the mean to analyze the behavior of absorption lines He I 4471 and the He I(4471)/Mg I (4482) ratio without disentangling. The obtained values from the spectrographs CORALIE and ECHELLE were represented by black and red markers respectively, covering a the complete orbital phase. Of this way, is expected that the obtained values from disentangled spectra are above the mean or outside the confidence zone. Thus we can corroborate that the disentangled was an optimal process.

We calculated the EW_{4471} from the disentangled spectra of the gainer star and using green markers around the orbital phase $\phi_o = 0.75$, were compared these results with the previous values, i.e. with the non-disentangled. Wherein the mean equivalent width $EW_{4471} = 0.588 \pm 0.153$ obtained with CORALIE and ECHELLE for different epochs around $\phi_o = 0.75$, corresponds to an interval of temperature between 12000 to 14000 K as a first approximation (Fig. 4.10, right). In addition, we noted a slight difference between the values measured for the equivalent width EW_{4471} an the equivalent width ratio $EW_{4471/4482}$, obtained by CORALIE AND ECHELLE spectrographs (Fig. 4.10). This small difference is caused because the ECHELLE spectrograph has around 1/3 of the spectral resolution capability of the CORALIE spectrograph. In addition, we noted a slight difference between the values measured for the equivalent width EW_{4471} an the equivalent width ratio $EW_{4471/4482}$, obtained by CORALIE AND ECHELLE spectrographs (Fig. 4.10). This small difference is caused because the ECHELLE spectrograph has around 1/3 of the spectral resolution capability of the CORALIE spectrograph. Thus, at the moment of resolving the absorption lines of the spectra some neighboring lines could be considered causing a slightly extra value.

Later, to gain confidence of the used method we computed the $EW_{4471/4482}$ ratio around the orbital phase $\phi_o = 0.75$ of the disentangled spectra and were represented by the green markers

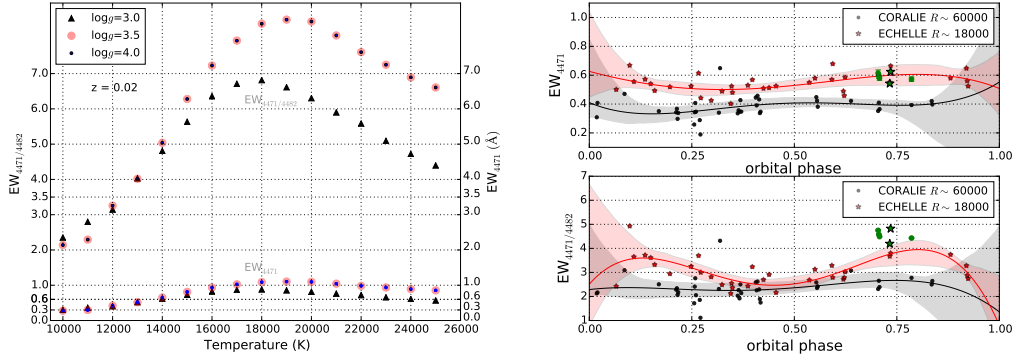


Figure 4.10: (Left) Theoretical Equivalent widths of He I 4471 and EW ratio of between He I 4471 and Mg I 4482 lines as a function of the effective temperature for $z=0.02$, $v_{\text{ sini}}= 150 \text{ km s}^{-1}$, $v_{\text{ mic.}}=2.0 \text{ km s}^{-1}$, $v_{\text{ mac.}}=10 \text{ km s}^{-1}$. (Right) Observed EW_{4471} and $EW_{4471/4482}$ versus orbital phases for CORALIE and ECHELLE data of the gainer star. The continuum line is a fitted 4rd order polynomial to the mean EW with a confidence interval region of 95% of the mean EW, the green symbols at $\phi_o = 0.75$ corresponds to the equivalent width disentangled.

again, and we compared these to the non-disentangling values (black/red markers). We obtained a mean ratio of $EW_{4471/4482} = 4.544 \pm 0.378$. Therefore, the model suggests that the gainer star has a temperature of $T_g = 13500 \pm 500 \text{ K}$, $v_{\text{ sini}}= 150 \text{ km s}^{-1}$, $v_{\text{ mic.}} = 2.0 \text{ km s}^{-1}$, $v_{\text{ mac.}} = 10 \text{ km s}^{-1}$ and metallicity $z = 0.02$. We must emphasize that the disentangling of the gainer and disc contribution was not possible to perform it, since there are not available models for disc spectral lines, causing that the error estimations might be larger.

4.5.5 The $H\alpha$ emission line profile

We analyzed the $H\alpha$ profile disentangled of the donor contribution for several orbital phases and long cycle epochs. The system HD 50526 shows $H\alpha$ irregular double emission at all phases (Fig. 4.11), which can be interpreted as a disc seen at low inclination, with an equivalent width which vary between ~ 0.0 to 0.7 \AA (Fig. 4.12). The ratio between violet and red emission known as the V/R parameter, defined as $V/R = (I_v - 1)/(I_r - 1)$, tends to vary during the orbital period, showing a minimum around $\phi_o = 0.315$ and a maximum around $\phi_o = 0.732$ for the orbital phase, which is not related to the movement of the system, due that during quadratures 0.25 and 0.75 occurs the maximums and could be interpreted as the projection of an outflow in the sight of the observer, when it is seen and hidden by the system (Fig. 4.13).

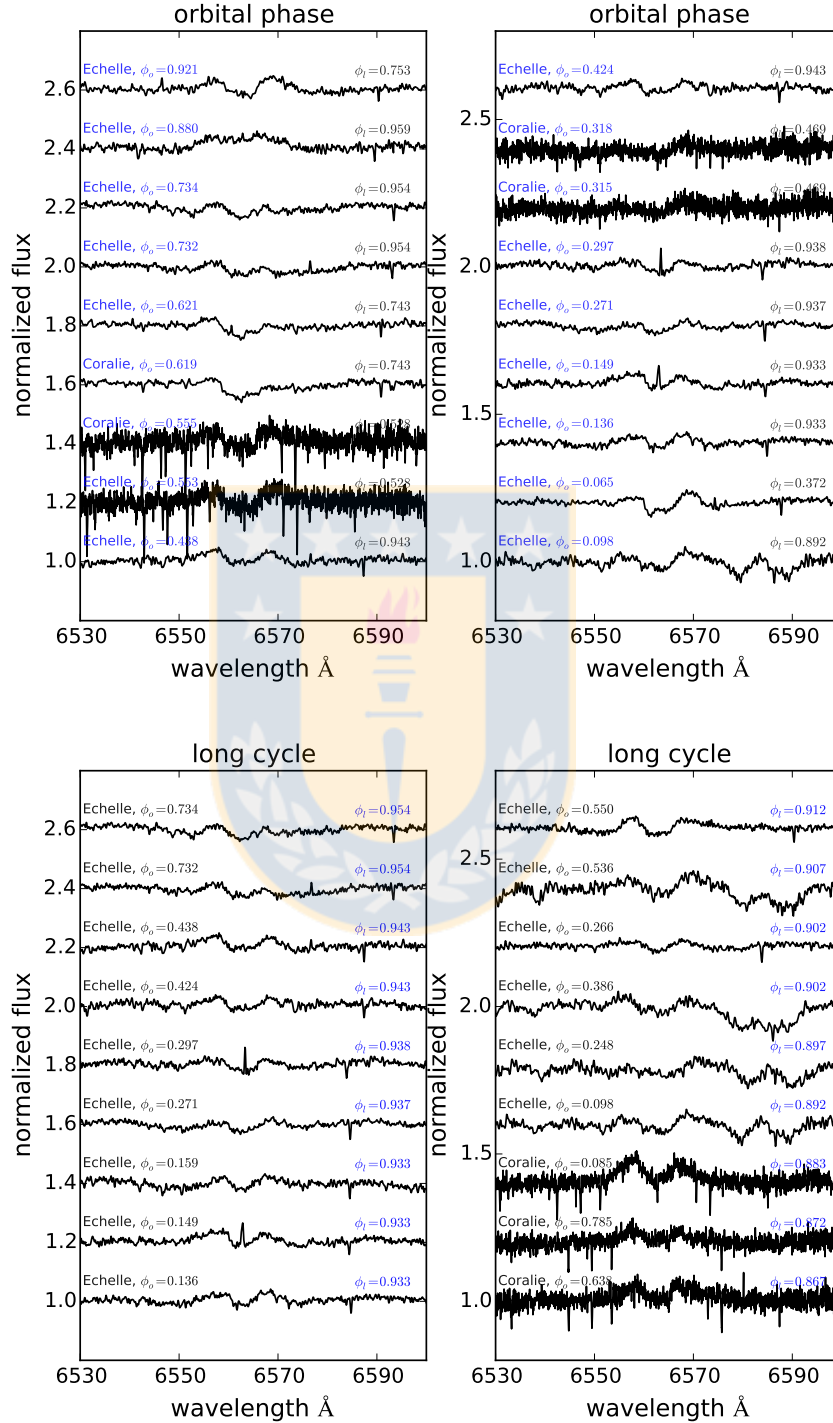


Figure 4.11: (Top) From left to right, comparison of H α spectra during a complete orbital phase (donor subtracted) for the gainer star. (Bottom) left to right, analysis of H α spectra close to the maximum of the long cycle (donor subtracted). The orbital and long cycle phases were labeled to left and right of every spectra.

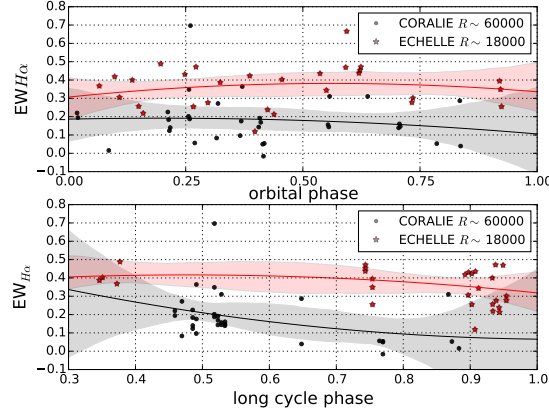


Figure 4.12: Equivalent width of $H\alpha$ profile from gainer star for several orbital (Top) and long cycle epochs (Bottom) with donor subtracted, using Coralie and Echelle spectrographs. The continuum line is a fitted 4rd order polynomial to the mean EW with a confidence interval region of 95%.

4.5.6 Gainer, mass ratio and circumstellar matter

In Section 4.3, we computed a mass ratio $q = 0.179 \pm 0.014$ for the system. But due to the scattering observed in RV for the gainer star, the possible blending of some lines due to absorbing/emitting material of the disc, and for completeness of the analysis, we have made a brief study of the compatibility of a synchronously rotating secondary star filling the Roche lobe for the mass ratio previously estimated. We have used a composite equation between the equations 3.5 and 3.9 from Eggleton (2006) valid for systems in synchronization:

$$\frac{v_{rot} \sin i}{K} \approx (1 + q) \frac{0.49q^{2/3}}{0.6q^{2/3} + \ln(1 + q^{1/3})}, \quad (4.8)$$

for a semi amplitude $K_2 = 162.483 \text{ km s}^{-1}$ and $v_{rot} \sin i = 60.5 \text{ km s}^{-1}$, we obtain a mass ratio $q \approx 0.312 \pm 0.015$. This figure is around 1.7 times the obtained value from the RV analysis from Section 4.6. Probably this difference can be interpreted as non-synchronism but too suggests that the gainer may be surrounded by a gas stream and a disk that distorts the spectrum and therefore the contamination affects the mass ratio derived from the radial velocities half-amplitudes.

For this reason we have computed the ratio between the effective radius and the orbital separation $R_L/a = 0.244 \pm 0.155$ using a mass ratio of 0.179. The result is according to the numerical integration Table 3.1 shown by Eggleton (2006) for binary interactions with conservative processes. Also, we have quantified the relation between the mean density $\bar{\rho}$ (g cm^{-3}) of the star and the critical orbital period (days) for a system, using the following equation:

$$P_{cr} \sqrt{\bar{\rho}} = \left(\frac{3\pi}{G} \right)^{1/2} \left(\frac{q}{1+q} \right)^{1/2} x_L^{-3/2}, \quad (4.9)$$

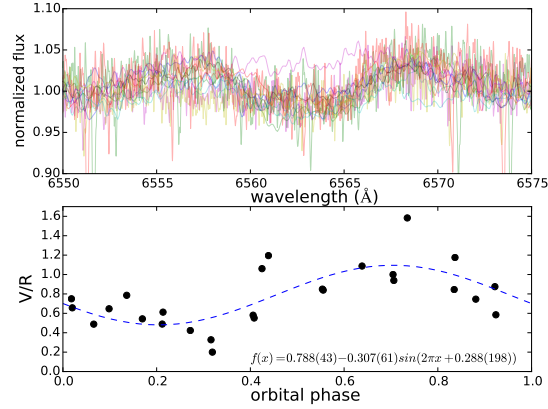


Figure 4.13: (Top) Comparison of normalized fluxes centered in the H α profiles during a complete orbital phase of the gainer star, (Bottom) Violet and Red intensities (V/R) ratio of H α profile, measured from the continuum of the gainer star.

where $x_L = R_L/a$ is in units of the orbital separation. Thus, for the derived ratio between the effective Roche Lobe and orbital separation R_L/a , we computed the value for the critical orbital period as a function of mean density $P_{cr}\sqrt{\rho} = 0.444 \pm 0.071$, and this value is higher than the published in the Table 3.1 by Eggleton (2006). The result suggests that the donor star still exceeds its Roche lobe. Hence, for better constrain the donor star. We used the logarithmic derivate of the Roche lobe radius, as an important factor to consider since corresponds to the equivalent of the ratio between star's radius and the mass as determined by its internal structure. The response of the donor's Roche lobe radius to the mass transfer depends on the mass ratio and the accretion efficiency $0 \leq \beta \leq 1$ ($\beta = 1$ conservative, $\beta = 0$ non-conservative), and we used the following dimensionless equation:

$$R'_L \equiv \frac{\partial \ln R_L/a}{\partial \ln m_d} = \frac{\partial \ln a}{\partial \ln m_d} + \frac{\partial \ln R_L/a}{\partial \ln q} \frac{\partial \ln q}{\partial \ln m_d}, \quad (4.10)$$

The dimensionless eq. 10 comes from the approximation for the Roche lobe radius of using the equation 3.17 of Eggleton (2006) and the equation 9 of Woods et al. (2012). We must emphasize that after the mass transfer onset the stability depends on the response of the radius of the donor star and the response of the Roche lobe radius to the mass loss of the donor. Therefore, we computed the logarithmic derivate assuming a maximum accretion efficiency $\beta_{max} = 1.0$ and we obtained for the donor star $R'_L = -1.313 \pm 0.001$, this suggests a binary interaction within of a conservative processes as show numerical integration Table 3.1 by Eggleton (2006).

4.5.7 Mass constrains from spectroscopy

To determine the masses of each component in a binary spectroscopic system with high accuracy is not easy, first we must to know the velocity semi amplitude of both components. This allows through the use of the mass function determine the masses of stars with an uncertainties less than to 3%. The mass function is defined as a function that represents the minimum possible mass for the unseen star, for a system with unknown orbital inclination and elliptical orbit (Hilditch (2001), eq. 2.53), and is expressed as :

$$f = 1.0361 \times 10^{-7} (1 - e^2)^{3/2} \left(\frac{K_2}{\text{kms}^{-1}} \right)^3 \frac{P_o}{\text{days}} M_{\odot}, \quad (4.11)$$

where e is the eccentricity and K_2 the half-amplitude of the RV of the donor star. Hence for an eccentricity $e = 0.0147 \pm 0.004$, we obtained a mass function for the donor $f = 2.978 \pm 0.001 M_{\odot}$. Using the following approximation :

$$M_d \sim 1.25q(1 + q)^2 f, \quad (4.12)$$

$$M_g \sim 1.25(1 + q)^2 f, \quad (4.13)$$

(Eggleton (2006), eq. 1.3a, 1.3b), we estimated the mass of donor star around $0.926 M_{\odot}$ while that the gainer mass is $5.174 M_{\odot}$. Therefore this estimation suggests that the orbital inclination is around $\sim 68^\circ$, which we will discuss in the next section.

4.6 Light-curve model and system parameters

4.6.1 The fitting procedure

Previously, we have used different methods to obtain some parameters of the system HD50526 by independent ways, through the photometric and spectroscopic analysis. In this section we have implemented the use of an algorithm developed by Djurašević (1992, 1996) which allow us to obtain the fundamental parameters through a fitting of the V-band light curve with a theoretical light-curve calculation. The code works with the aid of an inverse-problem solving method and using the parameters computed previously.

We assumed a semi detached binary system with a donor filling the Roche lobe with a conservative processes of mass transfer and adopted a configuration that included and optical thick accretion disc around the gainer star. Also the model considers a hot spot located on the edge side of the disc and the gainer in a synchronous rotation regime. We fixed the mass ratio $q = 0.179$, the temperature of the cool and less massive star in $T_c = 9500$ K with a filling factor for the critical Roche lobe of the donor in $F_c = 1.0$ and using a non-synchronous rotation coefficients of the system components $f_{h,c}=1.0$. In addition we set the gravity darkening exponent of the gainer $\beta_h = 0.25$ and albedo coefficient $A_h = 1.0$, while for the donor a $\beta_c = 0.25$ and $A_c = 1.0$.

Table 4.2: Results of the analysis of DPV HD 50526 V-filter light curve obtained by solving the inverse problem for the Roche model with an accretion disk around the more massive (hotter) gainer in synchronous rotation regime.

Quantity		Quantity	
n	265	$\mathcal{M}_h [\mathcal{M}_\odot]$	5.86 ± 0.02
$\Sigma(\text{O} - \text{C})^2$	0.0580	$\mathcal{M}_c [\mathcal{M}_\odot]$	1.05 ± 0.02
σ_{rms}	0.0148	$\mathcal{R}_h [\text{R}_\odot]$	3.54 ± 0.03
$i [^\circ]$	62.9 ± 0.2	$\mathcal{R}_c [\text{R}_\odot]$	6.92 ± 0.01
F_d	0.97 ± 0.2	$\log g_h$	4.11 ± 0.02
$T_d [\text{K}]$	9260 ± 200	$\log g_c$	2.78 ± 0.02
$d_e [a_{\text{orb}}]$	0.157 ± 0.01	M_{bol}^h	-1.65 ± 0.16
$d_c [a_{\text{orb}}]$	0.098 ± 0.02	M_{bol}^c	-1.57 ± 0.02
a_T	4.3 ± 0.3	$a_{\text{orb}} [\text{R}_\odot]$	28.5 ± 0.02
f_h	1.00	$\mathcal{R}_d [\text{R}_\odot]$	14.9 ± 0.02
F_h	0.251 ± 0.01	$d_e [\text{R}_\odot]$	4.5 ± 0.02
$T_h [\text{K}]$	13510 ± 500	$d_c [\text{R}_\odot]$	2.8 ± 0.03
$A_{\text{hs}} = T_{\text{hs}}/T_d$	1.40 ± 0.02		
$\theta_{\text{hs}} [^\circ]$	20.3 ± 2.0		
$\lambda_{\text{hs}} [^\circ]$	328.2 ± 4.0		
$\theta_{\text{rad}} [^\circ]$	-1.4 ± 3.0		
$A_{\text{bs}} = T_{\text{bs}}/T_d$	1.18 ± 0.02		
$\theta_{\text{bs}} [^\circ]$	52.1 ± 2.0		
$\lambda_{\text{bs}} [^\circ]$	143.1 ± 2.0		
Ω_h	8.235 ± 0.09		
Ω_c	2.180		

FIXED PARAMETERS: $q = \mathcal{M}_c/\mathcal{M}_h = 0.179$ - mass ratio of the components, $T_c = 9500\text{K}$ - temperature of the less-massive (cooler) donor, $F_c = 1.0$ - filling factor for the critical Roche lobe of the donor, $f_{h,c} = 1.00$ - non-synchronous rotation coefficients of the system components, $\beta_h = 0.25$, $\beta_c = 0.25$ - gravity-darkening coefficients of the components, $A_h = 1.0$, $A_c = 1.0$ - albedo coefficients of the components.

Note: n - number of observations, $\Sigma(\text{O} - \text{C})^2$ - final sum of squares of residuals between observed (LCO) and synthetic (LCC) light-curves, σ_{rms} - root-mean-square of the residuals, i - orbit inclination (in arc degrees), $F_d = R_d/R_{yc}$ - disk dimension factor (the ratio of the disk radius to the critical Roche lobe radius along y-axis), T_d - disk-edge temperature, d_e , d_c , - disk thicknesses (at the edge and at the center of the disk, respectively) in the units of the distance between the components, a_T - disk temperature distribution coefficient, f_h - non-synchronous rotation coefficient of the more massive gainer (in the synchronous rotation regime), $F_h = R_h/R_{zc}$ - filling factor for the critical Roche lobe of the hotter, more-massive gainer (ratio of the stellar polar radius to the critical Roche lobe radius along z-axis for a star in synchronous rotation regime), T_h - temperature of the gainer, $A_{\text{hs}} = T_{\text{hs}}/T_d$ - hot spot temperature coefficient, θ_{hs} and λ_{hs} - spot angular dimension and longitude (in arc degrees), θ_{rad} - angle between the line perpendicular to the local disk edge surface and the direction of the hot-spot maximum radiation, $A_{\text{bs}} = T_{\text{bs}}/T_d$ - bright spot temperature coefficient, θ_{bs} and λ_{bs} - bright spot angular dimension and longitude (in arc degrees), $\Omega_{h,c}$ - dimensionless surface potentials of the hotter gainer and cooler donor, $\mathcal{M}_{h,c} [\mathcal{M}_\odot]$, $\mathcal{R}_{h,c} [\text{R}_\odot]$ - stellar masses and mean radii of stars in solar units, $\log g_{h,c}$ - logarithm (base 10) of the system components effective gravity, $M_{\text{bol}}^{h,c}$ - absolute stellar bolometric magnitudes, $a_{\text{orb}} [\text{R}_\odot]$, $\mathcal{R}_d [\text{R}_\odot]$, $d_e [\text{R}_\odot]$, $d_c [\text{R}_\odot]$ - orbital semi-major axis, disk radius and disk thicknesses at its edge and center, respectively, given in solar units.

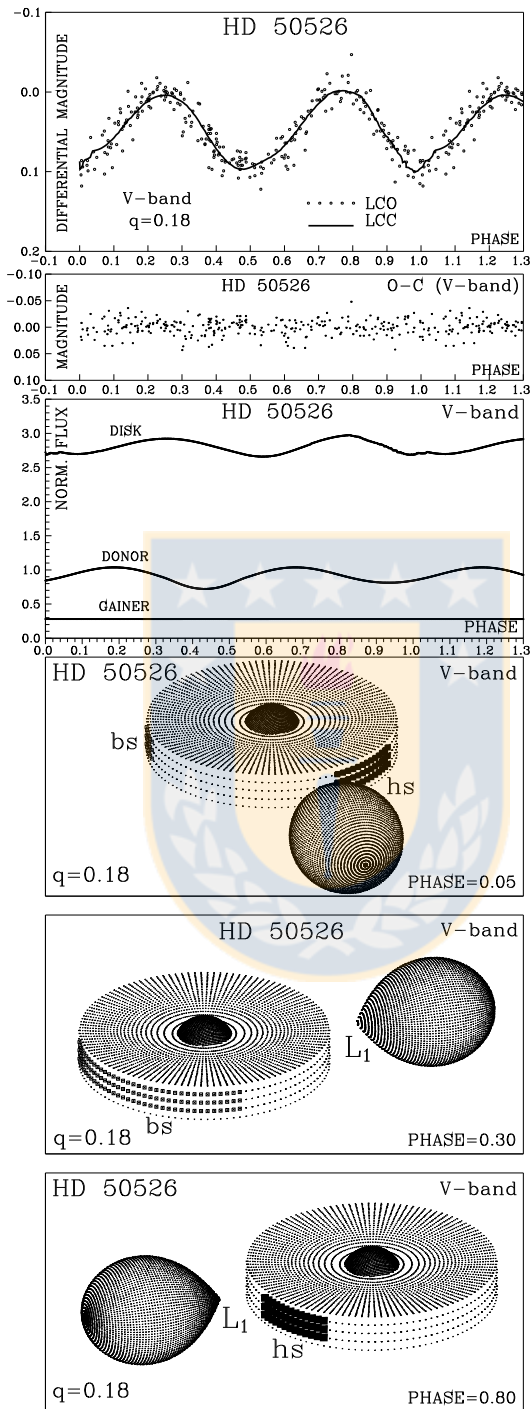


Figure 4.14: Observed (LCO) and synthetic (LCC) light-curves of DPV HD50526 obtained by analyzing photometric observations; final O-C residuals between the observed and synthetic light curves; fluxes of the donor, gainer and of the accretion disk, normalized to the donor flux at phase 0.25; the views of the model at orbital phases 0.05, 0.30 and 0.80, obtained with parameters estimated by the light curve analysis.

4.6.2 The best light-curve model

We employed the code described in the previous section, computing the individual flux contribution of the disc, donor and gainer star for HD50526 during a complete orbital cycle. Through an analysis of the photometric observations, we have performed a fit between the synthetic (LCC) light curve on the observed light curve (LCO) (Fig. 4.14) and we noted that residuals (O-C) for the best fit, do not present dependences on the orbital or long cycle phases and shown an acceptable scatter of ± 0.05 mag.

The obtained results for this system using a gainer in synchronous rotation regime are presented in Table 4.3. The best model shows an orbital inclination $i = 62.9 \pm 0.2$ degree. Also the model contains an accretion disc, concave and optically thick around the hot star with a radius of $R_d = 14.9 \pm 0.02 R_\odot$, which is 4.2 times larger than the star in their center ($R_h = 3.54 \pm 0.03 R_\odot$), with a central thickness $d_c = 2.8 \pm 0.03 R_\odot$ and an edge thickness $d_e = 4.5 \pm 0.02 R_\odot$. We noted that the gainer star is hidden by the disc around $\sim 32\%$ and it is partly illuminated from inside, their temperature in the external border is highly elevated $T_d = 9260 \pm 200$ K and comparable with the gainer, it also presents a luminous hot spot on the edge of the disc with a temperature of $T_{hs} = 12964 \pm 335$ K and a bright spot $T_{bs} = 10926 \pm 300$ K placed in an opposite disk's location. Due to the great flux contribution from the disk we assume that the disc is optically thick, and the luminosity L_{disc} is in form of black body radiation, then the temperature of the disc is related to the viscous dissipation $2\sigma T_d^4 = D(R)$, and we could express the mass transfer as :

$$\dot{M} = \frac{16\pi R_d^3}{3GM} \sigma T_d^4 \left[1 - \left(\frac{R_\star}{R_d} \right)^{1/2} \right]^{-1}, \quad (4.14)$$

(Frank et al. (2002), eq. 5.20), where σ is the Stefan-Boltzmann constant, R_d the radius disc, T_d temperature of the disc and R_\star is the radius of the accretor star. We have computed the mass transfer $\dot{M} = 3.100 \times 10^{-7} \pm 3.140 \times 10^{-9} M_\odot \text{ yr}^{-1}$, and the result is in agreement with the proposed by Bisikalo et al. (2003) for accretion discs of semi detached systems and values obtained for some DPV by (Garrido et al., 2013; Mennickent, 2014; Barría et al., 2014). In addition, we computed the total luminosity of the disc with a viscous dissipation rate $D(R)$:

$$L_{acc} = 2 \int_{R_1}^{R_2} D(R) 2\pi R dR, \quad (4.15)$$

$$D(R) = \frac{3GM\dot{M}}{8\pi R^3} \left[1 - \left(\frac{R_\star}{R} \right)^{1/2} \right], \quad (4.16)$$

Due that matter at R_\star still retains as kinetic energy the half of the potential energy lost in spiraling in, the half L_{acc} still available to be radiated from the boundary layer itself, i.e. the disc luminosity is half of the total accretion luminosity and the other half of the luminosity is emitted when the gas makes the transition from the inner edge of the accretion disc to the surface of the accretor star (gainer). Hence, we computed the luminosity of the disc $L_d = 3.085 \times 10^{29} \pm 8.415 \times 10^{27} \text{ J s}^{-1} = 806.000 \pm 21.988 L_\odot$ using the equation eq. 5.22 of Frank et al. (2002). This is understood as an luminous hot disc, which is heated and illuminated from the inside by its accretor and the rate of energy gained by the accretion of matter of using the dimensionless equation is

$$\eta_{acc} = L_{acc}/(\dot{M}c^2) = 3.513 \times 10^{-6} \pm 3.209 \times 10^{-8}, \text{ (Frank et al., 2002).}$$

4.7 Reddening, distance and spectral energy distribution

4.7.1 Distance determination

In this section we determinate the distance of a binary system using a classical method proposed by Clausen (2004). The method to determine the distance is based on the distance modulus of both binary components observed in V band, through the following equation:

$$\begin{aligned} (m_{d,g} - M_{d,g})_0 &= 5\log(R_{d,g}/R_{\odot}) + (m_{d,g} - A_V) \\ &\quad - M_{bol\odot} + 10\log(T_{d,g}/T_{\odot}) \\ &\quad + BC_{d,g} \end{aligned} \quad (4.17)$$

where the subindex d, g correspond to the donor and gainer star, A_V the interstellar absorption, $M_{bol\odot}$ the bolometric magnitude of the sun and $BC_{g,d}$ bolometric corrections for each component. The color excess for HD50526 was determined using a dust map from IRSA¹³ with an image size of 2.0 deg. We used $E(B - V)_{SF} = 0.275 \pm 0.016$ (Schlafly & Finkbeiner, 2011) which corresponds to the reddening in the direction of the target. We assumed the visual extinction to reddening ratio $A_V/E(B - V) = 3.1$ constant, and we get $A_{V_{SF}} = 0.854 \pm 0.05$. Due to the inclination of the system (Fig. 4.14), we have averaged the flux of every component in V band of quadratures $\phi_o = 0.25$, $\phi_o = 0.75$ and obtained the total flux $f_t = 4.3 \pm 0.15$ with the individual flux contributions for the donor of $f_d = 1.05 \pm 0.05$, the gainer $f_g = 0.3 \pm 0.05$ and the disc $f_{disc} = 2.95 \pm 0.05$. Therefore, apparent magnitudes can be derive by the following equation :

$$m_{d,g} - m_t = -2.5\log\left(\frac{f_{d,g}}{f_t}\right) \quad (4.18)$$

Considering the previous equation (Eq. 17), we computed the apparent magnitude for the donor star $m_d = 9.816 \pm 0.071$ mag , while for the gainer is $m_g = 11.176 \pm 0.175$ mag and the bolometric corrections were obtained according to Torres (2010) for $\log(T) > 3.90$. Hence, for the logarithmic temperature of the donor $\log(T_d) = 3.978 \pm 0.016$, corresponds a bolometric correction $BC_d = -0.150 \pm 0.041$ and for $\log(T_g) = 4.131 \pm 0.016$ corresponds $BC_g = -0.984 \pm 0.058$. Finally, we computed the individual distance of the donor and gainer and determined the distance modulus, using the follow equation :

$$d_{d,g}(pc) = 10^{((m_{d,g} - M_{d,g})_0 + 5)/5} \quad (4.19)$$

We computed separately the donor distance $d_d = 1159.652 \pm 159.784$ pc and for the gainer $d_g = 1118.476 \pm 105.419$ pc, respectively. Hence, the average distance for the system $d = 1138.5 \pm 191.426$ pc, which is in agreement with the distance published by Gaia TGAS¹⁴ $d_{Gaia} = 1174.841 \pm 373.787$

¹³<http://irsa.ipac.caltech.edu/applications/DUST/>

¹⁴<http://gea.esac.esa.int/archive/>

pc. The difference between the distance of the donor and gainer can be interpreted as the estimation of the intrinsic error of the method considering between other error sources that the gainer star is hidden by a disc optically thick and that the visual extinction was crudely estimated from a dust map in the surrounding sky zone.

4.7.2 Position in the H-R Diagram

We have implemented a theoretical model which evolves a binary system of intermediate mass, considering a hot star which can not accrete to high rate, limited by the Eddington accretion rate and begins at the zero-age main sequence for both stars, applying the modern stellar evolution code MESA¹⁵ (Eggleton, 1971; Paxton, 2004; Paxton et al., 2011, 2013, 2015, 2018) developed to calculate evolution of stars in a wide range of environments, as first approximation to understand the evolutionary process of the DPV HD50526. First, we compared the theoretical model with published values of masses, radius, age and orbital period of β Lyrae (Mennickent & Djurašević, 2013), which is an interacting binary well studied, and the model presented a great consistency with this interacting binary system and reproduced very well the values.

We must remember that the total mass of the system is $6.91 \pm 0.04 M_{\odot}$. For this reason we considered to HD 50526 as an intermediate mass system, which belongs to the lower edge. Therefore we used a mass ratio interval between $0.25 < q < 0.55$ because larger differences would not allow an interacting binary evolution and less ensure the convergence of the model. Hence, we initiated the DPV model at the zero age main sequence (ZAMS), adopting an initial orbital period of 2.0 to 2.25 with step of 0.05 d, an initial mass for the primary component (donor) of 5.6 to 4.4 M_{\odot} with step 0.1 M_{\odot} and for the companion of 1.4 to 2.5 M_{\odot} with steps of 0.1 M_{\odot} and an associated metallicity of $Z=0.02$. In addition for this model we have considered the mass transfer efficiency and we took into account the following mass loss/transfer fractions: α whose meant is associated to spherically symmetric outflow from the donor star in form of a fast wind, called Jeans's mode, where we considered a low fraction of factor 10^{-15} and another faster than the previous of 10^{-3} ; the same we have did to β , which the flow is transported from the donor star to the vicinity of the accretor, where it is ejected as a fast isotropic wind, using a factor of 10^{-15} and a fast factor of 10^{-4} . Later we implemented a chi-square adjustments considering a confidence of 95% using 16 freedom degree, i.e. $\chi^2_{critic0.95,16}$, and the optimization method converged successfully for the initial parameters of orbital period $P = 2.10$ days, mass of the donor star $M = 5.2 M_{\odot}$, mass of the gainer $M = 1.8 M_{\odot}$ with a chi-square of $\chi^2_{0.95,16} = 6.663$. Due to $\chi^2_{0.95,16} < \chi^2_{critic0.95,16}$, then the solution is accepted (Fig. 4.15).

The model shows that both stars begin their evolutionary process from the zero-age main sequence of different way. The donor evolves increasing its size and onset the mass transfer, causing the first hook in its evolutionary track depleting rapidly great part of its central hydrogen (Fig. 4.15). During this process, the donor decreases their luminosity around 2.0 orders of magnitude. While the gainer increases their mass and ascends through of the main sequence, placing itself in a new position inside of it, now it is more hotter and brighter. Once that the optically thick mass transfer is constant, the gainer star onset its evolution leaving the main sequence. When the mass inversion occurs, it provokes the second hook on the evolutionary track of the gainer, driving it to a new stage in its evolution, while the mass transfer decrease. But a new onset of the mass transfer causing the second hook on the gainer and rejuvenate it and place it near the beginning of the donor star. Also, we noted that the gainer star shows a systematic phase of increase and decrease of their radius until reaching the current position. The results suggests that the age of the system is 1.416584×10^8 yr. The donor star is lightly less hotter and brighter when reaches the current mass $M_d \sim 1.05 M_{\odot}$, the same occurs for the gainer which it is less hotter and luminous than our

¹⁵<http://mesa.sourceforge.net/>

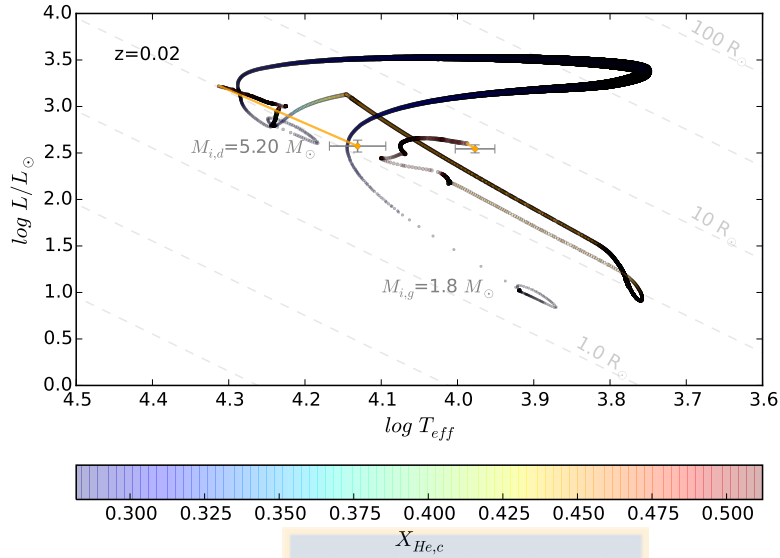


Figure 4.15: Hertzsprung-Russell diagram of binary evolutionary track. The donor star onsets with a mass $M_{i,d} = 5.20 M_{\odot}$ while the gainer with $M_{i,g} = 1.8 M_{\odot}$ for an initial orbital period $P_{i,o} = 2.10$ days. The stellar tracks were calculated with $Z = 0.02$ and the color bar shows the central hydrogen mass fraction for both components. The track was represented using circles that show the change of the stellar radius for both components. The orange lines connects the best model solution with the observed data.

model when reaches a similar mass $M_g \sim 5.86 M_{\odot}$.

Table 4.3: Comparison between the results of the theoretical model for HD 50526 obtained with MESA code, with a confidence interval of 95% and 16 freedom degree, versus the inverse problem for the Roche model analyzing the light curve in V-filter.

Parameters	MESA	Observed
Age [Myr]	141.658	—
$M_h [M_{\odot}]$	5.900	5.86 ± 0.02
$M_c [M_{\odot}]$	1.054	1.05 ± 0.02
$R_h [R_{\odot}]$	3.201	3.54 ± 0.03
$R_c [R_{\odot}]$	7.054	6.92 ± 0.01
$\log g_h$	4.198	4.11 ± 0.02
$\log g_c$	2.763	2.78 ± 0.02
$T_h [K]$	20568.938	13510 ± 500
$T_c [K]$	9718.449	9500 ± 250

4.7.3 Spectral Energy Distribution (SED)

To characterize the energy emitted by the DPV HD 50526 and interpret the information around $H\alpha$, we compiled the available information from VizieR Photometric viewer¹⁶ in the Table 4.9, building a spectral energy distribution (SED). First we have selected synthetic models from Virtual Observatory SED Analyzer¹⁷ (Bayo et al., 2008) of single stars for the donor and gainer, considering the errors of each component and build a grid to constraint results obtained in the previous sections. The best fitting model is obtained developing a test of chi-square, using the composite flux of Fitzpatrick & Massa (2005) for our system of the follow way :

$$f_{\lambda} = f_{\lambda,0} 10^{-0.4E(B-V)[k(\lambda-V)+R(V)]} \quad (4.20)$$

where $f_{\lambda,0}$ is the intrinsic surface flux of both stars at wavelength λ , and we consider to d as a free parameter measured in parsec, which can be determinated as:

$$f_{\lambda,0} = \left(\frac{R_2}{d}\right)^2 \left[\left(\frac{R_1}{R_2}\right)^2 f_{1,\lambda} + f_{2,\lambda} \right] \quad (4.21)$$

the parameters $f_{1,\lambda}$ and $f_{2,\lambda}$ are the fluxes of the gainer and donor stars respectively. $R(V) \equiv A(\lambda)/E(B-V)$ is the ratio of total extinction to reddening, R_1 and R_2 correspond to the radius of the primary and secondary star and $k(\lambda - V) \equiv E(\lambda - V)/E(B - V)$ is the normalized extinction curve, which can be computed as:

$$k = \begin{cases} \varepsilon\lambda^{-\beta} - R_v & \text{if } x < 0.3 \\ R_v \left(a(x) + \frac{b(x)}{R_v} - 1 \right) & \text{if } 0.3 \leq x \leq 8.0 \end{cases} \quad (4.22)$$

wherein the inverse of the wavelength corresponds to $x \equiv 1/\lambda$ (μm^{-1}), and the parameters $\varepsilon = 1.19$, $\beta = 1.84$ and $R_v = 3.05$ have a formal error around 1% (Martin & Whittet, 1990). Is necessary emphasize that β is not applicable at wavelengths beyond $5 \mu m$, while the parameters $a(x)$ and $b(x)$ are the parametrization coefficients for the extinction law from Cardelli et al. (1989). The best theoretical model considers a metallicity index $[M/H]=0.0$, i.e. solar metallicity for both stars, an effective temperature for the donor of $T_d = 9500$ K and $\log g_d = 2.5$ dex. The effective temperature of the gainer is between 13000 to 14000 K with steps of 1000 K and a $\log g_g$ of 4.0 to 4.5 dex with steps of 0.5 dex corresponding to the obtained values with their respective errors. Also we measured the equivalent width of the diffuse interstellar band (DIB) located at 5780 Å for determine the reddening that suffer the absorption lines. We used the coefficients of regression line of Herbig (1993), for the DIB at 5780 Å and we determined that $E(B-V) = 0.2703$. Very similar to the value published by IRSA¹⁸.

The difference between both values is due to that IRSA offer a mean value for all the light of sight. While we have used a DIB to determinate with more accuracy this value. Also, we noted a small difference between the theoretical $k(\lambda - V)$ and the observed (Fig. 4.16), which it is directly

¹⁶<http://vizier.u-strasbg.fr/vizier/sed/>

¹⁷<http://svo2.cab.inta-csic.es/theory/vosa/>

¹⁸<http://irsa.ipac.caltech.edu/applications/DUST/>

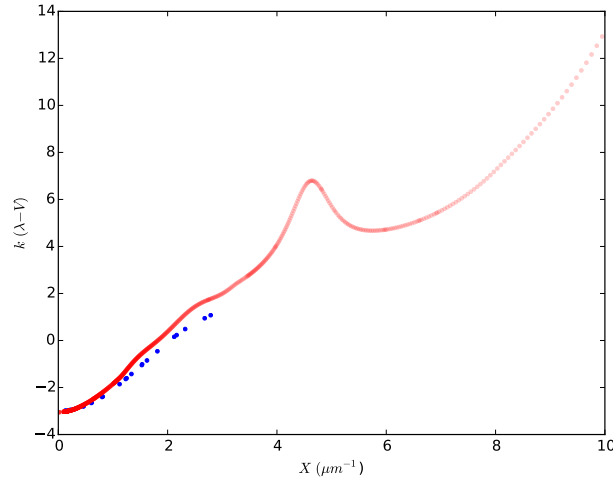


Figure 4.16: Comparison between the theoretical normalized extinction curve (red) and the observed (blue) obtained by IRSA. The great effect of varying that occurs in R_v changes the shape of the extinction curve at the shorter wavelengths. Therefore, is not correct to extrapolate the values close to the FUV but we can affirm that the effect is less than the theoretical k .

related with the free parameter of the distance. However, the system is slightly reddened, and we could replace the extinction curve $k(\lambda - V)$ for a mean value, as free parameter, without loss a lot of accuracy.

Therefore with all this, we have performed again a chi square test and obtained the best value for the extinction curve normalized $k(\lambda - V) = -3.0$, consider a distance with a 5% of error for 8 degrees of freedom, i.e. $\chi_{critic0.90,8}^2$ and we found a distance of $d = 1100$ pc with $\chi^2 = 2.528$. Due to $\chi^2 < \chi_{critic0.90,8}^2$, then the solution is accepted. Possibly, the difference is greater due we does not considering the contribution of a luminous disc illuminated by their accretor. Also we noted that the spectral energy distribution shows an excess of infrared from 12400 \AA , which indicate the presence of a circumstellar material (Fig. 4.17).

In conclusion, the composite spectral energy distribution will directly depend on whether the system is slightly reddened or not. If the system is too red, use equation 22 to then solve equations 21 and 20, while for the opposite case it is allowed to replace the extinction curve with a free value for its adjustment. However, the only free parameter corresponds to the distance of the system corresponding to equation 21, which will allow us to know the distance to which our system is located. The analysis carried out by the SED allowed to characterize the system and confirm its physical parameters such as: superficial gravity and metallicity, temperature of both components using 22 calibrated flows obtained with Vizier, besides being able to determine its distance

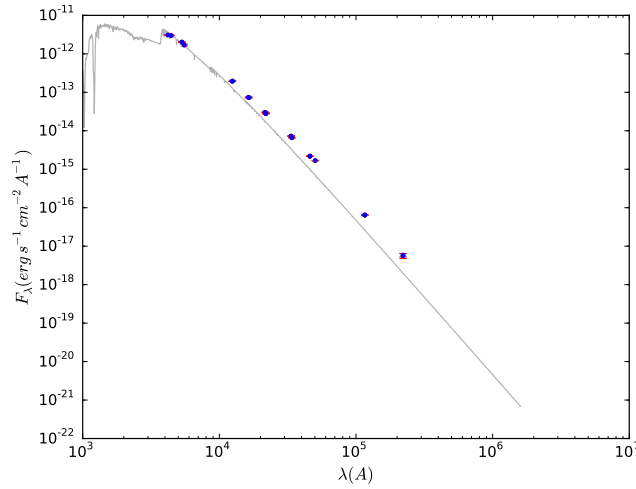


Figure 4.17: Best fit of spectral energy distribution, considering a composed flux by two stars without consider the contribution of the disc.

4.8 Conclusions

In this work we have studied the long term variability of the DPV HD50526, using several spectrographs of high and medium resolution, covering a range from 352.1 to 872.2 nm for a series of 140 spectra uniformly distributed on the orbital period. We summarize our main conclusions as follows :

- From photometric study from ASAS data, we determined that the DPV HD 50526 shows and orbital period of $P_o = 6.701 \pm 0.001$ d and a long period of $P_l = 190.584 \pm 0.889$ d. Also we have presented the best orbital parameters using PIKAIA code and are given in Table 4.1.
- Through the use of Djurasevic's code we have determined the mass of the donor star $M_2 = 1.05 \pm 0.02 M_\odot$ with a temperature $T_2 = 9500 \pm 250$ K and radius $R_2 = 6.92 \pm 0.01 R_\odot$, while the companion or gainer star have a mass $M_1 = 5.86 \pm 0.02 M_\odot$, a temperature $T_1 = 13510 \pm 500$ K and finally a radius $R_1 = 3.54 \pm 0.03 R_\odot$.
- The gainer star is surrounded by and optical and geometrically luminous accretion disk, with radial extension $R_d = 14.9 \pm 0.02 R_\odot$, which It is around 4.2 time more larger than its accretor. In addition the accretion disk hides around $\sim 32\%$ of the hot star, and it has an elevated temperature of $T_d = 9260 \pm 200$ K.
- We have considered the luminosity of the disc in form of black body and computed that luminosity of disc is $806.000 \pm 21.988 L_\odot$, which is interpreted as a bright and hot disc illuminated from the inside by its accretor.
- The mass transfer $\dot{M} = 3.100 \times 10^{-5} \pm 3.140 \times 10^{-7} M_\odot \text{ yr}^{-1}$ is a normal value for systems as the DPV, and show a rate of energy gained by accretion of matter of $\eta_{acc} = 3.513 \times 10^{-6} \pm 3.209 \times 10^{-8}$.
- During the quadratures the donor, gainer and disc contribute with a 24.4%, 6.9% and a 68.6% of the total flux. Also the disc shows a hot and bright spot located on the edge, and its is one more reason whereby the disc presents greater contribution that its central star.

- The hot spot presents a temperature $T_{hs} = 12964 \pm 335$ K very similar to the gainer, while the bright spot $T_{bs} = 10926 \pm 300$ K is slightly more cold.
- The DPV HD 50526 is found slightly reddened and the color excess $E(B-V) = 0.2703$ which were determined using the DIB located at 5780 \AA .
- The system also shown an excess of infrared from 12400 \AA in the spectral energy distribution, which indicates the presence of a circumstellar material for a distance of 1100 pc with a $\chi^2_{0.90,8} = 2.528$.
- The DPV model performed with MESA code, suggest that for an initial orbital period $P_{i,o} = 2.10$ days, $M_{i,d} = 5.2 M_{\odot}$ and $M_{i,g} = 1.8 M_{\odot}$ with a chi-square of $\chi^2_{0.95,16} = 6.663$. Also the gainer star is less luminous and hot than the model indicates, while the donor star is slightly less luminous and hot. The current age of HD 50526 was estimated 141.6584 Myr .



Table 4.4: Summary of spectroscopic observation using CORALIE spectrograph, where N is number of spectra per date. The HJD at mid-exposure for the first spectrum series is given, the orbital (Φ_o) and long cycle (Φ_l) phases were calculated using the Eq. 1 and Eq. 2 respectively with a spectral resolution of $R \sim 60000$

UT-date	Observatory/Telescope	Instrument	N	exptime (s)	HJD	ϕ_o	ϕ_l	S/N	R
2008-04-05	ESO/EULER	CORALIE	1	600	2454562.48183587	0.255	0.517	58.63	60000
2008-04-05	ESO/EULER	CORALIE	1	600	2454562.48967077	0.257	0.517	40.06	60000
2008-04-05	ESO/EULER	CORALIE	1	900	2454562.49923005	0.258	0.517	53.72	60000
2008-04-05	ESO/EULER	CORALIE	1	900	2454562.51053684	0.260	0.517	56.74	60000
2008-04-06	ESO/EULER	CORALIE	1	1200	2454563.48660112	0.405	0.523	80.98	60000
2008-04-06	ESO/EULER	CORALIE	1	1200	2454563.50136823	0.408	0.523	72.66	60000
2008-04-06	ESO/EULER	CORALIE	1	1200	2454563.51613534	0.410	0.523	87.38	60000
2008-04-07	ESO/EULER	CORALIE	1	900	2454564.47754834	0.553	0.528	77.13	60000
2008-04-07	ESO/EULER	CORALIE	1	900	2454564.48884356	0.555	0.528	75.25	60000
2008-04-07	ESO/EULER	CORALIE	1	900	2454564.50013878	0.557	0.528	82.24	60000
2008-04-08	ESO/EULER	CORALIE	1	900	2454565.48752165	0.704	0.533	96.06	60000
2008-04-08	ESO/EULER	CORALIE	1	900	2454565.49882845	0.706	0.533	69.98	60000
2008-04-08	ESO/EULER	CORALIE	1	900	2454565.51012367	0.707	0.533	65.50	60000
2008-05-22	ESO/EULER	CORALIE	1	900	2454609.48284187	0.269	0.764	48.53	60000
2008-05-22	ESO/EULER	CORALIE	1	900	2454609.49441520	0.271	0.764	86.80	60000
2008-05-23	ESO/EULER	CORALIE	1	900	2454610.45414630	0.414	0.769	81.35	60000
2008-05-23	ESO/EULER	CORALIE	1	900	2454610.46548819	0.415	0.769	65.35	60000
2008-05-23	ESO/EULER	CORALIE	1	900	2454610.47678378	0.417	0.769	99.96	60000
2008-10-02	ESO/EULER	CORALIE	1	1000	2454741.83096102	0.018	0.458	67.80	60000
2008-10-02	ESO/EULER	CORALIE	1	1000	2454741.84341591	0.020	0.458	68.11	60000
2008-10-03	ESO/EULER	CORALIE	1	1200	2454742.84518965	0.169	0.464	45.16	60000
2008-10-04	ESO/EULER	CORALIE	1	1200	2454743.82668378	0.315	0.469	82.88	60000
2008-10-04	ESO/EULER	CORALIE	1	1200	2454743.84618795	0.318	0.469	62.63	60000
2008-12-19	ESO/EULER	CORALIE	1	900	2454819.70376246	0.638	0.867	73.19	60000
2008-12-20	ESO/EULER	CORALIE	1	900	2454820.69211018	0.785	0.872	79.27	60000
2008-12-22	ESO/EULER	CORALIE	1	900	2454822.70360483	0.085	0.883	72.78	60000
2009-04-15	ESO/EULER	CORALIE	1	900	2454937.47435090	0.211	0.485	66.91	60000
2009-04-15	ESO/EULER	CORALIE	1	900	2454937.48568086	0.213	0.485	70.36	60000
2009-04-15	ESO/EULER	CORALIE	1	900	2454937.49702239	0.215	0.485	67.06	60000
2009-04-16	ESO/EULER	CORALIE	1	900	2454937.50836392	0.216	0.485	66.16	60000
2009-04-16	ESO/EULER	CORALIE	1	1200	2454938.47947708	0.361	0.490	75.73	60000
2009-04-16	ESO/EULER	CORALIE	1	1200	2454938.49425580	0.364	0.490	79.77	60000
2009-04-17	ESO/EULER	CORALIE	1	1200	2454938.50903451	0.366	0.490	75.59	60000
2009-04-17	ESO/EULER	CORALIE	1	1200	2454938.52381323	0.368	0.490	80.51	60000
2009-04-17	ESO/EULER	CORALIE	1	1200	2454938.53859195	0.370	0.490	72.35	60000
2009-05-16	ESO/EULER	CORALIE	1	900	2454968.45579766	0.834	0.647	70.39	60000
2009-05-16	ESO/EULER	CORALIE	1	900	2454968.46713945	0.836	0.648	90.59	60000

Table 4.5: Summary of spectroscopic observation using ECHELLE spectrograph, where N is number of spectra per date. The HJD at mid-exposure for the first spectrum series is given, the orbital (Φ_o) and long cycle (Φ_l) phases were calculated using the Eq. 1 and Eq. 2 respectively with a spectral resolution of $R \sim 18000$

UT-date	Observatory/Telescope	Instrument	N	exptime (s)	HJD	ϕ_o	ϕ_l	S/N	R
2009-11-04	SPM/SPMT	Echelle	1	1200	2455140.04944751	0.548	0.548	45.18	18000
2009-11-05	SPM/SPMT	Echelle	1	1200	2455141.04128960	0.553	0.553	97.95	18000
2009-11-12	SPM/SPMT	Echelle	1	1200	2455142.98124607	0.563	0.563	141.99	18000
2009-11-12	SPM/SPMT	Echelle	1	1200	2455143.94206029	0.568	0.568	73.10	18000
2009-11-12	SPM/SPMT	Echelle	1	900	2455144.87802708	0.573	0.573	101.01	18000
2009-11-12	SPM/SPMT	Echelle	1	900	2455144.88912728	0.573	0.573	98.14	18000
2009-11-12	SPM/SPMT	Echelle	1	900	2455144.90022751	0.573	0.573	91.14	18000
2009-11-12	SPM/SPMT	Echelle	1	900	2455146.01491087	0.579	0.579	84.30	18000
2009-11-12	SPM/SPMT	Echelle	1	900	2455146.02601127	0.579	0.579	114.48	18000
2009-11-12	SPM/SPMT	Echelle	1	900	2455146.03710007	0.579	0.579	113.51	18000
2009-12-09	SPM/SPMT	Echelle	1	1200	2455171.91678429	0.195	0.715	130.92	18000
2009-12-09	SPM/SPMT	Echelle	1	1200	2455171.93134509	0.197	0.715	129.76	18000
2009-12-09	SPM/SPMT	Echelle	1	1200	2455171.94591749	0.199	0.715	154.53	18000
2009-12-09	SPM/SPMT	Echelle	1	1200	2455172.98771418	0.354	0.721	25.51	18000
2009-12-09	SPM/SPMT	Echelle	1	1200	2455173.00228659	0.357	0.721	36.33	18000
2011-01-27	SPM/SPMT	Echelle	1	900	2455586.76571973	0.098	0.892	98.19	18000
2011-01-27	SPM/SPMT	Echelle	1	900	2455587.76936629	0.248	0.897	79.83	18000
2011-01-28	SPM/SPMT	Echelle	1	900	2455588.69713235	0.386	0.902	117.34	18000
2011-01-28	SPM/SPMT	Echelle	1	900	2455589.70166633	0.536	0.907	95.55	18000
2012-02-11	SPM/SPMT	Echelle	1	1200	2455968.82382656	0.108	0.896	187.20	18000
2012-02-12	SPM/SPMT	Echelle	1	1200	2455969.88029338	0.266	0.902	156.54	18000
2012-02-13	SPM/SPMT	Echelle	1	1200	2455970.75980939	0.397	0.907	194.38	18000
2012-02-14	SPM/SPMT	Echelle	1	1200	2455971.78222342	0.550	0.912	182.25	18000
2012-02-15	SPM/SPMT	Echelle	1	1200	2455972.87665882	0.713	0.918	6.25	18000
2012-02-19	SPM/SPMT	Echelle	1	1200	2455975.70836929	0.136	0.933	178.23	18000
2012-02-19	SPM/SPMT	Echelle	1	1200	2455975.79925421	0.149	0.933	155.24	18000
2012-02-19	SPM/SPMT	Echelle	1	1200	2455975.86411098	0.159	0.933	157.06	18000
2012-02-19	SPM/SPMT	Echelle	1	1200	2455976.61805307	0.271	0.937	162.42	18000
2012-02-19	SPM/SPMT	Echelle	1	1200	2455976.78931463	0.297	0.938	163.90	18000
2012-02-20	SPM/SPMT	Echelle	1	1200	2455977.64297014	0.424	0.943	120.89	18000
2012-02-20	SPM/SPMT	Echelle	1	1200	2455977.73496695	0.438	0.943	120.24	18000
2012-02-21	SPM/SPMT	Echelle	1	1200	2455978.75980151	0.591	0.949	63.40	18000
2012-02-21	SPM/SPMT	Echelle	1	1200	2455978.77386302	0.593	0.949	39.26	18000
2012-02-22	SPM/SPMT	Echelle	1	1200	2455979.70671364	0.732	0.954	162.61	18000
2012-02-22	SPM/SPMT	Echelle	1	1200	2455979.72076366	0.734	0.954	178.13	18000
2012-02-23	SPM/SPMT	Echelle	1	1200	2455980.70032159	0.880	0.959	107.49	18000
2012-11-13	SPM/SPMT	Echelle	1	1200	2456245.02839128	0.323	0.346	192.24	18000
2012-11-14	SPM/SPMT	Echelle	1	1200	2456245.91058693	0.455	0.350	160.04	18000
2012-11-18	SPM/SPMT	Echelle	1	1200	2456250.00101000	0.065	0.372	170.72	18000
2012-11-19	SPM/SPMT	Echelle	1	1200	2456250.87730000	0.196	0.376	135.82	18000
2013-01-28	SPM/SPMT	Echelle	1	1200	2456320.72825435	0.619	0.743	131.94	18000
2013-01-28	SPM/SPMT	Echelle	1	1200	2456320.74231642	0.621	0.743	144.85	18000
2013-01-28	SPM/SPMT	Echelle	1	1200	2456320.75639001	0.623	0.743	139.53	18000
2013-01-30	SPM/SPMT	Echelle	1	1200	2456322.73900591	0.919	0.753	106.96	18000
2013-01-30	SPM/SPMT	Echelle	1	1200	2456322.75306786	0.921	0.753	138.05	18000
2013-01-30	SPM/SPMT	Echelle	1	1200	2456322.76714142	0.923	0.754	173.78	18000
2015-01-13	SPM/SPMT	Echelle	1	1200	2457035.95402000	0.344	0.496	154.77	18000
2015-01-13	SPM/SPMT	Echelle	1	1200	2457035.96816000	0.346	0.496	132.48	18000
2015-01-13	SPM/SPMT	Echelle	1	1200	2457035.98227000	0.349	0.496	147.27	18000

Table 4.6: Summary of spectroscopic observation using CHIRON spectrograph, where N is number of spectra per date. The HJD at mid-exposure for the first spectrum series is given, the orbital (Φ_o) and long cycle (Φ_l) phases were calculated using the Eq. 1 and Eq. 2 respectively with a spectral resolution of $R \sim 80000$ (Slicer mode).

UT-date	Observatory/Telescope	Instrument	N	exptime (s)	HJD	ϕ_o	ϕ_l	S/N	R
2012-11-05	CTIO/1.5m	CHIRON	1	1200	2456236.80526037	0.096	0.303	64.16	80000
2012-11-08	CTIO/1.5m	CHIRON	1	1200	2456239.79422590	0.542	0.318	53.81	80000
2012-11-08	CTIO/1.5m	CHIRON	1	1200	2456239.80832071	0.544	0.318	56.84	80000
2012-11-08	CTIO/1.5m	CHIRON	1	1200	2456239.82241444	0.546	0.318	56.32	80000
2012-11-11	CTIO/1.5m	CHIRON	1	1200	2456242.82871200	0.997	0.334	60.35	80000
2012-11-11	CTIO/1.5m	CHIRON	1	1200	2456242.84280691	0.997	0.334	60.52	80000
2012-11-11	CTIO/1.5m	CHIRON	1	1200	2456242.85690172	0.999	0.334	57.91	80000
2012-11-14	CTIO/1.5m	CHIRON	1	1200	2456245.78951280	0.437	0.350	61.58	80000
2012-11-14	CTIO/1.5m	CHIRON	1	1200	2456245.80360880	0.439	0.350	60.90	80000
2012-11-14	CTIO/1.5m	CHIRON	1	1200	2456245.81770132	0.441	0.350	44.02	80000
2012-11-17	CTIO/1.5m	CHIRON	1	1200	2456248.71775822	0.874	0.365	52.34	80000
2012-11-17	CTIO/1.5m	CHIRON	1	1200	2456248.73185306	0.876	0.365	58.97	80000
2012-11-17	CTIO/1.5m	CHIRON	1	1200	2456248.74594790	0.878	0.365	55.82	80000
2012-11-20	CTIO/1.5m	CHIRON	1	1200	2456251.73843209	0.325	0.381	61.03	80000
2012-11-20	CTIO/1.5m	CHIRON	1	1200	2456251.75252803	0.327	0.381	62.16	80000
2012-11-20	CTIO/1.5m	CHIRON	1	1200	2456251.76662151	0.329	0.381	68.75	80000
2012-11-25	CTIO/1.5m	CHIRON	1	1200	2456256.83286117	0.085	0.408	58.58	80000
2012-11-28	CTIO/1.5m	CHIRON	1	1200	2456259.70042938	0.513	0.423	51.29	80000
2012-11-28	CTIO/1.5m	CHIRON	1	1200	2456259.71452406	0.515	0.423	47.15	80000
2012-11-28	CTIO/1.5m	CHIRON	1	1200	2456259.72861750	0.517	0.423	44.42	80000
2012-12-04	CTIO/1.5m	CHIRON	1	1200	2456265.78505374	0.421	0.455	60.72	80000
2012-12-04	CTIO/1.5m	CHIRON	1	1200	2456265.79914814	0.423	0.455	50.97	80000
2012-12-04	CTIO/1.5m	CHIRON	1	1200	2456265.81324131	0.425	0.455	49.38	80000
2013-11-04	CTIO/1.5m	CHIRON	1	1000	2456600.84049212	0.417	0.213	37.58	80000
2013-11-04	CTIO/1.5m	CHIRON	1	1000	2456600.85227210	0.419	0.213	26.30	80000
2013-11-04	CTIO/1.5m	CHIRON	1	1000	2456600.86405207	0.421	0.213	24.72	80000
2013-11-06	CTIO/1.5m	CHIRON	1	1200	2456602.82314142	0.713	0.223	46.29	80000
2013-11-06	CTIO/1.5m	CHIRON	1	1200	2456602.83723646	0.715	0.223	48.93	80000
2013-11-06	CTIO/1.5m	CHIRON	1	1200	2456602.85133027	0.717	0.223	49.25	80000
2013-11-08	CTIO/1.5m	CHIRON	1	1200	2456604.78689240	0.006	0.233	56.70	80000
2013-11-08	CTIO/1.5m	CHIRON	1	1200	2456604.80098707	0.008	0.233	56.68	80000
2013-11-08	CTIO/1.5m	CHIRON	1	1200	2456604.81508074	0.010	0.233	59.71	80000
2013-11-12	CTIO/1.5m	CHIRON	1	1200	2456608.84935936	0.612	0.255	48.33	80000
2013-11-12	CTIO/1.5m	CHIRON	1	1200	2456608.86345529	0.614	0.255	49.33	80000
2013-11-12	CTIO/1.5m	CHIRON	1	1200	2456608.87754884	0.616	0.255	29.91	80000
2013-11-17	CTIO/1.5m	CHIRON	1	1200	2456613.74164809	0.342	0.280	44.41	80000
2013-11-17	CTIO/1.5m	CHIRON	1	1200	2456613.75574294	0.344	0.280	48.97	80000
2013-11-17	CTIO/1.5m	CHIRON	1	1200	2456613.76983652	0.346	0.280	44.86	80000
2013-11-18	CTIO/1.5m	CHIRON	1	1200	2456614.79142646	0.499	0.286	47.82	80000
2013-11-18	CTIO/1.5m	CHIRON	1	1200	2456614.80552017	0.501	0.286	50.66	80000
2013-11-18	CTIO/1.5m	CHIRON	1	1200	2456614.81961616	0.503	0.286	45.71	80000
2013-11-20	CTIO/1.5m	CHIRON	1	1200	2456616.80744009	0.800	0.296	50.03	80000
2013-11-20	CTIO/1.5m	CHIRON	1	1200	2456616.82153479	0.802	0.296	49.97	80000
2013-11-20	CTIO/1.5m	CHIRON	1	1200	2456616.83562947	0.804	0.297	45.98	80000
2013-11-22	CTIO/1.5m	CHIRON	1	1200	2456618.78744321	0.095	0.307	44.20	80000
2013-11-22	CTIO/1.5m	CHIRON	1	1200	2456618.80153801	0.097	0.307	38.86	80000
2013-11-22	CTIO/1.5m	CHIRON	1	1200	2456618.81563157	0.099	0.307	48.80	80000
2013-11-24	CTIO/1.5m	CHIRON	1	1200	2456620.71242225	0.382	0.317	23.02	80000
2013-11-24	CTIO/1.5m	CHIRON	1	1200	2456620.72651699	0.385	0.317	24.71	80000
2013-11-24	CTIO/1.5m	CHIRON	1	1200	2456620.74061160	0.387	0.317	24.32	80000
2013-11-26	CTIO/1.5m	CHIRON	1	1200	2456622.78521955	0.692	0.328	45.27	80000
2013-11-26	CTIO/1.5m	CHIRON	1	1200	2456622.81340771	0.696	0.328	46.44	80000
2013-12-16	CTIO/1.5m	CHIRON	1	1200	2456642.74995625	0.671	0.433	22.86	80000
2013-12-16	CTIO/1.5m	CHIRON	1	1200	2456642.76405042	0.673	0.433	23.86	80000
2013-12-16	CTIO/1.5m	CHIRON	1	1200	2456642.77814343	0.675	0.433	24.77	80000

Table 4.7: Radial velocities of the donor and their respective errors, using Mg 4482 Å

HJD	RV (km s ⁻¹)	error (km s ⁻¹)
2454741.83096102	6.008	1.773
2454741.84341591	9.223	1.773
2454822.70360483	18.980	1.768
2454937.47435090	39.181	1.768
2454937.49702239	28.192	1.769
2454937.50836392	37.231	1.768
2454562.48183587	33.628	1.773
2454562.49923005	32.419	1.770
2454562.51053684	28.621	1.770
2454609.48284187	28.691	1.777
2454743.82668378	12.701	1.772
2454743.84618795	24.607	1.774
2454938.47947708	15.317	1.782
2454938.49425580	11.562	1.774
2454938.50903451	26.284	1.771
2454938.52381323	9.904	1.769
2454938.53859195	6.569	1.770
2454563.48660112	21.457	1.776
2454563.50136823	19.900	1.768
2454563.51613534	8.110	1.769
2454610.45414630	1.593	1.773
2454610.46548819	3.183	1.784
2454610.47678378	3.843	1.775
2454564.47754834	-14.869	1.773
2454564.50013878	-17.607	1.775
2454819.70376246	-27.225	1.772
2454565.48752165	-28.563	1.778
2454565.49882845	-23.635	1.769
2454565.51012367	-4.828	1.771
2454820.69211018	-28.717	1.768
2454968.45579766	-45.319	1.780
2454968.46713945	-18.569	1.771

Table 4.8: Radial velocities of the gainer and their respective errors, using HeI 4471 Å

HJD	RV (km s ⁻¹)	error (km s ⁻¹)
2454741.83096102	-24.721	0.565
2454741.84341591	-30.537	0.564
2454822.70360483	-92.043	0.559
2454742.84518965	-154.188	0.576
2454937.47435090	-161.451	0.560
2454937.48568086	-157.314	0.563
2454937.49702239	-160.555	0.560
2454937.50836392	-161.689	0.564
2454562.48183587	-162.900	0.562
2454562.48967077	-159.843	0.570
2454562.49923005	-163.126	0.564
2454562.51053684	-161.700	0.563
2454609.48284187	-157.162	0.568
2454609.49441520	-163.301	0.573
2454743.82668378	-144.197	0.565
2454743.84618795	-141.973	0.564
2454938.47947708	-115.712	0.564
2454938.49425580	-113.772	0.564
2454938.50903451	-112.957	0.563
2454938.52381323	-111.983	0.562
2454938.53859195	-108.396	0.563
2454563.48660112	-83.198	0.563
2454563.50136823	-77.460	0.641
2454563.51613534	-78.577	0.563
2454610.45414630	-81.058	0.567
2454610.46548819	-73.779	0.564
2454610.47678378	-73.476	0.569
2454564.47754834	59.130	0.564
2454564.48884356	61.890	0.563
2454564.50013878	62.013	0.563
2454819.70376246	128.833	0.560
2454565.48752165	159.604	0.562
2454565.49882845	155.228	0.561
2454565.51012367	158.355	0.561
2454820.69211018	155.554	0.561
2454968.45579766	140.670	0.562
2454968.46713945	137.023	0.565

Table 4.9: Photometry points extracted from VizieR Catalogue with a search radius of 2 arsec to build the Spectral Energy Distribution

wavelength A	Obs. Flux erg/s/cm ² /A	Obs. Error erg/s/cm ² /A	Filter ID
4200	3.090E-12	5.090E-14	HIP:BT
4440	2.990E-12	4.560E-14	Johnson:B
5320	2.030E-12	2.120E-14	HIP:VT
5320	2.010E-12	3.180E-14	HIP:VT
5540	1.690E-12	8.800E-14	Johnson:V
12400	1.940E-13	3.120E-15	2MASS:J
12500	1.960E-13	3.840E-15	Johnson:J
16299	7.400E-14	2.140E-15	Johnson:H
16500	7.310E-14	1.980E-15	2MASS:H
21600	3.030E-14	7.680E-16	2MASS:Ks
21900	2.860E-14	6.880E-16	Johnson:K
21900	2.850E-14	5.000E-16	Johnson:K
21900	2.790E-14	6.250E-16	Johnson:K
33500	7.270E-15	1.600E-16	WISE:W1
33500	7.210E-15	1.870E-16	WISE:W1
34000	6.560E-15	1.820E-16	Johnson:L
46000	2.200E-15	4.250E-17	WISE:W2
46000	2.170E-15	4.250E-17	WISE:W2
50300	1.680E-15	2.370E-17	Johnson:M
116000	6.460E-17	1.120E-18	WISE:W3
116000	6.420E-17	1.120E-18	WISE:W3
221000	5.850E-18	5.900E-19	WISE:W4
221000	5.630E-18	8.420E-19	WISE:W4

Chapter 5

Spectroscopic and photometric study of the eclipsing interacting binary V495 Centauri

Rosales, J.A.¹, Mennickent, R.E.¹, Djurašević, G.^{2,3}, Araya, I.^{4,5}, Curé, M.⁴

¹ *Departamento de Astronomía, Universidad de Concepción, Casilla 160-C, Concepción, Chile.*

² *Astronomical Observatory, Volgina 7, 11060 Belgrade 38, Serbia.*

³ *Isaac Newton Institute of Chile, Yugoslavia Branch.*

⁴ *Instituto de Física y Astronomía, Facultad de Ciencias, Universidad de Valparaíso, Chile.*

⁵ *Núcleo de Matemáticas, Física y Estadística, Facultad de Ciencias, Universidad Mayor, Chile.*

Published: Monthly Notices of the Royal Astronomical Society

5.1 Abstract

Double Periodic Variables (DPV) are among the new enigmas of semi-detached eclipsing binaries. These are intermediate-mass binaries characterized by a long photometric period lasting on average 33 times the orbital period. We present a spectroscopic and photometric study of the DPV V495 Cen based on new high-resolution spectra and the ASAS V-band light curve. We have determined an improved orbital period of 33.492 ± 0.002 d and a long period of 1283 d. We find a cool evolved star of $M_2 = 0.91 \pm 0.2M_\odot$, $T_2 = 6000 \pm 250K$ and $R_2 = 19.3 \pm 0.5R_\odot$ and a hot companion of $M_1 = 5.76 \pm 0.3M_\odot$, $T_1 = 16960 \pm 400K$ and $R = 4.5 \pm 0.2R_\odot$. The mid-type B dwarf is surrounded by a concave and geometrically thick disc, of radial extension $R_d = 40.2 \pm 1.3R_\odot$ contributing ~ 11 percent to the total luminosity of the system at the V band. The system is seen under inclination $84^\circ 8' \pm 0^\circ 6'$ and it is at a distance $d = 2092 \pm 104.6$ pc. The light curve analysis suggests that the mass transfer stream impacts the external edge of the disc forming a hot region 11% hotter than the surrounding disc material. The persistent $V < R$ asymmetry of the H α emission suggests the presence of a wind and the detection of a secondary absorption component in He I lines indicates a possible wind origin in the hotspot region.

5.2 Introduction

Double Periodic Variables are interacting binary stars of intermediate mass that show two closely linked photometric variations being the long period roughly 33 times longer than the orbital period (Mennickent et al., 2003, 2016; Mennickent, 2017; Poleski et al., 2010). The nature of the second period is unknown but suspected to reflect the strength variations of a wind generated in the stream-disc impact region (Mennickent et al., 2012, 2016; van Rensbergen et al., 2008). Also, DPVs are considered as one specific evolutionary step for more massive Algols, one possibly involving mild mass transfer and systemic mass loss (Mennickent et al., 2008). An interesting property of these objects is the surprising constancy of their orbital periods, which is not expected in Algols undergoing RLOF mass transfer (Garrido et al., 2013). Also the DPVs seem to be hotter and more massive than classical Algols and seem to have always a B-type component; their orbital periods typically run between 4 and 100 days. DPVs have been found in the Galaxy (MW), Large Magellanic Cloud (LMC) and the Small Magellanic Cloud (SMC). The components of DPVs are denoted by the suffixes g and d appended to the parameter designation, g denoting the primary component (C1) or gainer (hot) and d the secondary component (C2) or donor (cold), respectively. Recently, a mechanism based on cycles of a magnetic dynamo in the donor star, the so called Applegate mechanism, was proposed as an explanation for the DPV long cycles consistent with the almost constancy of the orbital period (Schleicher & Mennickent, 2017).

The importance of studying DPVs is the fact that they are interesting astrophysical objects for the study of mechanisms of mass transfer in semidetached binaries, they share similarities with some Algol systems, and can potentially provide us a wealth of information on the density, tidal friction, wind processes and stellar dynamos in massive close binaries (Deschamps et al., 2015; de Mink et al., 2014). Hitherto only a couple of DPVs, less than 5%, have been studied spectroscopically, e.g. (Mennickent et al., 2008, 2012; Barría et al., 2013, 2014; Garrido et al., 2013; Mennickent et al., 2015, 2016).

The eclipsing interacting binary V495 Cen (ASAS ID 130135-5605.5, $\alpha_{2000} = 13:01:35.0$, $\delta_{2000} = -56:05:30.0$, $V = 9.95$ mag, $B-V = 0.52$ mag, spectral type Be)¹ was discovered as a DPV by Mennickent & Rosales (2014), who find that the system is characterized by a long photometric cycle of 1283 d, resulting in the system with the longest period among Galactic DPVs. V 495 Cen has been poorly studied and shows an orbital period of 33.48177 d in the ASAS² catalogue (Pojmanski, 1997). Our study will contribute to the overall understanding of DPVs, especially those of long orbital period.

In Section 2 we present a photometric analysis of V495 Cen. In Section 3 we give a brief review of the methods of data acquisition and data reductions. In Section 4 we present the orbital and physical parameters of the system. In Section 5 we model the light curve with a special code including the light contribution of both stars and the accretion disc, and get luminosities, radii, temperatures, surface gravities, masses and the system's inclination. In Section 6 we present an analysis yielding the reddening and distance of the system. Finally, the main results of our research are summarized in Section 7.

5.3 Photometric ephemeris

We have re-analyzed the ASAS light curve considering only those 622 better quality data points labeled as A-type by ASAS (Fig. 5.1) and rejecting outliers points, contrary to the previous analysis (Mennickent & Rosales, 2014) in which were considered data points labeled as A-type and

¹<http://simbad.u-strasbg.fr/simbad>

²<http://www.astrouw.edu.pl/asas/>

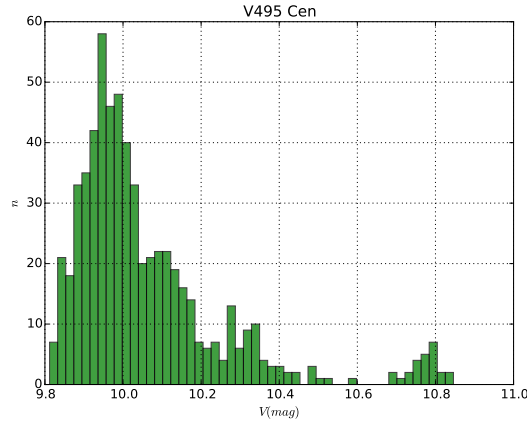


Figure 5.1: Histogram of magnitude for V495 Cen with 50 bins

B-type, the best and normal quality respectively. The data set was analyzed by Phase Dispersion Minimization (PDM-IRAF, Stellingwerf 1978)³, revealing an orbital period $P_o = 33.492 \pm 0.01613$ d (the error corresponds to the difference between the first approximation by PDM and the best value found by visual inspection of the periodogram minimum) and the epoch of minimum HJD = 2454609.71384 \pm 0.032 d. We have noticed that the orbital period shown in ASAS (33.4817 d) does not match the value obtained by us. This is probably due to the fact that the algorithm used by PDM to search for periods is different to that used by ASAS at the moment of carrying out the periodogram.

With the long and short periods we disentangled the light curve with a code specially designed for this purpose by Zbigniew Kołaczkowski. The code fits the data with a Fourier series consisting of fundamental frequencies and harmonics and removes them. As a result we obtain the cleaned light curve with no frequencies and two light curves for the isolated orbital and long cycles as shown in (Fig. 5.2). The process reveals an orbital modulation typical of an eclipsing binary type (EB), with rounded inter-eclipse regions revealing proximity effects, and a longer cycle characterized by a quasi-sinusoidal variability typical of Double Periodic Variables, whose full amplitude in the V-band is $\sim 20\%$ with respect to the total brightness. We determined the following ephemeris for the light curves:

$$HJD_{min,orbital} = 2454609.713(32) + 33.492(16) \times E, \quad (5.1)$$

$$HJD_{max,long} = 2454926.699(42) + 1283 \times E, \quad (5.2)$$

These are used for the spectroscopic analysis in the rest of the paper.

³IRAF is distributed by National Optical Astronomy Observatories, which are operated by Association of Universities for Research in Astronomy, Inc., under cooperative agreement with the National Science Foundation

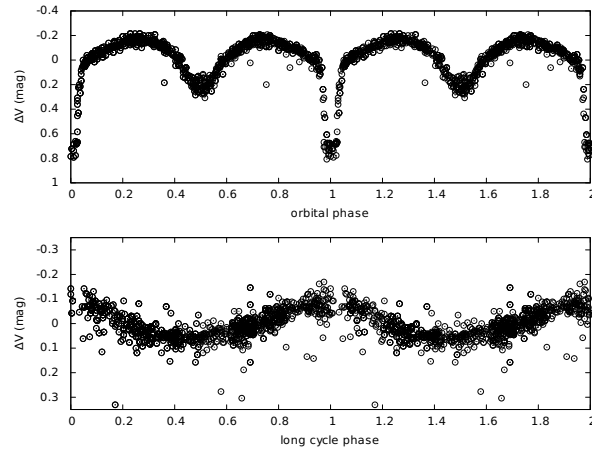


Figure 5.2: V495 Cen ASAS V-band light curve after disentangling. Orbital period (up) and long period (down). Phases were calculated according to times of light curve minimum and maxima, given by equation (1) and (2)

5.4 Spectroscopic observations

To investigate the fundamental properties of V495 Cen we collected a series of high-resolution optical spectra between February and May 2015 with the CHIRON⁴ spectrograph. We obtained 10 spectra with $R \sim 25000$ (fiber mode) and 30 spectra with $R \sim 25000$ (slicer mode). The spectral regions covered were 4500-8500 Å and 4580-8762 Å at the fiber and slicer mode, respectively, with a typical signal to noise ratio (SNR) of ≈ 160 .

The corrections with flat and bias, wavelength calibration and order merging were done with IRAF. We also normalized all spectra to the continuum and corrected them to the heliocentric rest frame.

The spectra obtained with CHIRON are not sky-subtracted. We have not flux calibrated our spectra but this does not affect the strength measurements and radial velocities included in this paper.

5.5 Spectroscopic analysis

5.5.1 Spectral disentangling

The spectra were disentangled with a method that is quite good for separating the absorption-lines widths of both stellar components (González & Levato, 2006). This method turns to be effective when working with absorption-lines widths less than the radial velocity amplitude of the corresponding star, i.e. for most lines except for the strong and wide $H\alpha$ emission. For this reason all spectral regions of interest except the $H\alpha$ region were disentangled. However, as we can see in Fig. 5.3, the underlying donor absorption is small compared with the strong double peak $H\alpha$ emission. The presence of emission in $H\alpha$ confirms the interacting binary nature for this system and suggests it is in a semi-detached stage and possesses a circumstellar disc. We notice the deep central

⁴<http://www.ctio.noao.edu/noao/content/CHIRON>

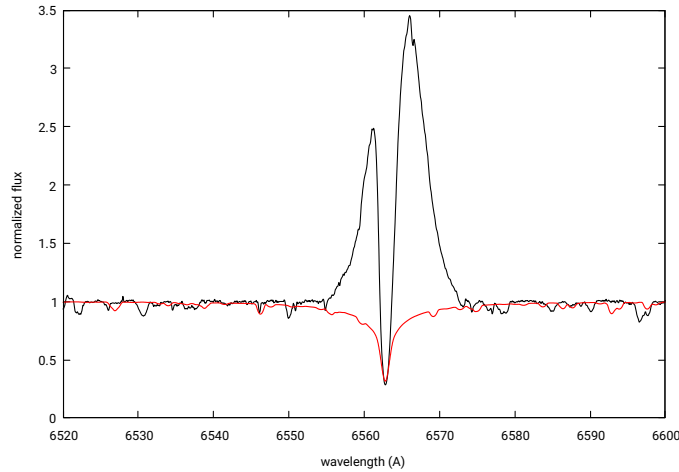


Figure 5.3: The H α line on HJD 2457062.80354576 ($\phi_o = 0.24, \phi_l = 0.68$) and the best synthetic spectrum for the donor.

absorption between the emission peaks revealing large amounts of obscuring material through the line of sight and also the larger intensity of the red peak at this specific epoch.

5.5.2 Determination of donor physical parameters

To determine the physical parameters of the secondary star, we compared our observed average donor spectrum with synthetic spectra constructed with SPECTRUM⁵ which uses atmospheric models computed with grids of ATLAS9⁶ model atmospheres (Castelli & Kurucz, 2004). The models used are in Local Thermodynamic Equilibrium (LTE).

The theoretical models were calculated for effective temperatures from 4250 to 19000 K with steps of 250 K, surface gravities from 0.5 to 3.5 dex with steps of 0.5 dex, solar metallicity, micro-turbulent velocity from 0.0 to 2.0 km s⁻¹ with steps of 1.0 km s⁻¹ and macro-turbulent velocity from 1.0 to 20.0 km s⁻¹ with steps of 1.0 km s⁻¹.

Our analysis aimed to find the best synthetic spectrum was based on a chi-square optimization algorithm. The method allowed simultaneous determination of various parameters involved with stellar spectra and consists of the minimization of the deviation between the theoretical normalized flux distribution and the observed normalized spectrum, the latter corrected by a veiling factor η . The synthetic spectrum depends on the stellar parameters, such as effective temperature T_{eff} , surface gravity $\log g$, rotational velocity $v \sin i$, micro-turbulence v_{mic} and macro-turbulence velocity v_{mac} . The optimization of the method converged successfully at $T_2 = 6000 \pm 250$ K, $\log g_2 = 2.5 \pm 0.5$, $v_{2r} \sin i = 26 \pm 1$ km s⁻¹, $v_{mic} = 0.0 \pm 0.5$ km s⁻¹, $v_{mac} = 11 \pm 0.5$ (Fig. 5.5). We observed a slow divergence of the method for higher temperatures and surface gravity.

5.5.3 Radial velocities for the donor

The radial velocity of the donor was measured by cross correlation of a spectral region plenty of metallic lines with a spectrum chosen as a template. Then the velocities were translated to the

⁵<http://www.appstate.edu/~grayro/spectrum/spectrum.html>

⁶<http://wwwuser.oats.inaf.it/castelli/grids.html>

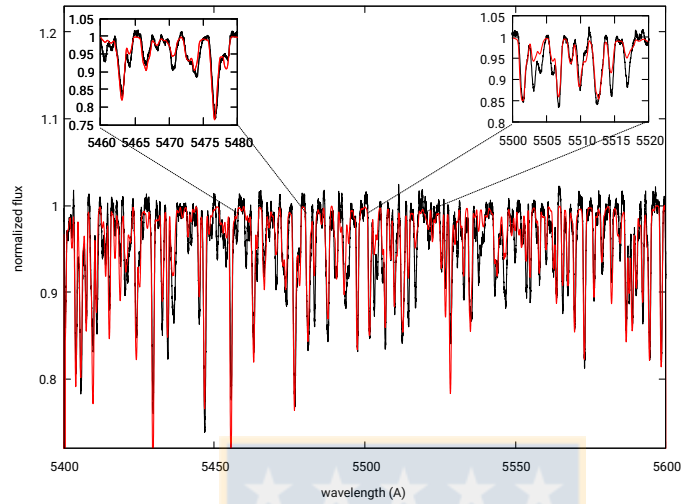


Figure 5.4: A detailed comparison between the observed and synthetic (best model: smoothed line in red colour) donor spectrum.

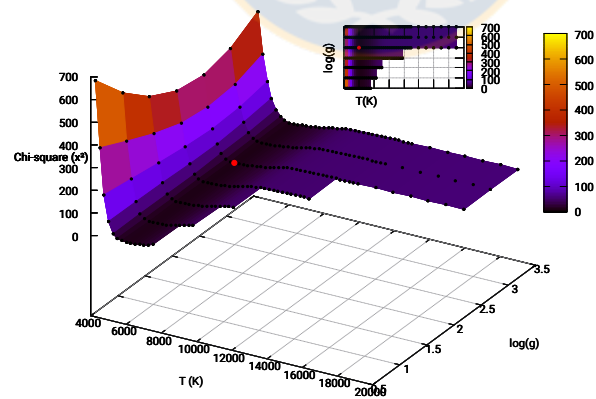


Figure 5.5: Colour map of χ^2 with two degrees of freedom and with all other parameters at their optimized values for donor star corresponding to value of $\Delta\chi^2 = 8.26$ from a total 12134 data.

absolute heliocentric system by adding the template velocity obtained by simple Gaussian fits to selected absorption lines. The donor velocities are given in Table 5.4.

To find the orbital elements of V495 Cen, we used the genetic algorithm PIKAIA ⁷ developed by Charbonneau (1995). The method consists in finding the set of orbital parameters that produces a series of theoretical velocities that minimize the function χ^2 , defined as:

$$\chi^2(P_o, \tau, \omega, e, K_2, \gamma) = \frac{1}{N-6} \sum_{j=1}^N \left(\frac{V_j^{obs} - V(t_j; P_o, \tau, \omega, e, K_2, \gamma)}{\sigma_j} \right)^2, \quad (5.3)$$

Where N is the number of observations, V_j^{obs} is the radial velocity observed in the data set, and $V(t_j; P_o, \tau, \omega, e, K_2, \gamma)$ is the radial velocity at time t_j given the parameters. P_o is the orbital period, ω the periastron longitude, τ the time of passage per the periastron, e the orbital eccentricity, K_2 the half-amplitude of the RV for the donor, and γ the velocity of the system centre of mass. The radial velocity is given by:

$$V(t) = \gamma + K_2(\cos(\omega + \theta(t)) + e\cos(\omega)), \quad (5.4)$$

(Hilditch (2001), eq. 2.45) where θ is the true anomaly obtained solving the following two equations involving the eccentric anomaly E :

$$\tan\left(\frac{\theta}{2}\right) = \sqrt{\frac{1+e}{1-e}} \tan\left(\frac{E}{2}\right), \quad (5.5)$$

$$E - e\sin(E) = \frac{2\pi}{P_o}(t - \tau), \quad (5.6)$$

(Hilditch (2001), eq. 2.35) To calculate this, we must first solve equation (6) for E , then solve Equation (5) for θ , and finally solve equation (4) for $V(t_j; P_o, \tau, w, e, K_2, \gamma)$. The error was estimated using Monte Carlo simulations, by perturbing the best-fitting solution obtained with PIKAIA and computing a χ^2 of these perturbed solutions. We note that our eccentricity solutions give a small value of $e = 0.007$. We have implemented a test for the significance of the eccentricity (Lucy & Sweeney, 1971). According to this test the condition $p_1 < 0.05$ means a significant ellipticity, where:

$$p_1 = \left(\frac{\sum(o - c)_{ecc}^2}{\sum(o - c)_{circ}^2} \right)^{(n-m)/2}, \quad (5.7)$$

where *ecc* indicates the residuals of an eccentric fit, and *circ* the residuals of a circular fit, n the total number of observations, m the number of free parameters in an eccentric fit. Finally p_1 is the probability of falsely rejecting the circular orbit. We obtained $p_1 = 0.0178$ which is in principle compatible with a very small ellipticity. However, the 1σ error still allows a circular orbit. The orbital parameters and errors are given in Table 5.1 and the best fit to the radial velocities is shown in Fig. 5.6.

⁷<http://www.hao.ucar.edu/modeling/pikaia/pikaia.php>

Table 5.1: Orbital elements for the donor of V495 Cen obtained through minimization of χ^2 given by equation (1). The value $\tau^* = \tau - 2450000$ is given and the maximum and minimum are one isophote 1σ

Parameter	Best value	Low limit	Upper limit
$P_o(d)$	33.48100	33.35620	33.60620
τ^*	105.12600	105.02200	105.23000
e	0.00733	0.00000	0.02600
$\omega(rad)$	1.68911	1.67044	1.70844
$K_2(kms^{-1})$	106.88000	105.19200	108.49200
$\gamma(kms^{-1})$	-0.75273	-2.12456	0.61544

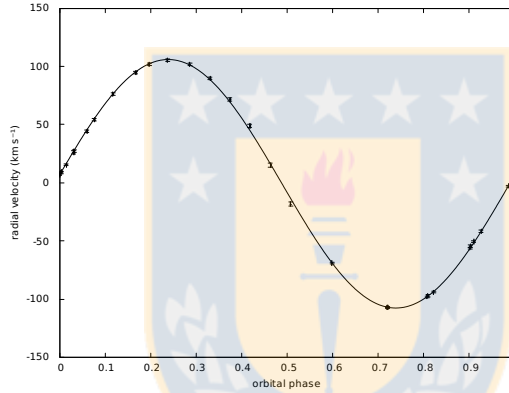


Figure 5.6: The radial velocities of the donor obtained by cross correlation of a region plenty of metallic lines and the best fit, given for Eq. 4.

The secondary star dominates the metallic and Balmer line spectrum. It was quite difficult to find lines from the gainer. However, we found a little group of characteristic lines that represents the movement of the gainer star and we choose to use the most characteristic lines for a star of B spectral type, these were found as components of the He I 5015 and He I 5875 lines (Fig. 5.7), as also happened in the DPV HD 170582 (Mennickent et al. (2015)). It should be noticed that in HD 170582 the origin of the anomalous He I component is placed near the hotspot region, consistent with a hotspot wind. The radial velocities for the C1 component (gainer) of the He I 5015 line and the C2 component (donor) of the He I 5875 line were measured with a gaussian fit and are shown in Fig. 5.8, along with fits for both orbits. We observe that the technique of gaussian fit provides velocities with a larger scatter than those obtained with the cross correlation method.

The RV of the component C1 for He I 5015 is fitted with a sine function of amplitude 16.92 ± 0.84 km s^{-1} and zero point 0.00 ± 0.58 km s^{-1} . It moves in opposition to the donor and it could reflect the motion of the gainer around the binary center of mass. The RV of the component C2 of He I 5875 was fitted with a sine of amplitude 106.80 ± 0.39 km s^{-1} and zero point -0.91 ± 0.28 km s^{-1} , both solutions assume a circular orbit (Fig. 5.8). The reason for which the radial velocity curve of the component C1 has a small phase lag might be due to the brightness contribution of the disc in the absorption line.

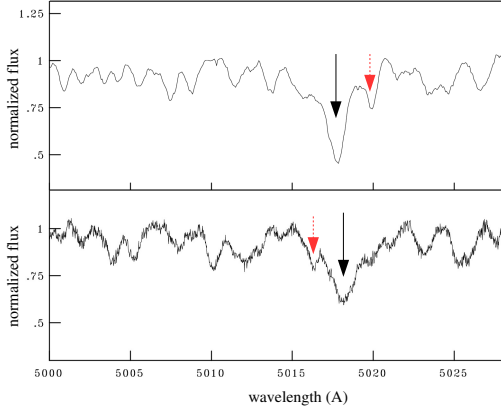


Figure 5.7: He I 5015 for HJD 2457062.78265893 ($\Phi_o = 0.24$, $\Phi_l = 0.68$, up) and for HJD 2457078.7407534 ($\Phi_o = 0.72$, $\Phi_l = 0.70$, below). The dotted (red) arrow indicates the donor star component while the solid (black) arrow indicates the component attributed to the gainer.

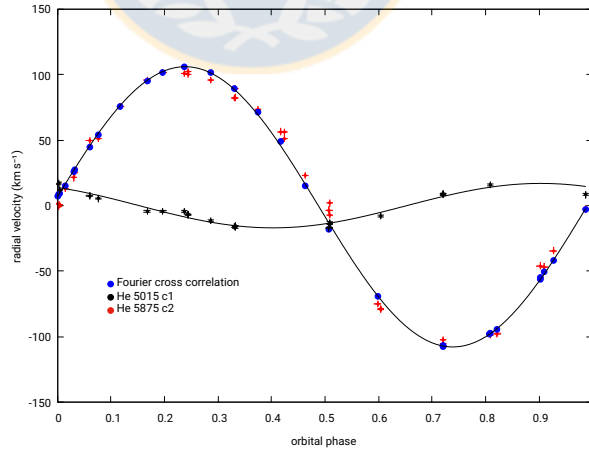


Figure 5.8: Radial velocities of the He I 5015 C1 component and He I 5875 C2 component measured by gaussian fits. For comparison we show the velocities measured with the cross correlation method, applied to a region plenty of metallic lines (red dots). The best fits are shown for both orbits.

5.5.4 The H α emission line profile

An important result of our spectroscopic analysis is that the H α profile shows a double peak emission with the red peak always of larger intensity than the blue one while the central absorption does not follow the motion of none of the stellar components (Fig. 5.9). Representative H α profiles at some epochs and intensity/width measurements performed at the mean profile are shown in Fig. 5.10. The full width of the line at the level of the continuum is 776 km s^{-1} .

The double emission and the deep absorption core is typical of a disk seen at large inclination, however the persistence of the larger red peak is not usual. In binaries with accretion discs, it is normal to find variations of the relative intensities of the emission peaks. This is quantified with the parameter V/R usually defined as $V/R = (I_v - 1)/(I_r - 1)$, i.e. in terms of the peak intensities relative to the normalized continuum. Due to bright zones in the disc of Algols this ratio tends to vary cyclically with the orbital period. However, in V495 Cen we observe almost always $V < R$. This can be interpreted as evidence of material escaping from the system, i.e. a wind emerging probably from the hotspot region. We also notice here that the strength of the H α emission is large compared with other cases of DPVs. The equivalent width (EW) of the H α line shows a clear periodic behavior and varies with the orbital period. A least square fit of sine type, with the orbital period fixed at $1.0 P_o$ (solid line in Fig. 5.11), represents the observed data quite well, and shows a mean EW of $9.517 \pm 0.063 \text{ \AA}$ and an amplitude of $1.985 \pm 0.663 \text{ \AA}$. The phase of observations is such that the minima occur at orbital phase 0.15. A probable interpretation is that there is an asymmetric distribution of H α emission on the surface of the star or material escaping from the hotspot, which is assumed to be synchronously rotating. Also we note the spectral resolution difference for each equivalent width obtained by fiber mode ($R \sim 25000$, blue dots) and slicer mode ($R \sim 80000$, black dots).

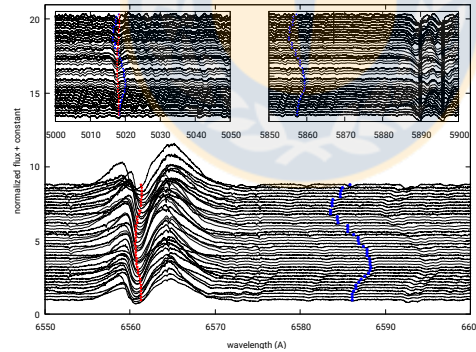


Figure 5.9: The behavior of H α line sorted by phases. The radial velocities were overlaid in each spectrum to compare with the movement of the donor (blue dots) and gainer (red triangles).

5.5.5 Gainer, mass ratio and circumstellar matter

In some spectroscopic binaries stars, spectral lines from both stars are visible and the lines are alternately double or single. These systems are known as double-lined spectroscopic binaries, denoted as SB2. But in other systems, the spectrum of only one component is seen and the lines in the spectrum shift periodically towards the blue and red. Such stars are known as single-lined spectroscopic binaries or SB1. V495 Cen is probably an SB2 system and we have assumed that the velocity obtained from the C1 HeI 5015 line represents the gainer orbital motion hence we have

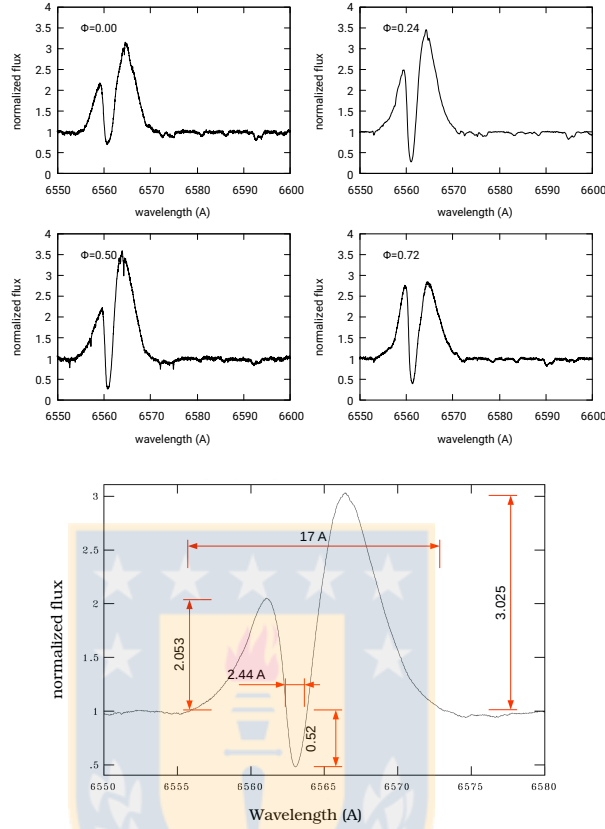


Figure 5.10: (Left) Variation of the H α profile at different orbital phases. (Right) H α profile average with representative sizes. The width of the absorption was measured at the height of the continuum but was raised to facilitate the visibility of the data.

inferred a mass ratio $q = 0.158 \pm 0.008$.

Now let's investigate if this value is compatible with synchronous rotation for the secondary star filling the Roche lobe; we use the following equation valid for semi detached binaries:

$$\frac{v_{rot} \sin i}{K} \approx (1 + q) \frac{0.49q^{2/3}}{0.6q^{2/3} + \ln(1 + q^{1/3})}, \quad (5.8)$$

(Eggleton (2006), eq. 3.5 and 3.9). Therefore with $K_2 = 106.880 \text{ km s}^{-1}$ and $v_{rot2} \sin i = 26 \text{ km s}^{-1}$ with their respective errors and considering the 1% of accuracy of equation 8, we get $q = 0.119 \pm 0.037$, which is very close to the q value derived from the RV half-amplitude of the helium components (Fig. 5.12); therefore we can say that the 5015 HeI line comes from the gainer star. Since synchronism is expected for such a short orbital period binary due to the influence of dynamical tides (Zahn, 1975, 1977), from now on we assume the donor rotating synchronously.

Another important point is the relation between the mean density $\bar{\rho}$ (in solar units) of a star that just fills its Roche lobe and the effective radius R_L (Eggleton, 1983) we quantified as the product between the critical orbital period (days) and mean density (g cm^{-3}) as:

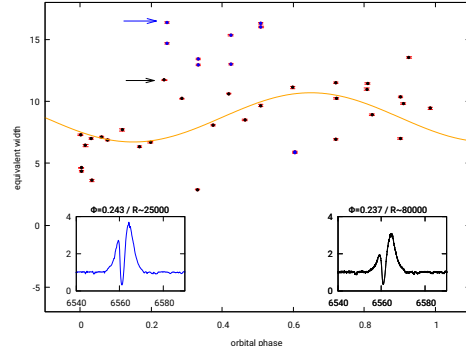


Figure 5.11: The equivalent width of the H α emission line as a function of the orbital phase. Black dots correspond to spectra obtained with slicer mode, while the blue dots are spectra obtained in fiber mode.

$$P_{cr} \sqrt{\bar{\rho}} = \left(\frac{3\pi}{G} \right)^{1/2} \left(\frac{q}{1+q} \right)^{1/2} x_L^{-3/2}, \quad (5.9)$$

where x_L is in units of the orbital separation. Assuming $q = 0.158$ from the above RV study, we have obtained the ratio between the effective radius and the orbital separation $R_L/a = 0.236 \pm 0.155$ (Eggleton (2006), eq. 3.5), and estimated the critical period $P_{cr} \sqrt{\bar{\rho}} = 0.44 \pm 0.06$, which is the shortest period possible for a binary of given mass ratio into which a star of given mean density $\bar{\rho}$ can be fitted without overflowing its Roche lobe (Eggleton (1983), eq. 3). Both values are significant figures to understand the evolution of the Double Periodic Variable V495 Cen.

5.5.6 Mass constraints from spectroscopy

The mass function represents the minimum possible mass for the unseen star, for a system with unknown orbital inclination i and elliptical orbit, it may be expressed as:

$$f = 1.0361 \times 10^{-7} (1 - e^2)^{3/2} \left(\frac{K_2}{\text{kms}^{-1}} \right)^3 \frac{P_o}{\text{day}} M_{\odot}, \quad (5.10)$$

(Hilditch (2001), eq. 2.53) Using $q = 0.158$ (donor rotating synchronously) and an elliptical orbit with $e = 0.007$ from the above RV study, we obtained a mass function $f = 4.235 \pm 0.015 M_{\odot}$. Assuming an orbital inclination $i = 84.8$ (see the next section), the respective masses are $M_d = 0.911 \pm 0.420 M_{\odot}$ and $M_g = 5.753 \pm 0.451 M_{\odot}$. These are preliminary results. Both are compatible with results obtained, independently, through LC analysis in the next section.

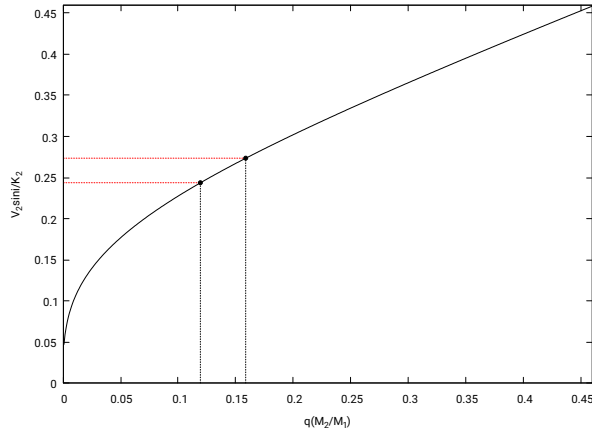


Figure 5.12: The solid line is given by equation 8 and the dashed lines show the synchronous ($q = 0.158$) and the observed (sub-synchronous, $q = 0.119$) cases.

5.6 Light-curve model and system parameters

5.6.1 The fitting procedure

We find the main physical parameters for the stellar components fitting the V-band light curve with the aid of an inverse-problem solving method based in the algorithm developed by Djurašević (1992, 1996). We have assumed a semi-detached system with the donor filling the Roche lobe, and we adopted a configuration that included an optically thick accretion disc around the gainer star.

Our model considers a hot spot located on the edge side of the disc, and it is described by the ratio of the hot spot temperature and the unperturbed local temperature of the disc, the angular dimension and longitude (in arc degrees). Synchronous rotation is assumed for both stellar components. The model used follows results of hydrodynamical simulation of gas dynamics in interacting close binary stars by Bisikalo et al. (1998, 1999, 2003) and has been tested in studies of DPVs, e.g. (Mennickent et al., 2012; Barría et al., 2013; Mennickent et al., 2015).

We fixed $q = 0.158$ and $T_c = 6000K$ based on the spectroscopic study previously presented. In addition, we set the gravity darkening exponent and the albedo of the gainer to $\beta_h = 0.25$ and $A_h = 1.0$ in accordance with von Zeipel's law for radiative shells and complete re-radiation; for the donor we set $\beta_c = 0.08$ and $A_c = 0.5$, as is appropriate for stars with convective envelopes according to Lucy (1967), Rafert & Twigg (1980), Ruciński (1969).

5.6.2 The best light-curve model

The best fit model for V495 Cen contains an optically and geometrically thick disc around the gainer star; the stellar, orbital and disc parameters are given in Table 5.2.

The system inclination angle is $i = 84^\circ.8 \pm 0.6$ and the disc radius $R_d = 40.2 \pm 1.3R_\odot$,

Table 5.2: Results of the analysis of the V-band light-curve of V495 Cen obtained by solving the inverse problem for the Roche model with an accretion disc around the more-massive (hotter) gainer in the synchronous rotation regime.

Quantity		Quantity	
n	617	$\mathcal{M}_h[\mathcal{M}_\odot]$	5.76 ± 0.3
$\Sigma(\text{O} - \text{C})^2$	0.5751	$\mathcal{M}_c[\mathcal{M}_\odot]$	0.91 ± 0.2
σ_{rms}	0.0306	$\mathcal{R}_h[\text{R}_\odot]$	4.5 ± 0.2
$i[^\circ]$	84.8 ± 0.6	$\mathcal{R}_c[\text{R}_\odot]$	19.3 ± 0.5
F_d	0.88 ± 0.03	$\log g_h$	3.89 ± 0.02
$T_d[\text{K}]$	4040 ± 250	$\log g_c$	1.83 ± 0.02
$d_e[a_{\text{orb}}]$	0.046 ± 0.016	M_{bol}^h	-3.16 ± 0.1
$d_c[a_{\text{orb}}]$	0.007 ± 0.009	M_{bol}^c	-1.80 ± 0.1
a_T	4.1 ± 0.3	$a_{\text{orb}}[\text{R}_\odot]$	82.8 ± 0.3
f_h	1.00	$\mathcal{R}_d[\text{R}_\odot]$	40.2 ± 1.3
F_h	0.109 ± 0.014	$d_e[\text{R}_\odot]$	3.8 ± 0.2
$T_h[\text{K}]$	16960 ± 400	$d_c[\text{R}_\odot]$	0.6 ± 0.2
$A_{\text{hs}} = T_{\text{hs}}/T_d$	1.11 ± 0.05		
$\theta_{\text{hs}}[^\circ]$	18.2 ± 2.0		
$\lambda_{\text{hs}}[^\circ]$	338.3 ± 9.0		
$\theta_{\text{rad}}[^\circ]$	-15.4 ± 13.6		
Ω_h	18.36 ± 0.02		
Ω_c	2.125 ± 0.05		

Note: Fixed Parameters: $q = \mathcal{M}_c/\mathcal{M}_h = 0.158$ - mass ratio of the components, $T_c = 6000\text{K}$ - temperature of the less-massive (cooler) donor, $F_c = 1.0$ - filling factor for the critical Roche lobe of the donor, $f_{h,c} = 1.00$ - non-synchronous rotation coefficients of the system components, $\beta_h = 0.25$, $\beta_c = 0.08$ - gravity-darkening coefficients of the components, $A_h = 1.0, A_c = 0.5$ - albedo coefficients of the components.

Note: n - number of observations, $\Sigma(\text{O} - \text{C})^2$ - final sum of squares of residuals between observed (LCO) and synthetic (LCC) light-curves, σ_{rms} - root-mean-square of the residuals, i - orbit inclination (in arc degrees), $F_d = R_d/R_{\text{vc}}$ - disk dimension factor (the ratio of the disk radius to the critical Roche lobe radius along y-axis), T_d - disk-edge temperature, d_e , d_c , - disk thicknesses (at the edge and at the center of the disk, respectively) in the units of the distance between the components, a_T - disk temperature distribution coefficient, f_h - non-synchronous rotation coefficient of the more massive gainer (in the synchronous rotation regime), $F_h = R_h/R_{zc}$ - filling factor for the critical Roche lobe of the hotter, more-massive gainer (ratio of the stellar polar radius to the critical Roche lobe radius along z-axis for a star in synchronous rotation regime), T_h - temperature of the gainer, $A_{\text{hs,bs}} = T_{\text{hs,bs}}/T_d$ - hot spot temperature coefficients, θ_{hs} and λ_{hs} - spot angular dimension and longitude (in arc degrees), θ_{rad} - angle between the line perpendicular to the local disk edge surface and the direction of the hot-spot maximum radiation, $\Omega_{h,c}$ - dimensionless surface potentials of the hotter gainer and cooler donor, $\mathcal{M}_{h,c}[\mathcal{M}_\odot]$, $\mathcal{R}_{h,c}[\text{R}_\odot]$ - stellar masses and mean radii of stars in solar units, $\log g_{h,c}$ - logarithm (base 10) of the system components effective gravity, $M_{\text{bol}}^{h,c}$ - absolute stellar bolometric magnitudes, $a_{\text{orb}}[\text{R}_\odot]$, $\mathcal{R}_d[\text{R}_\odot]$, $d_e[\text{R}_\odot]$, $d_c[\text{R}_\odot]$ - orbital semi-major axis, disk radius and disk thicknesses at its edge and center, respectively, given in solar units.

which is 9 times larger than the radius of the main star $R_h = 4.5$. The disc has central vertical thickness $d_c = 0.6R_\odot$ and edge thickness $d_e = 3.8R_\odot$, i.e. it has a concave form. The temperature of the disc increases from $T_d = 4040$ K at the outer edge to $T_h = 16960$ K at the inner edge where it is in thermal and physical contact with the gainer. The surface gravity of the secondary component (donor) is $\log g_c = 1.83 \pm 0.1$ i.e. almost 1σ below the spectroscopic value 2.5 ± 0.5 . The temperature of the hotspot is $T_{hs} \approx 4484$ K i.e. is 11 percent higher than the disc edge temperature.

The light curve and the fit, the O-C curve, residuals, and the individual flux contributions of the donor, disc and the gainer, are shown in Fig. 5.13. Also we show a view of the model at orbital phases 0.05, 0.55 and 0.80.

The obtained solution can be treated as unique with a model of the system with fixed initial parameters (mass ratio and temperature of the donor). The uniqueness of the obtained optimal solution is checked by the solving the inverse problem of the light curve interpretation by applying the Simplex algorithm. Even, if we vary the initial system parameters in the initial simplex in the interval of 5-10% of the optimal solution, the optimization process converges to the obtained solution within a given errors bars. Of course, if the initial fixed parameters are used with a larger uncertainty, the estimated errors bars of the free model parameters increase too.

5.7 Reddening, distance and spectral energy distribution

5.7.1 Distance determination

In order to determine the distance to the system we have applied a standard method based on the distance modulus to both binary components observed in the V band (Clausen, 2004):

$$(m_{d,g} - M_{d,g})_0 = 5 \log(R_{d,g}/R_\odot) + (m_{d,g} - A_V) - M_{bol\odot} + 10 \log(T_{d,g}/T_\odot) + BC_{d,g}, \quad (5.11)$$

where A_V is interstellar absorption and BC the bolometric correction; the apparent magnitudes, radii and effective temperatures of gainer and donor are represented with sub-indexes g and d , respectively.

Maps of Galactic dust and extinction in the region of V495 Cen are available on-line and give $E(B - V)_{S\&F} = 0.2820 \pm 0.0069$ (Schlafly & Finkbeiner (2011)) and $E(B - V)_{SFD} = 0.3279 \pm 0.0080$ (Schlegel et al. (1998)). Assuming a visual extinction to reddening ratio $A_V/E(B - V) = 3.1$ we get $A_{V_{S\&F}} = 0.8460 \pm 0.006$ and $A_{V_{SFD}} = 0.9837 \pm 0.008$, where we preferred the most recent determination of the reddening in the direction of the target.

The model of the V -band light curve (Fig. 5.13) shows that the flux of the system at the V band at quadratures $\phi_o = 0.25$ and $\phi_o = 0.75$ is $f_t = 1.77 \pm 0.05$ while the individual flux contribution of the donor is $f_d = 1.0 \pm 0.05$, of the gainer is $f_g = 0.57 \pm 0.05$ and the disc is $f_{disc} = 0.2 \pm 0.05$. This means that at quadrature the donor, gainer and disc contribute 57, 32 and 11 % to the total flux at the V band, respectively.

The apparent magnitude of the donor and gainer are derived from:

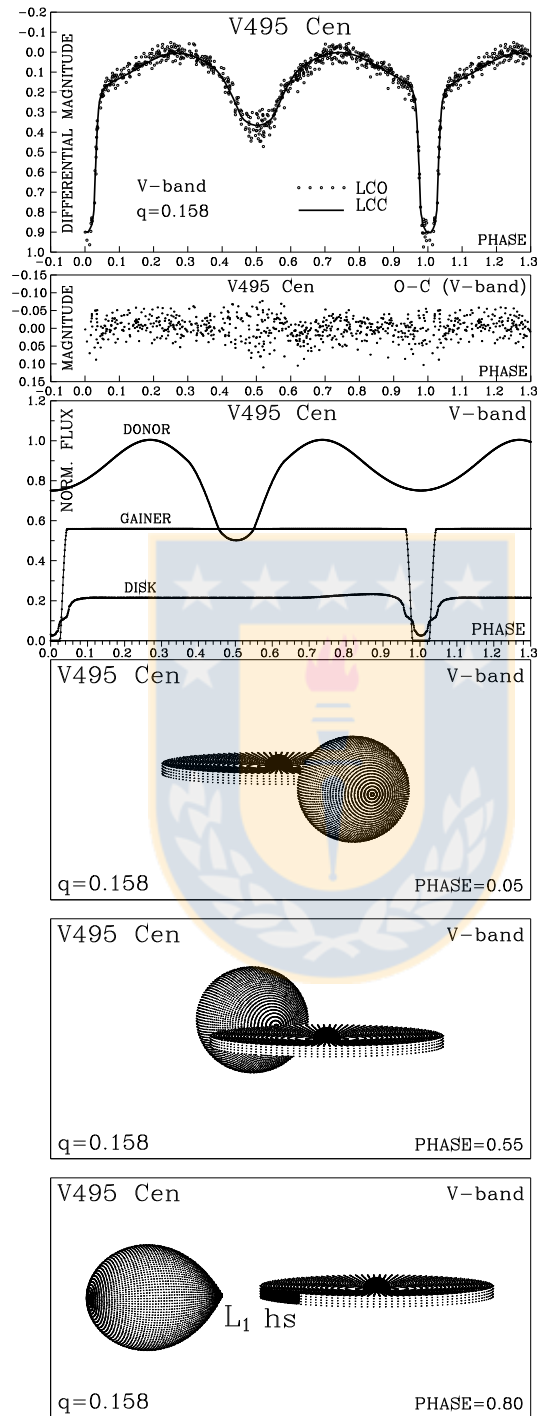


Figure 5.13: From top to bottom we show the observed (LCO) and synthetic (LCC) light-curves of V495 Cen obtained by analyzing photometric observations, final O-C residuals between the observed and optimum synthetic light curves, flux of donor, gainer and of the accretion disc, normalized to the donor flux at phase 0.25. The views of the optimal model at orbital phases 0.05, 0.50 and 0.80 obtained with parameters estimated by the light curve analysis.

$$m_d - m_t = -2.5 \log \left(\frac{f_d}{f_t} \right), \quad (5.12)$$

Considering that the observed apparent magnitude of the system is $m_t(V) = 9.95 \pm 0.03$, and the flux fractions given above, we find $m_d = 10.569 \pm 0.044$ mag and $m_g = 11.180 \pm 0.037$ mag.

The bolometric corrections were taken from Flower (1996) and the solar bolometric magnitude was taken from Torres (2010). We use $\log T_d = 3.778 \pm 0.042$ and $BC_d = -0.045 \pm 0.110$ for the donor and $\log T_g = 4.229 \pm 0.024$ and $BC_g = -1.525 \pm 0.079$ for the gainer, and the individual distances are $d_d = 1923.092 \pm 137.538$ pc $d_g = 2401.043 \pm 187.169$ pc. The difference in the distance for donor and gainer can be interpreted as an estimate of the intrinsic error of the method due to the gainer star is hidden by the disc, causing an extra reddening that is not the same reddening caused by the total absorption across the line of sight to V495 Cen. Therefore we have averaged the values obtaining for the system distance:

$$d(\text{pc}) = 2162.068 \pm 324.707 \text{ pc}, \quad (5.13)$$

Since the maximum absorption through the galactic gas column along the system line of sight has been considered for this calculation, this distance must be considered as a lower limit only.

5.7.2 Position in the H-R Diagram

From the above sections it is clear that the less massive star is the more evolved star of the binary pair, as usual in Algol systems. This can be explained by the mass transfer that has inverted the system mass ratio in such a way that the less massive star started as the more massive one some time ago and evolved first until filling its Roche lobe just before start mass transfer onto the now more massive stellar component.

In order to study the position of V 495 Cen in the luminosity-temperature diagram, we have chosen as comparison models based on a grid that is part of the large database of Geneva stellar models⁸. We consider single star models with metallicity $Z = 0.014$ (Ekström et al., 2012) as a first approximation to understand the evolutionary stage of V495 Cen (Fig. 5.14).

We observe that the gainer ($5.76 M_\odot$) is located outside the main sequence, showing a luminosity similar to a single star of that mass. It is located near the start of the stellar contraction stage for the evolutionary track of $6.0 M_\odot$. The core fractions of hydrogen and helium are 0.72 and 0.266, respectively. On the other hand, the donor ($0.91 M_\odot$) has a huge luminosity compared with a star of similar mass and fits the evolutionary track of a $4.35 M_\odot$ single star in the phase of hydrogen shell narrowing (Iben 1967, Fig.14). The high luminosity donor can be understood in terms of an evolved giant filling its Roche lobe that has transferred part of its mass onto the gainer forming the accretion disc.

⁸<https://obswww.unige.ch/Recherche/evoldb/index/>

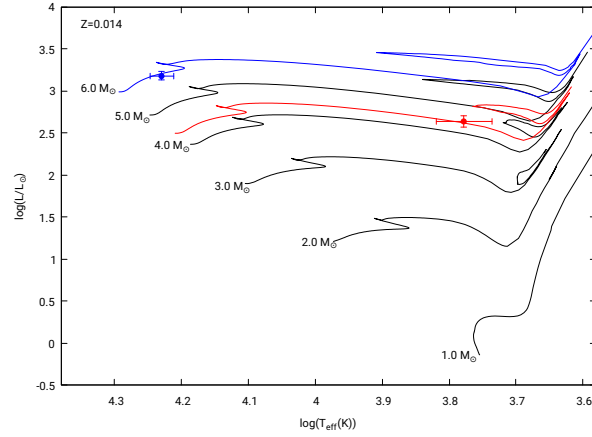


Figure 5.14: Hertzsprung-Russell diagram of evolutionary track for non-rotating single stars models (Ekström et al., 2012). The blue line corresponds to $6.0M_{\odot}$ while the red line to $4.35M_{\odot}$. Lines represent stellar tracks without rotation calculated at $Z= 0.014$.

Also we have inferred the color of each star as function of effective temperature (Torres, 2010). $(B - V)_{og} = -0.200 \pm 0.001$, $(B - V)_{od} = 0.571 \pm 0.001$ and compared the intrinsic color of both obtaining the spectral classes of each star. Hence, considering all above we find that the gainer is an early B3 V type, and the donor corresponds to late F9 IV, based on the intrinsic color analysis (Fitzgerald, 1970).

5.7.3 Spectral Energy Distribution (SED)

The determination of the physical parameters of astronomical objects from observational data is frequently linked with the use of theoretical models as templates. In order to obtain the broad-band photometric fluxes we compiled all the information available for V495 Cen and built the SEDs with the aid of the Spanish Virtual Observatory SED Analyzer⁹ (Bayo et al., 2008)) We performed a statistical test to decide which synthetic model best reproduces the observed data. The provided “best” fitting model is the one that minimizes the value of reduced χ^2 , considering the composite flux as:

$$f_{\lambda} = f_{\lambda,0} 10^{-0.4E(B-V)[k(\lambda-V)+R(V)]}, \quad (5.14)$$

where

$$f_{\lambda,0} = \left(\frac{R_2}{d}\right)^2 \left[\left(\frac{R_1}{R_2}\right)^2 f_{1,\lambda} + f_{2,\lambda} \right], \quad (5.15)$$

⁹<http://svo2.cab.inta-csic.es/theory/vosa4/>

and f_1 and f_2 are the fluxes of the star and secondary star respectively, $R(V) \equiv A(\lambda)/E(B - V)$ is the ratio of reddening to extinction at V , d is the distance to the system and R_1/R_2 is the ratio of the primary star radius to the secondary star radius, $k(\lambda - V) \equiv E(\lambda - V)/E(B - V)$ is the normalized extinction curve and was calculated in two steps:

$$k = \begin{cases} \varepsilon\lambda^{-\beta} - R_v & \text{if } x < 0.3 \\ R_v \left(a(x) + \frac{b(x)}{R_v} - 1 \right) & \text{if } 0.3 \leq x \leq 8.0 \end{cases} \quad (5.16)$$

Where $x \equiv 1/\lambda(\mu m^{-1})$, $\varepsilon = 1.19$, $\beta = 1.84$ and $R_v = 3.05$, with formal errors of about 1% (Martin & Whittet, 1990), however, this value of β is not applicable at wavelengths beyond $5 \mu m$. The parameters $a(x)$ and $b(x)$ are the parametrization coefficients for the extinction law from Cardelli et al. (1989).

The theoretical spectra were taken from the library of ATLAS9 Kurucz ODFNEW/NOVER models. We used fluxes calculated with metallicity index $[M/H] = 0.0$, the micro turbulence velocity for both stars was of 0.0 km s^{-1} . We considered the reddening produced by galactic dust as discussed in Section 3.1. The parametric space of the models was reduced to consider: donor temperature between 4250 and 8000 K with step of 250 K and surface gravity between 0.5 and 3.0 with steps 0.5, gainer temperature between 16000 and 17000 K with step of 1000 K and surface gravity between 3.5 and 4.5 with step of 0.5. We fixed the radii and considered all values of the photometry obtained with VOSA from 4280 Å until 220883 Å.

We implemented a chi-square adjustment considering a distance with a 5% error, for 7 degrees of freedom, i.e. $\chi^2_{critic0.95,7}$. We found a distance of $d = 2092 \text{ pc}$ with a $\chi^2 = 1.447$. Due to $\chi^2 < \chi^2_{critic0.95,7}$, then the solution is accepted and the solution obtained in Section 6.1 is consistent with the current results (Fig. 5.15).

In addition, we observe a slight infrared excess at wavelengths longer than 10000 Å, which cannot come from the main star itself but from cooler emitting material. This excess is probably formed in the same circumstellar material responsible of the strong $H\alpha$ line emission.

5.8 Conclusions

In this work we have presented a detailed spectroscopic and photometric analysis of V 495 Cen, the hitherto longest orbital period Galactic DPV. We conclude:

- From the photometric study we have determined that V495 shows an orbital period of $P_o = 33.492 \pm 0.002 \text{ d}$ and a long period of $P_l = 1283 \text{ d}$.
- We have modeled the spectrum and light curve and the best system and orbital parameters we found are given in Table 5.2. For instance, we determined the mass of

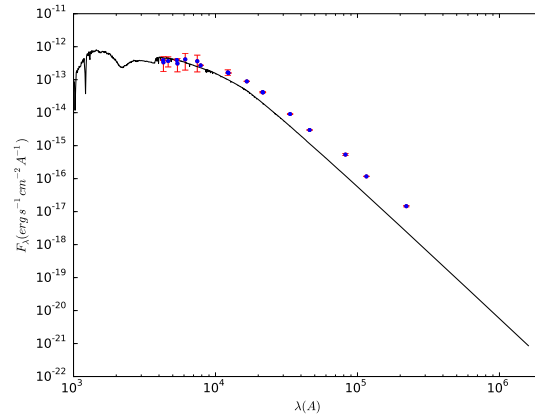


Figure 5.15: The best fit to the spectral energy distribution (SED) considers a two-star composite spectrum; it reproduces well the bluer part but exhibits a significant excess from the near-infrared that is probably formed in the circumstellar material. The black and orange theoretical spectrum is given by equation 14.

the secondary star $M_2 = 0.91 \pm 0.2 M_{\odot}$, its temperature $T_2 = 6000 \pm 250$ K and radius $R_2 = 19.3 \pm 0.5$, the mass of the primary $M_1 = 5.76 \pm 0.3 M_{\odot}$, its the temperature $T_1 = 16960 \pm 400$ K and radius $R_1 = 4.5 \pm 0.2 R_{\odot}$.

- The early B type dwarf is surrounded by an optical and geometrically thick accretion disc of radial extension $R_d = 40.2 \pm 1.3 R_{\odot}$.
- At quadratures the donor, gainer and disc contribute 57, 32 and 11% to the total flux at the V band, respectively.
- The best model shows a hot spot located in the outer edge of the disc, 11% hotter than the surrounding disc and displaced 18.2 degree for the line joining the star centers in the direction of the orbital motion.
- The spectral energy distribution shows infrared excess indicating the presence of a circumstellar material.
- We found a lower limit to the distance to V495 Cen of 2092 pc with a $\chi^2 = 1.447$ for 7 degrees of freedom and 95% of confidence level, i.e. the distance for V495 Cen is 2092 ± 104.6 pc.

Table 5.3: Summary of spectroscopic observation. N is number of spectra. The HJD at mid-exposure for the first spectrum series is given, Φ_o and Φ_l refer to the orbital and long-cycle phase, respectively, and are calculated according to Eq. 1 and Eq. 2. Spectral Resolution $R \sim 80000$ (with image slicer) and $R \sim 25000$ (fiber mode).

UT-date	Observatory/Telescope	Instrument	N	exptime (s)	HJD	Φ_o	Φ_l	S/N	R
2015-02-09	CTIO/1.5m	CHIRON	1	1800	2457062.78265893	0.2438536557	0.6899319243	214.11	25000
2015-02-09	CTIO/1.5m	CHIRON	1	1800	2457062.80354576	0.2444773294	0.6899482040	133.13	25000
2015-02-12	CTIO/1.5m	CHIRON	1	1800	2457065.73864590	0.3321184204	0.6922358892	172.66	25000
2015-02-12	CTIO/1.5m	CHIRON	1	1800	2457065.75953170	0.3327420633	0.6922521681	139.00	25000
2015-02-15	CTIO/1.5m	CHIRON	1	1800	2457068.81094574	0.4238562478	0.6946305111	114.24	25000
2015-02-15	CTIO/1.5m	CHIRON	1	1800	2457068.83183151	0.4244798898	0.6946467900	137.29	25000
2015-02-18	CTIO/1.5m	CHIRON	1	1800	2457071.65142447	0.5086719758	0.6968444462	229.02	25000
2015-02-18	CTIO/1.5m	CHIRON	1	1800	2457071.67231145	0.5092956539	0.6968607260	107.85	25000
2015-02-21	CTIO/1.5m	CHIRON	1	1800	2457074.85684834	0.6043848414	0.6993428280	116.52	25000
2015-02-21	CTIO/1.5m	CHIRON	1	1800	2457074.85684834	0.6043848414	0.6993428280	113.69	25000
2015-02-25	CTIO/1.5m	CHIRON	1	1800	2457078.74075340	0.7203569245	0.7023700338	79.80	80000
2015-02-25	CTIO/1.5m	CHIRON	1	1800	2457078.76179291	0.7209851571	0.7023864325	74.70	80000
2015-02-28	CTIO/1.5m	CHIRON	1	1200	2457081.64889093	0.8071929212	0.7046367038	41.35	80000
2015-03-03	CTIO/1.5m	CHIRON	1	1200	2457084.80281535	0.9013680308	0.7070949457	54.36	80000
2015-03-06	CTIO/1.5m	CHIRON	1	1200	2457087.65572745	0.9865550149	0.7093185717	49.53	80000
2015-03-09	CTIO/1.5m	CHIRON	1	1200	2457090.67030988	0.0765694201	0.7116682072	57.18	80000
2015-03-12	CTIO/1.5m	CHIRON	1	1200	2457093.71585473	0.1675083526	0.7140419756	60.09	80000
2015-03-13	CTIO/1.5m	CHIRON	1	1200	2457094.71578943	0.1973660624	0.7148213480	52.11	80000
2015-03-16	CTIO/1.5m	CHIRON	1	1200	2457097.70121347	0.2865098080	0.7171482568	53.50	80000
2015-03-19	CTIO/1.5m	CHIRON	1	1200	2457100.64933568	0.3745397337	0.7194460917	63.64	80000
2015-03-22	CTIO/1.5m	CHIRON	1	1200	2457103.62769326	0.4634724772	0.7217674928	36.06	80000
2015-04-03	CTIO/1.5m	CHIRON	1	1200	2457115.62824705	0.8218049283	0.7311210032	76.57	80000
2015-04-06	CTIO/1.5m	CHIRON	1	1200	2457118.57643026	0.9098366754	0.7334188856	62.55	80000
2015-04-09	CTIO/1.5m	CHIRON	1	1200	2457121.61299987	0.0005076103	0.7357856585	50.84	80000
2015-04-09	CTIO/1.5m	CHIRON	1	3360	2457121.68248558	0.0025824300	0.7358398173	102.58	80000
2015-04-09	CTIO/1.5m	CHIRON	1	3360	2457121.72158038	0.0037497874	0.7358702887	101.85	80000
2015-04-10	CTIO/1.5m	CHIRON	1	1200	2457122.62723699	0.0307923855	0.7365761785	51.96	80000
2015-04-10	CTIO/1.5m	CHIRON	1	3360	2457122.68590166	0.0325440926	0.7366219031	68.10	80000
2015-04-11	CTIO/1.5m	CHIRON	1	1200	2457123.60255273	0.0599149815	0.7373363622	60.33	80000
2015-04-13	CTIO/1.5m	CHIRON	1	1200	2457125.54243230	0.1178391251	0.7388483494	42.48	80000
2015-04-17	CTIO/1.5m	CHIRON	1	1200	2457129.53506219	0.2370576945	0.7419602979	59.30	80000
2015-04-20	CTIO/1.5m	CHIRON	1	1200	2457132.67083800	0.3306908928	0.7444043944	57.25	80000
2015-04-23	CTIO/1.5m	CHIRON	1	1200	2457135.59115892	0.4178906814	0.7466805603	67.59	80000
2015-04-26	CTIO/1.5m	CHIRON	1	1200	2457138.60097040	0.5077626277	0.7490264773	44.16	80000
2015-04-29	CTIO/1.5m	CHIRON	1	1200	2457141.63049700	0.5982232607	0.7513877607	45.85	80000
2015-05-03	CTIO/1.5m	CHIRON	1	1200	2457145.71165279	0.7200851833	0.7545687083	35.71	80000
2015-05-06	CTIO/1.5m	CHIRON	1	1200	2457148.69643838	0.8092098650	0.7568951195	56.81	80000
2015-05-09	CTIO/1.5m	CHIRON	1	1200	2457151.80714083	0.9020943813	0.7593196733	55.85	80000
2015-05-10	CTIO/1.5m	CHIRON	1	1200	2457152.61159559	0.9261151266	0.7599466840	38.55	80000
2015-05-13	CTIO/1.5m	CHIRON	1	1200	2457155.58329222	0.0148489764	0.7622628934	45.06	80000

Table 5.4: Radial velocities of the donor and their errors.

HJD	RV (km s^{-1})	error (km s^{-1})
2457078.74075340	-107.007	0.464
2457078.76179291	-106.801	0.391
2457081.64889093	-98.052	0.496
2457084.80281535	-56.000	0.649
2457087.65572745	-2.660	0.705
2457090.67030988	54.155	0.854
2457093.71585473	94.720	1.105
2457094.71578943	101.841	0.977
2457097.70121347	101.745	1.098
2457100.64933568	71.432	1.260
2457103.62769326	15.153	1.791
2457115.62824705	-93.987	0.728
2457118.57643026	-50.599	0.944
2457121.61299987	7.012	0.720
2457121.68248558	8.738	0.769
2457121.72158038	9.406	0.749
2457122.62723699	26.157	1.172
2457122.68590166	27.430	1.147
2457123.60255273	44.459	1.214
2457125.54243230	75.944	1.018
2457129.53506219	105.475	1.007
2457132.67083800	89.557	0.901
2457135.59115892	48.835	1.292
2457138.60097040	-18.296	1.658
2457141.63049700	-69.054	1.008
2457145.71165279	-107.108	0.664
2457148.69643838	-97.126	0.781
2457151.80714083	-54.372	1.042
2457152.61159559	-41.587	1.021
2457155.58329222	15.412	0.771

Table 5.5: Radial velocities of the gainer and their errors.

HJD	RV (km s^{-1})	error (km s^{-1})
2457121.61299987	16.455	0.611
2457121.68248558	17.276	0.599
2457121.72158038	11.927	0.600
2457123.60255273	7.559	0.624
2457090.67030988	5.428	0.624
2457093.71585473	-4.516	0.610
2457094.71578943	-4.310	0.608
2457129.53506219	-4.208	0.608
2457062.78265893	-6.731	0.603
2457062.80354576	-6.808	0.603
2457097.70121347	-11.708	0.609
2457132.67083800	-15.873	0.604
2457065.73864590	-16.498	0.611
2457065.75953170	-15.399	0.611
2457138.60097040	-16.877	0.619
2457071.65142447	-12.784	0.627
2457071.67231145	-14.066	0.616
2457074.85684834	-7.853	0.614
2457145.71165279	8.475	0.614
2457078.74075340	9.035	0.606
2457078.76179291	8.733	0.605
2457148.69643838	15.724	0.607
2457087.65572745	8.391	0.616

Table 5.6: Radial velocities of He I 5875 and their errors

HJD	RV (km s^{-1})	error (km s^{-1})
2457121.61299987	-130.882	0.685
2457121.68248558	-134.489	0.607
2457121.72158038	-128.763	0.363
2457155.58329222	-122.714	0.032
2457122.62723699	-110.354	3.539
2457122.68590166	-104.390	0.660
2457123.60255273	-82.371	0.255
2457090.67030988	-80.060	0.291
2457125.54243230	-62.002	1.056
2457093.71585473	-37.893	1.700
2457094.71578943	-38.739	2.546
2457129.53506219	-33.361	0.696
2457062.78265893	-26.676	0.435
2457062.80354576	-27.353	2.761
2457097.70121347	-42.736	0.463
2457065.73864590	-40.997	1.276
2457065.75953170	-56.653	1.059
2457100.64933568	-58.969	0.314
2457135.59115892	-82.542	1.205
2457068.81094574	-93.843	7.426
2457068.83183151	-99.579	1.821
2457103.62769326	-116.214	0.815
2457138.60097040	-138.043	1.183
2457071.65142447	-139.524	1.116
2457074.85684834	-211.019	0.267
2457074.85684834	-211.019	0.267
2457145.71165279	-245.749	0.820
2457078.74075340	-244.460	0.849
2457078.76179291	-239.287	2.241
2457081.64889093	-232.824	1.144
2457148.69643838	-234.363	0.394
2457084.80281535	-180.051	1.567
2457151.80714083	-189.062	0.497
2457118.57643026	-172.555	2.148
2457152.61159559	-179.926	1.442
2457087.65572745	-140.905	1.524

Table 5.7: Photometry points extracted from Vizier Catalogue with a search radius of 2 arsec to build the Spectral Energy Distribution

wavelength A	Obs. Flux erg/s/cm ² /A	Obs. Error erg/s/cm ² /A	Filter ID
4280	3.8961272708038E - 13	1.0765397488993E - 14	TYCHO/TYCHO.B
4297.1691826842	3.3568742904622E - 13	1.6077336496569E - 13	Misc/APASS.B
4640.4198339016	3.6790221791186E - 13	1.2469697114109E - 13	Misc/APASS.sdss _g
5340	3.9470079496967E - 13	9.0883216669006E - 15	TYCHO/TYCHO.V
5394.2913582927	3.0914068920168E - 13	1.3638523748095E - 13	Misc/APASS.V
6122.3296283695	4.1249010772103E - 13	2.1731276951292E - 13	Misc/APASS.sdss _r
7439.4904529922	3.6321232166977E - 13	1.9135168108482E - 13	Misc/APASS.sdss _i
7862.1015966	2.7060061005582E - 13	4.9846474469570E - 15	DENIS/DENIS.I
12210.6027581	1.6530536695297E - 13	3.3495411288929E - 14	DENIS/DENIS.J
12350	1.5958995899691E - 13	3.3807190373159E - 15	2MASS/2MASS.J
16620	8.8762578525412E - 14	1.6350671210266E - 15	2MASS/2MASS.H
21465.009653	4.1737018974359E - 14	1.9220607543274E - 15	DENIS/DENIS.Ks
21590	4.1204825037746E - 14	9.1082511255687E - 16	2MASS/2MASS.Ks
33526	9.0757866535675E - 15	2.7585057793523E - 16	WISE/WISE.W1
46028	2.9820652029785E - 15	5.2185087508631E - 17	WISE/WISE.W2
82283.5545614	5.3621475465995E - 16	3.7105529678368E - 17	AKARI/IRC.S9W
115608	1.1671349817430E - 16	1.6124565662840E - 18	WISE/WISE.W3
220883	1.4612560240564E - 17	6.4601593690368E - 19	WISE/WISE.W4



Chapter 6

Evolutionary process of the Double Periodic Variable: V495 Centauri

Rosales, J. A.¹, Mennickent, R. E.¹, Schleicher, D. R. G.¹, Senhadji, A. A.²

¹ *Departamento de Astronomía, Universidad de Concepción, Casilla 160-C, Concepción, Chile.*

² *Physics and Astronomy Department, Bishop's University, Sherbrooke, Canadá.*

Published: Monthly Notices of the Royal Astronomical Society

6.1 Abstract

We present a simple model for the Double Periodic Variable (DPV) V495 Cen, which evolves as a binary system of intermediate mass, where the gainer cannot accrete at high rate, limited by the Eddington accretion rate, leading to the formation of an accretion disc. The theoretical model begins at the zero age main sequence considering the rotation for both stars. For this purpose we used the stellar evolution code MESA, developed to calculate the evolution of stars in a wide range of parameters. We started the model adjusting fundamental parameters published for this system through a chi-square optimization algorithm, and adopting an initial orbital period of 3.9 days and initial masses for the primary component $M_{i,d} = 3.40 M_{\odot}$ and $M_{i,g} = 3.18 M_{\odot}$ for the gainer, with a metallicity associated to this type of DPV of $Z = 0.02$. The method converged successfully for eight free degrees and 5% of confidence with a chi-square of $\Delta\chi_{0.95,8}^2 = 0.212$. We describe each evolutionary stage of both components until that the donor reaches 20% core helium depletion as stop criterion. We offer a complementary analysis for understanding the mechanism of the magnetic dynamos inside the donor star using the Tayler-Spruit formalism. Currently, the theoretical model is consistent with the fundamental parameters published for V495 Cen and we discuss how our predictions can help to develop efficient theoretical models for DPV stars.

6.2 Introduction

The evolution of Double Periodic Variables (DPV) has been little studied to date. Our understanding of the internal structure of each component is based on spectroscopy and photometric studies of the last years. These system are binary stars of intermediate mass that show two photometric

variations, where the long period is on average about 33 times longer than the orbital period (Mennickent et al., 2003; Mennickent, 2017). A property of these systems is the constancy of their orbital period, which is not expected in classical Algols undergoing Roche Lobe Over Flow (RLOF) mass transfer (Garrido et al., 2013), mainly because intermediate mass binaries evolve in a conservative way, but the mass will be blown away from the system during the short era of rapid mass-transfer soon after the onset of RLOF (van Rensbergen et al., 2008). The increase of mass loss from a binary system is related to the initial orbital period and the initial mass of the donor. I.e., if we compare two binary systems of equal total masses, then the system that present the largest initial orbital period will be the one who loses more mass. The same occurs at the case of the initial mass of the donor (van Rensbergen et al., 2011).

The Algol system already presented a cycle of 32 year, reported by Soderhjelm (1980), which was not linked to the orbit of the system. Years later, Applegate & Patterson (1987) proposed a mechanism to produce the observed long-term period variations as result of magnetic activity cycles, produced on the external convection zone of one star of the system, responsible for the changes in the orbital period on a time scale of order 10 years. Then Sarna et al. (1997), examined the possibility of tracking the existence of dynamos in Algol type binary stars that show mass loss. Later Meintjes (2004) described episodes of magnetized mass transfer in the cataclysmic variable AE Aquarii, subsequently Peterson et al. (2010) reported magnetic activity in a close binary Algol, where the most evolved component is a bright radio active KIV star while its companion is a star of the main sequence of spectral type B8. They suggested that both stars are aligned by a persistent asymmetric magnetic field between both stars. Currently, the second period is linked to mechanisms based on magnetic dynamo cycles of the donor star is proposed by Schleicher & Mennickent (2017) and variations of the wind generated by impact of a gas stream onto the accretion disc (Mennickent et al., 2012, 2016). The DPV V495 Centauri is currently studied through photometric and spectroscopic analysis by Rosales Guzmán et al. (2018). The system includes an evolved star with characteristics of an F-type star, transferring mass onto an early B-type dwarf, hidden by an optically and geometrically thick disc of radial extension $R_d = 40.2 \pm 1.3 R_\odot$. Some one the characteristics of this system are that it has an extremely long period of 1283 days, shows a persistent $V < R$ asymmetry of the $H\alpha$ emission line and shows also the presence of a possible wind formed in the hotspot region. The fundamental parameters proposed for this system include an accretion disc around the gainer star, which is in agreement with the spectral energy distribution that shows infrared excess indicating the presence of circumstellar material. We offer a complementary analysis of the system V495 Cen to understand the evolution of stars in a binary system as a DPV, applying the modern stellar evolution code MESA¹ (Eggleton, 1971; Paxton, 2004; Paxton et al., 2011, 2013) developed to calculate evolution of stars in a wide range of parameters, with independent modules for experiments in stellar astrophysics of close binary systems (Paxton et al., 2015, 2018).

6.3 On the model

When the primary star expands beyond a critical volume called Roche lobe and increases its radius, it begins eventually to interact with the companion. The module for experiments with a close binary star of MESA is developed to find an analytic approximation of the Roche lobe around of the primary star, according to:

$$R_L = a \frac{0.49q^{2/3}}{0.6q^{2/3} + \ln(1 + q^{1/3})}, \quad (6.1)$$

¹<http://mesa.sourceforge.net/>

(Eggleton (2006), eq. 3.5) where R_L is the effective radius for the critical equipotential of the Roche lobe and $q = m_2/m_1$ the mass ratio. Normally, in the binary system we distinguish three cases of mass transfer based on the evolutionary stage of the donor star, when it fills the Roche lobe, defined by Kippenhahn & Weigert (1967) and Lauterborn (1970):

(i) Case A : The donor star evolves first filling the Roche lobe during the core hydrogen burning. Here the evolution is slow (nuclear timescale), and during its process of mass transfer the donor star evolves in a stable way along of the main sequence.

(ii) Case B : The donor has filled the Roche lobe and leaved the main sequence. This process occurs before core helium ignition, the mass transfer is driven by the fast expansion of the donor in a thermal timescale since the donor is crossing the Hertzsprung-gap while is burning hydrogen in a shell.

(iii) Case C : The donor star has filled the Roche lobe after the core helium ignition, both stars interact before the donor ends its life. In high mass stars the mass transfer occurs in a dynamical timescale and it is often unstable.

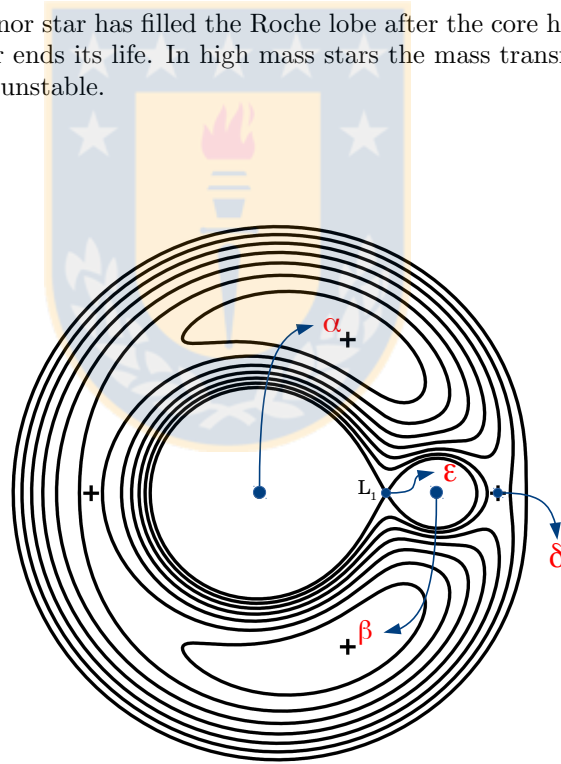


Figure 6.1: Mass loss/transfer fraction. α correspond to the fraction of mass lost from the vicinity of the donor as fast wind, β mass lost from the vicinity of the accretor, δ is the mass lost from the circumbinary coplanar toroid and ϵ is the fraction of accreted mass.

6.3.1 Mass transfer

Particularly, the mass transfer produces important effects in the stars. This process can be accompanied by stellar winds from the mass-losing star, or ejection of matter from the accretor (Soberman et al., 1997). In our calculation, we take into account the following mass loss/transfer fractions (see Fig. 6.1); α : the Jeans's mode is a fast mode, associated to a spherically symmetric outflow from the donor star in form of a fast wind; β : at the isotropic re-emission, the flow is transported from the donor star to the vicinity of the accretor, where it is ejected as a fast isotropic wind; δ : this mode is considered an intermediate mode or mass loss to a ring. The ejection of the mass has the characteristic of the angular momentum of a circumbinary ring; ϵ : is the fraction of the mass accreted by the secondary. The donor star has filled the Roche lobe, here the matter is lost from vicinity of the donor, through the inner Lagrange point, to the vicinity of the accretor, which arrives with high angular momentum. However, the δ mode was not considered because a circumbinary coplanar toroid, is not observed in the DPV V495 Cen.

When the donor expands, the flow from the outermost layers accelerates and converges towards the Lagrangian point L_1 (Fig. 6.1), it reaches sound velocities near the point L_1 , and fall onto the gainer with a mass transfer rate given by Kolb & Ritter (1990):

$$\dot{M} = \int \rho_L \nu_s dA, \quad (6.2)$$

where ρ_L and ν_s are the density and the sound speed of the flow at the L_1 point, respectively. But, the mass transfer from the primary star (donor) to the companion is limited by the Eddington accretion rate. This accretion represents the rate at which the radiation produced by the heated infalling material is strong enough to prevent the accretion:

$$\dot{M}_{Edd} = \frac{4\pi cR}{\kappa}, \quad (6.3)$$

(Burger & Katz (1983), eq. 3), where R is the radius of the accreting star and κ is the opacity. MESA assumes the mass losses in a stellar wind has a specific orbital angular momentum. Therefore for an inefficient mass transfer, where fixed fractions of the transferred mass are lost either as a fast isotropic wind from each star or a circumbinary toroid are compatible. Also MESA always ensures that the mass loss/transfer are always consistent with each other, as both are calculated self-consistently, i.e. this provides both explicit and implicit methods to compute mass transfer rates. An explicit computation sets the value of \dot{M}_{RLOF} at the start of a step, while an implicit one begins with a guess for \dot{M}_{RLOF} and iterates until the required tolerance is reached. The composition of accreted material is set to that of the donor surface, and the specific entropy of accreted material is the same as the surface of the accretor (Paxton et al., 2015).

6.3.2 Mass loss

After adjusting the mass transfer of the binary system, we have implemented the mass loss due to winds. We used the model of Reimers (1975) for the mass loss in red giants, while for AGB stars towards the stage of the white dwarf the mass loss will be considered based on dynamical calculation of the atmospheres of Mira-like stars proposed by Bloeker (1995). In addition, for a range of stars within the H-R diagram, the mass loss is represented by a function depending only on T_{eff} and L of the stars proposed by de Jager et al. (1988), but when we deal with mass loss for massive stars is recommended to use the models of Nieuwenhuijzen & de Jager (1990). However, in

another cases for stars like Wolf-Rayet the model of [Nugis & Lamers \(2000\)](#) is implemented. Unlike the previous case of mass loss in O and B stars, where it is related with their metallicities ([Vink et al., 2001](#)), while the massive stars can be worked with the model of [Glebbeek et al. \(2009\)](#).

In other cases such as supersonic mass loss one could consider the formalism by [Priyalnik & Kovetz \(1995\)](#), and when we deal with super Eddington mass loss we should use the formalism by [Paczynski & Proszynski \(1986\)](#). Finally, to ensure the correct representation of the mass loss process in intermediate mass stars through the He-core burning phase, we have to consider time steps small enough to allow the convergence of the results.

6.3.3 Internal structure and rotation

The relevance of the rotation in the stars is that the centrifugal forces interacting with the matter drive deviations from spherical symmetry. It is known that large mean rotational velocities are common among the early-type stars and that these velocities decline steeply in the F-star region, from 150 km s^{-1} to less than 10 km s^{-1} ([Tassoul, 2000](#)). The instabilities discussed in this section are a list of all rotationally induced instabilities, relevant for stellar evolution of intermediate mass within our model, which are included in MESA code. However, they are well studied by [Heger et al. \(2000, 2005\)](#) and are in general relevant for the present case.

The dynamical shear instability (mixing process) ([Zahn, 1992](#)) is an instability that occurs when the energy that is gained from the shear flow becomes comparable to the work that has to be done against the gravitational potential for the adiabatic turnover of a mass element, i.e., this means that this instability is stabilized by density gradients. Another type of instability related to adiabatic process is the called Solberg-Hoiland (SB) ([Wasiutynski, 1946](#)) instability, which arises if an adiabatically displaced mass element experiences a net force that has components in the direction of the displacement. It is a convective instability type favored by stellar rotation, just if the outward decrease in angular velocity is moderate according to the Rayleigh criterion:

$$\frac{dj}{d\bar{\omega}} = \bar{\omega} \left(\bar{\omega} \frac{d\Omega}{d\bar{\omega}} + 2\Omega \right) > 0 \quad \text{or} \quad \frac{d \ln \Omega}{d \ln \bar{\omega}} > -2 \quad (6.4)$$

where $j = \bar{\omega}^2 \Omega$ is the angular momentum, Ω angular velocity and $\bar{\omega}$ is the distance from rotational axis until the element fluid ([Maeder, 2009](#)). Despite that we have not used this instability for the internal structure of our stars we consider that is necessary to be mentioned due to the relationship that it has with the previous instability and the accretion discs.

Another interesting instability that can occur in radiative stellar zones due to the presence of inverse gradients of the mean molecular weight μ , is the thermohaline convection. Here the mean molecular weight gradient $\nabla_{\mu} = d \ln \mu / d \ln P$ plays the role of the gradient of the average mass per particle relative to the mass of hydrogen, while the difference between the adiabatic term and the local (radiative) gradient $\nabla_{ad} - \nabla$ plays the role of the temperature ([Vauclair, 2008](#)), i.e., this mechanism governs the photospheric composition of bright giants of low mass, and is a type of double diffusive instability which is observed as elongated fingers. This instability is induced by the molecular weight inversion created by the ${}^3\text{He} + {}^3\text{He} \rightarrow {}^4\text{He} + {}^2\text{H}$ reaction in the outer zone of the hydrogen combustion layer, converting two particles to three as predicted by [Ulrich \(1972\)](#). It is expected that it will stabilize after the first dredging, when the star reaches the RGB brightness.

When the radiative gradient ∇_{rad} is intermediate between the stability predicted by Ledoux criterion and the instability predicted by the Schwarzschild criterion it is called semiconvection:

$$\nabla_{int} < \nabla < \nabla_{int} + \left(\frac{\varphi}{\delta} \right) \nabla_{\mu}, \quad (6.5)$$

with $\nabla_{int} \approx \nabla_{ad}$ and $\nabla \approx \nabla_{rad}$ (Maeder, 2009). The semi convection (Kato, 1966) is a type of instability that can occur in non rotating stars. It is a secular shear instability, i.e., this type of instability appears in regions where an unstable temperature gradient is stabilized against convection by a sufficiently large gradient of mean molecular weight. However, we know that our objects are rotating stars and, therefore, we have considered the Eddington-Sweet circulation (Baker & Kippenhahn, 1959), which considers that a rotating star cannot be in hydrostatic and radiative thermal equilibrium at the same time. This is because surfaces of constant temperature and constant pressure do not coincide. Consequently, large-scale circulations develop. Since inhomogeneities on isobars are quickly smoothed out by the horizontal turbulence only the perpendicular component of the circulation velocity is considered here, and the process is approximated by diffusion along the radial coordinate.

Inasmuch as the temperature plays a fundamental role in the stars, the Goldreich-Schubert-Fricke (GSF) instability (Goldreich & Schubert, 1967; Fricke, 1968) is essential to study the instability in rotating stars whose profiles show gradients along radial and vertical coordinates. It is composed by two criteria, the first is related to the stabilization by the temperature gradient, which is removed due to thermal conduction. The second criterion is analogue to Taylor-Proudman (Kippenhahn, 1974; Tassoul, 1978) for slowly rotating incompressible fluids. But it is thought that GSF is probably far less efficient in the transport of angular momentum than it is often assumed (Caleo et al., 2016). Therefore the condition for this instability in the limit of no viscosity and no stratification is:

$$\left| \frac{\partial(rv_o)}{\partial r} \right| > \left| \frac{l_r}{l_z} \frac{\partial(rv_o)}{\partial z} \right|, \quad (6.6)$$

where l_r and l_z are the radial and vertical length scales of the system (Regev et al., 2016) and r represents a radial boundary. The criterion says, if the vertical gradient of the swirling flow is weak, then this instability is expected only for short radial wavelength disturbances.

One of the more effective ways of transport of angular momentum and magnetic field amplification is the Spruit-Tayler dynamo proposed by Spruit (2002), which provides estimates for the magnetic field components B_r and B_ϕ based on dynamo processes that take into account the effect of stable stratifications. This model assumes that the rotation rate is a function of the radial coordinate and the initial magnetic field must be sufficiently weak to neglect the initial magnetic forces and allow the radial component B_r to be wound by the differential rotation, later of some turns this would be predominately azimuthal i.e., $B_\phi > B_r$ and increases linearly until be unstable. Therefore in this case the differential rotation is sufficiently strong to maintain a dynamo process. Then, the azimuthal field produced must be large enough to generate the Tayler instability. Considering an instability without thermal diffusion overestimates the intensity of the field required for this, if the stratification is due to the thermal gradient. When the stabilizing stratification is due to the entropy gradient, the heat is transported by the photons. While the viscosity and magnetic fields are diffused by Coulomb interactions, known as the Prandtl number, here the viscosity is of the same order as the magnetic diffusivity, and at the same time it is the mechanism that controls the magnetic diffusion. Therefore the stabilizing effect of the stratification due to the entropy gradient is reduced by thermal diffusion, and the instabilities may appear more easily. Independent of the intensity of the azimuth field, the condition derived by Spruit is:

$$\frac{\omega_A}{\Omega} > \left(\frac{N}{\Omega} \right)^{1/2} \left(\frac{\kappa}{r^2 \Omega} \right)^{1/4} \left(\frac{\eta}{\kappa} \right)^{1/2}, \quad (6.7)$$

where the conditions to validate the previous equation are $\omega_a \ll N \ll \Omega$ and $\eta \ll \kappa$. In the above equation η is the magnetic diffusivity (cm^2s^{-1}), N is the buoyancy frequency, Ω the rotation rate, κ is the thermal diffusivity and r is the radial length scale (Spruit, 2002). Also the minimum shear rate q required to produce the critical magnetic field strengths for Taylor instability and drive convective motions are:

$$q_0 = \left(\frac{N}{\Omega}\right)^{7/4} \left(\frac{\eta}{r^2 N}\right)^{1/4} \quad (6.8)$$

$$q_1 = \left(\frac{N}{\Omega}\right)^{7/4} \left(\frac{\eta}{r^2 N}\right)^{1/4} \left(\frac{\eta}{\kappa}\right)^{3/4}, \quad (6.9)$$

wherein q is the dimensionless differential rotation rate when the thermal diffusion can be neglected q_0 , and when the thermal diffusion is considered q_1 , i.e., when the effects of stratification is dominated by the composition gradient. The overshooting process depends on the adjacent convective layers, where the acceleration of the cells is zero or null, i.e., a neutral stability corresponds when $\nabla_{rad} = \nabla_{ad}$, but strictly speaking the temperature gradient must be slightly sub-adiabatic, otherwise the convective elements never show deceleration (Kippenhahn), this process is also known by other authors as convective penetration. The difference that exists between kinematic and dynamic edges is the average overshooting distance $d_{over} = |r_v - r\Delta t|$ to which the convective mixture extends, beyond the formal limit defined by Schwarzschild or Ledoux (Maeder, 2009). When the rotation is present in a convective core the SH criterion and the semi convection could influence the overshooting process, in turn the overshooting will determine the amount of nuclear fuel for the star and thus directly affecting the age of the star (Meakin & Arnett, 2007). Another effect that can extend the convective core is the rotational mixing, which conducts more hydrogen in the center, which can change the global properties of a solar-type star with a significant increase of the effective temperature, producing a change in the evolutionary track of the star due to the rotational mixing counteracts the effects of atomic diffusion (Eggenberger et al., 2010). In addition the mixing effects grow with age, because the mixture has more time to influence the distribution of elements (Maeder, 2009).

We want emphasize that the Tayler-Spruit dynamo is certainly a fundamental ingredient among the processes considered here, as it is the only process that can generate a magnetic field, and which may also drive convection due to magnetic instabilities. As we will show in the next chapters, thermohaline convection is also quite important during the later phases of binary evolution, though more for the gainer rather than for the donor. The models employed here are based on approximate descriptions, as the processes themselves are highly non-linear. While in principle a 3D treatment would be required, the latter is not feasible if the system is followed over a significant portion of the lifetime of the star. The results therefore have to be taken “cum grano salis”, as a fully consistent treatment is not possible at present.

6.3.4 The fitting procedure

We present a MESA model which evolves a binary system of intermediate mass, and we have specified to MESA how should treat the mass transfer from the donor star to the companion, which cannot accrete at a high rate, limited by the Eddington accretion rate, i.e., simulating the formation of an accretion disc on the gainer star. The theoretical model begins at the zero-age main sequence with rotation for both stars, but we have constrained the rotation of the primary star (donor) to 26 km s^{-1} as initial conditions to never reach high rotation rates during their evolution. Also we

consider a binary interaction with practically almost conservative processes. We initiated the model using parameters previously derived for the DPV V495 Cen (Rosales Guzmán et al. (2018), Table 2), adopting an initial orbital period 3.6 to 4.6 d with steps of 0.1 d, an initial mass for the primary component (donor) of 3.0 to 5.1 M_{\odot} with step of 0.01 M_{\odot} and for the companion (gainer) of 1.9 to 4.0 M_{\odot} with steps of 0.01 M_{\odot} . The metallicity associated to the DPV is $Z = 0.02$. Also, both stars include differential rotational and the controls to generate a dynamo model considering a Solberg-Hoiland (SH) instability, the diffusion coefficient for angular momentum, secular shear instability (SSI), Eddington-Sweet (ES) circulation, and the Spruit-Tayler (ST) dynamo. The surface rotation for the primary component is 26 km s^{-1} , while that for the companion the surface rotation is a free parameter that can be estimated by MESA assuming synchronous rotation. The principal stopping criterion for the evolution is when the primary star reaches core helium depletion ($X_{\text{He}_{4c}} < 0.2$). We considered a semiconvection according to the Ledoux criterion (Lebreton et al., 2009) where the stability occurs if the radiative gradient is less than adiabatic gradient $\nabla(r) < \nabla(L)$. The convective overshooting and a wind mass loss are considered according to de Jager et al. (1988) for a cool wind described by Bloeker (1995).

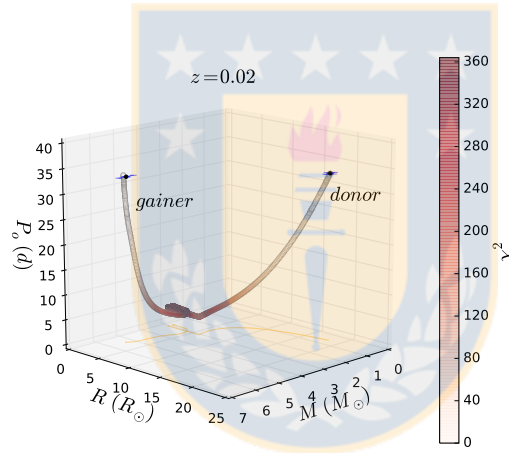


Figure 6.2: Best model for V495 Cen of 8 freedom degree with all optimized parameters values for both stars, with a $\Delta\chi_{0.95,8}^2 = 0.212$.

Our model is aimed to find the best fit, which was based on a chi-square optimization algorithm. The method allows the simultaneous determination of various parameters such as radius, masses, orbital period, luminosities and temperatures. The optimization method converged successfully for the initial parameters of orbital period $P_{i,o} = 3.9$ d, mass of the donor star $M_{i,d} = 3.40 M_{\odot}$, mass of the gainer $M_{i,g} = 3.18 M_{\odot}$ with a chi-square of $\Delta\chi_{0.95,8}^2 = 0.212$ (Fig. 6.2).

We have compared the published values of the masses, radius, orbital period and radial velocities of V495 Cen by Rosales Guzmán et al. (2018) with our best model and the main feature presented is the great consistency between theoretical and observed values. We noted that the orbital period as a function of the mass of the primary component (donor) is relatively constant until to 2.5 M_{\odot} and it changes abruptly around of 1.5 M_{\odot} (Fig. 6.3). This suggests that the system is in a stage of change in its orbital period as the mass of the primary star varies. During the evolution of the system, we note that the orbital velocity of the primary component increases (Fig. 6.4, black line), reaches a peak around 150 km s^{-1} and then decreases to about 106 km s^{-1}

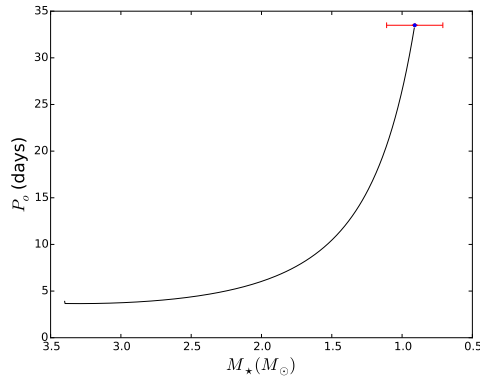


Figure 6.3: Evolution of the orbital period as a function of the mass of the primary star (donor) of V495 Cen.

for a mass of $0.91 m_{\odot}$. The companion decreases its orbital velocity to 16 km s^{-1} for a mass of $5.76 m_{\odot}$ (Fig. 6.4, dashed red line). Also, we performed a study of the behavior of the radius as function of the mass for both stars (Fig. 6.5), that shows a small change in radius whereas the mass increases in the gainer star (dashed red line), possibly due to the rejuvenation process of this star produced by mass accretion. The primary component (black line) increases rapidly their size as its mass decreases. With respect to the mass transfer from the primary star toward the companion it proceeds in a quasi steady manner during most of time (Fig. 6.6). In summary, the theoretical model is consistent with the published results of V495 Cen.

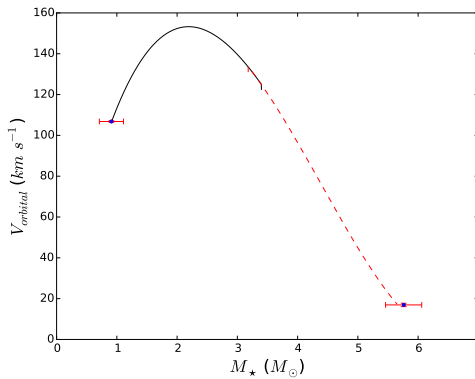


Figure 6.4: Orbital velocities curve for both components as a function of their masses. The primary component (black line) increases their orbital velocity during the loss mass process known as spin-up and later decrease reaching the current value. The secondary (dashed red line) component shows a diminutions of their radial velocity and a mass gain.

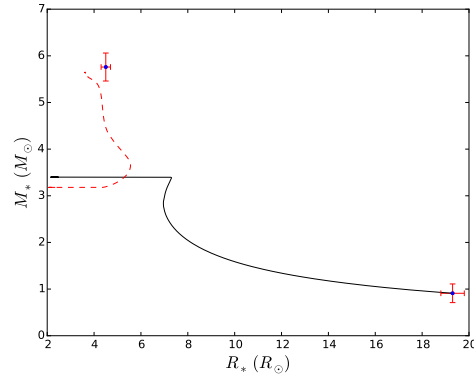


Figure 6.5: Schematic behavior of radius and mass for both stars. The gainer star (dashed red line) decreases its radius, while the donor star (black line) expands to fill the Roche lobe.

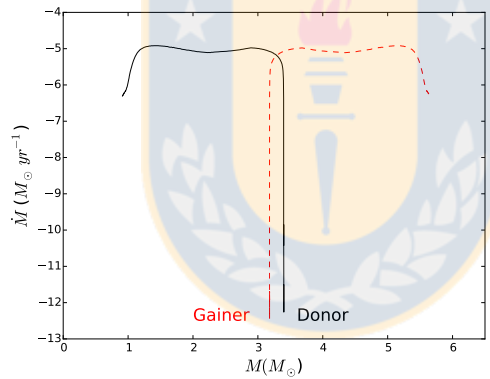


Figure 6.6: Theoretical variation of mass transfer until reaching the helium depletion for initial masses $M_{i,d} = 3.40 M_{\odot}$, $M_{i,g} = 3.18 M_{\odot}$ with initial orbital period $P_{i,o} = 3.9$ d.

6.4 Evolution of the DPV 495 Cen in the HR diagram

The evolution of both stars begins on the zero main sequence (ZAMS) with the hydrogen burning, labeled as A-point (Fig. 6.7). Both stars evolve similarly as they move, and the central helium abundances $X_{He,c}$ rises steadily as both stars fuse hydrogen into helium in their convective cores. During this phase, the primary star evolves, increasing its size and quickly depleting the central hydrogen, while the companion (gainer) preserves its initial volume, this can be seen in Fig. 6.7. Once the donor star has exhausted the central hydrogen (B-point) at age 2.980×10^8 yr, it quickly start the hydrogen shell burning, causing an increase of its luminosity (C-point) and temperature, at age around 3.012×10^8 yr. After this phase, the primary star decreases its luminosity by less than one order of magnitude and stabilizes its temperature, and starts (D-point) the optically thick mass transfer at age 3.0133×10^8 yr, causing a rejuvenation of the companion (gainer star). The initial mass of the primary component decreases until reaching an equilibrium of both mass (U_1 -

point) where $m_1=m_2$, i.e., the mass ratio $q = 1$, at 3.0136×10^8 yr. After mass ratio inversion, the donor star moves to the minimum value of the Roche lobe at 3.0142×10^8 yr (E-point), arriving to the end of the phase of optically thick mass transfer (U_2 -point) at 3.0159×10^8 yr, where the donor luminosity drops about an order of magnitude, because the deeper layers of the donor need to expand as they adjust to the quickly decreasing mass. Finally, the donor star finishes the mass transfer stage (F-point) at the age 3.0268×10^8 yr and then continues as a detached binary system.

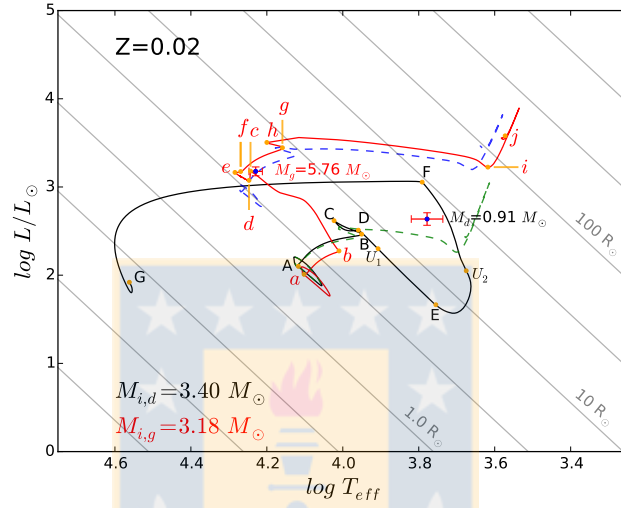


Figure 6.7: Evolutionary track of primary or donor star (black line) and its companion (red line). The important points of the evolution were labeled together to the initial masses. The dashed green line correspond to evolutionary track of a single star of initial mass $M_{i,s} = 3.40 M_{\odot}$ using the same initial parameters of the donor star until the central helium depletion ($X_{H,e,c} < 0.2$). The dashed blue line is the evolutive track for a single star of mass $5.76 M_{\odot}$ with the similar characteristics of the gainer star.

The stages C, D, U_1 of the donor star occur rapidly, causing a hook in the evolutionary track of the gainer star (Fig. 6.7, red line, b -point), preserving its volume and beginning a rejuvenation. The process that occurs at the D-point, illustrate the well-known fact that the change of the orbital period is completely bound to the mass transfer process (Fig. 6.9). This can be seen in the Fig. 6.10, where we plot how the mass transfer changes as a function of time, also we indicate the processes of the onset of the mass transfer until the end of the optically thick mass transfer. The central density of the donor star is bound to the mass transfer, increasing gradually fast during the process, from the start of the mass transfer process until the mass inversion the central density increased $\sim 2.8 \text{ g cm}^{-3}$.

When the gainer begins the central hydrogen burning it reaches the b -point. Then it starts to accrete mass, and rapidly recovers around of 17% of its central hydrogen mass fraction from $X_{H,c} = 0.240$ to $X_{H,c} = 0.419$ until reaches the c -point, causing the second hook in the evolutionary track. After the end of the optically thick mass transfer, the hot star stops its rejuvenation process but continue accreting matter, principally hydrogen from the disc, and begins a stage in which it tries to

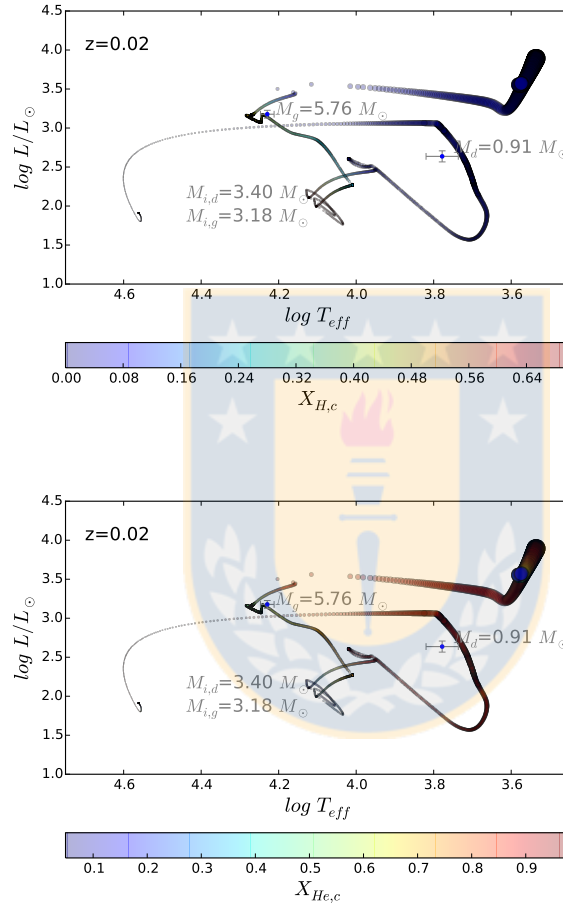


Figure 6.8: Hertzsprung-Russel (H-R) diagrams showing the binary evolution. The color bar shows the central hydrogen and helium mass fraction for both components and confirms a rejuvenation of the gainer retaining their size during great part of their lifetime, whereas that the donor star suffers a rapid evolution exhausting their helium during the mass transfer phase.

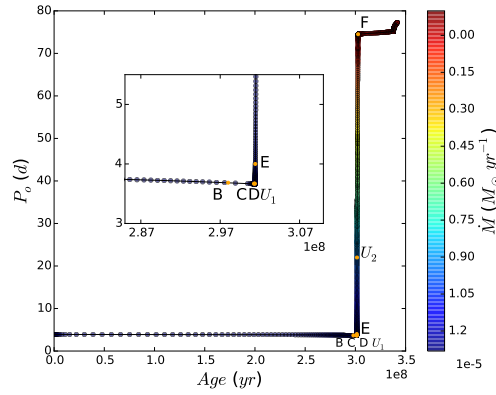


Figure 6.9: Change of the orbital period as a function of the time, labeled with the more important stage related to mass transfer and their change during the mass inversion.

return to the main sequence, moving from the d-point to the e-point, while it continues the central hydrogen burning. Also, during the stages *b* until *e*, the temperature increases around 10,000 K and its luminosity an order of magnitude. Once that the maximum temperature and accreted mass has been reached (*e*-point), the new evolution of the gainer star begins in a sequence parallel to the main sequence for single stars, as if it were similar to a single star of $M = 5.87 M_{\odot}$. (Fig. 6.7, blue dashed line), in addition we added the single track evolution to a star of $M = 3.40 M_{\odot}$ in comparative with the donor star (Fig. 6.7, green dashed line).

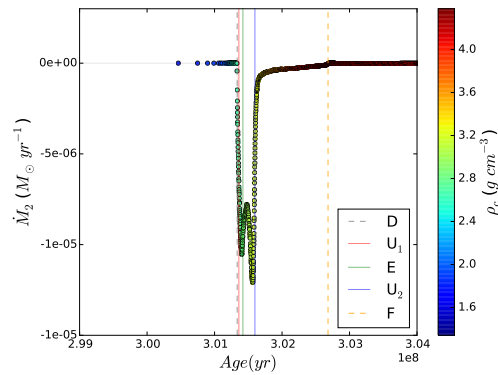


Figure 6.10: \dot{M}_d curve for the best evolutionary model of the donor star. The vertical dashed line (black) indicates the optically thick mass transfer, the continuum the mass ratio $q=1$, i.e. $m_1=m_2$ and the continuum blue line corresponds to the end of the phase of optically thick mass transfer.

6.5 Structural changes in the components of V495 Cen during binary evolution

For intermediate mass stars the theory of convective overshooting and semi convection is particularly complicated. Hence, it is important to emphasize the three classical temperature gradients to constrain and understand the best model. The ratio between the natural logarithms of the derivate (T) and (p) is called ∇ which is defined at any layer within of the star, while the radiative gradient $\nabla_r = (d \ln T / d \ln P)_r$ represents the local heat flux by radiative transport. However, the gas can change adiabatically, therefore for a monatomic ideal gas the adiabatic gradient is $\nabla_a = (d \ln T / d \ln P)_s$, where the s indicate that the derivatives are to be taken in the surrounding material. Therefore, if $\nabla_r < \nabla_a$ in a certain layer, it is stable against convection, if $\nabla = \nabla_r$ all the heat is carried by radiation and finally if $\nabla_r > \nabla_a$ the layer is unstable to convection. We have constructed Kippenhahn diagrams to analyze the internal evolution of both stars with a stopping criterion when the donor reaches core helium depletion $X_{He,c} < 0.2$ (Fig. 6.11).

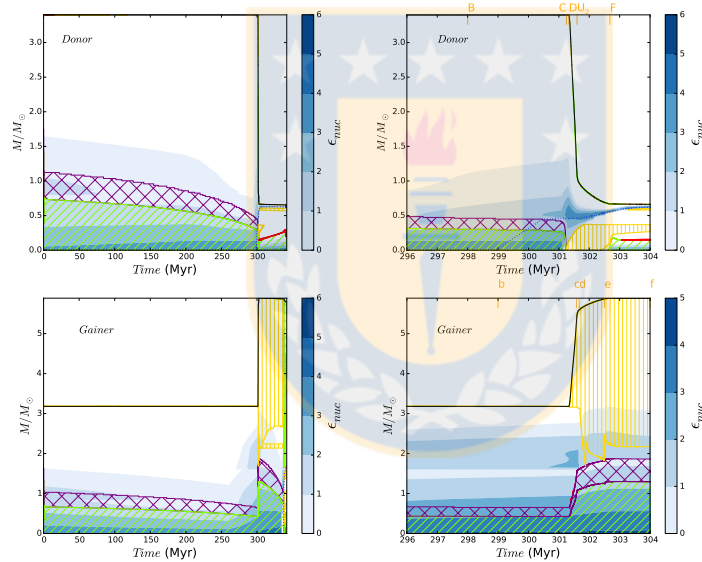


Figure 6.11: (Left) Kippenhahn diagrams showing the evolution of internal structure of both stars, accompanied (Right) by a zoom with some principal events labeled. (Up) diagram of donor star with initial mass $M_{d,i} = 3.40 M_{\odot}$, (Down) diagram of gainer star with initial mass $M_{g,i} = 3.18 M_{\odot}$. Both model stop when the donor star reaches core helium depletion $X_{He,c} < 0.2$. The x-axis give the age after ignition of hydrogen in units of Myr. The different layers are characterized by their values of M/M_{\odot} , convection mixing in hatched green, semi convection mixing in red, overshooting mixing in crosshatched purple, thermohaline mixing in hatched yellow, the solid black line shows the surface of each star and brown zone corresponds to rotational mixing.

The donor star begins from the zero age main sequence (zams) with hydrogen burning and a convective core (hatched green) around of $\sim 0.75 M_{\odot}$ which slowly decreases around of 45% of its central mass at C-point, previously to the moment of beginning the mass transfer process.

Practically, half of the energy generation rate is produced inside of the convective core around of $0.32 M_{\odot}$. After the convective core, we noted an overshooting convection region (crosshatched purple) where the material is carried from an unstable zone to stratified region (Fig. 6.11, up/left), this process causes helium core mass increase after Hydrogen depletion at 299 Myr steadily (Fig. 6.11, up/right, blue dots), later it enters a resting stage during 1.05 Myr whose stage corresponds to the increase of luminosity and temperature (C-point) until the end of optically thick mass transfer (U_2 -point), later the core mass at the end of the main sequence becomes larger than would be expected in single stars, followed by an uncontrolled decrease of the total mass of the star due to the mass transfer. After to the mass transfer, appears a mechanism which governs the photospheric composition: the double diffuse instability is observed as a kind of elongated fingers, caused by the molecular weight inversion created by the ^3He and ^4He (Charbonnel & Zahn, 2007) in the external layer of hydrogen burning, called thermohaline mixing (Fig. 6.11, yellow line). Also we detected that the convective core is governed by a slim layer of semi convective mixing (red line) and for a short time the donor star presents an increase of its internal rotational velocity during the helium depletion producing new stream in the stellar matter conducting the matter from the center to the surface and return to the center in a short time (Fig. 6.12, brown square) at 340.4 Myr, mixing the matter of the core with the envelope of the star.

The evolution of the hot companion or gainer star is more interesting since the external layer of the star is governed by a thermohaline mixing process, which shows a convective core of $0.67 M_{\odot}$ where around of 10% of the core presents an overshooting mixing process and later 301.3 Myr has an increase in the energy production rate. After mass transfer, the convective core increases its mass reaching a maximum of $1.30 M_{\odot}$, moving the overshooting mixing process the same proportion and increasing its energy generation deeper in the core. The thermohaline region shows an anonymous mixing later at 300 Myr which is controlled by convective layers of the gainer. The main evolutionary stages for both stars are given in Table 6.1.

6.6 Stellar dynamo in the donor star

In this section we have developed a brief analysis about the effects of the magnetic fields in rotating stars. Typically the magnetic field generation by differential rotation has been regarded as a process operating in the convective zone. However, the magnetic fields can be created in stratified layers in differentially rotating stars. Also the convection is not really necessary for a dynamo process to operate if the toroidal field replaces the role of convection as a result of magnetic instability. Hence, the differential rotation is an azimuthal amplification mechanism which stretches the field lined and forms a toroidal field (Spruit, 2002). We have analyzed the magnetic fields generated by the Tayler-Spruit dynamo during three different stages of the system :

- The first stage corresponds to hydrogen depletion to 298.000 Myr ($M_d=3.397 M_{\odot}$, $M_g=3.179 M_{\odot}$).
- During the mass transfer, i.e. up to 301.335 Myr ($M_d=3.395 M_{\odot}$, $M_g=3.181 M_{\odot}$).
- The current stage of the system to 301.763 Myr ($M_d=0.913 M_{\odot}$, $M_g=5.651 M_{\odot}$).

We notice that the Eulerian diffusion coefficient for mixing $D_{Eulerian}$ (Fig. 6.12, yellow line) decreases when it gets close to the limit of the convective mixing zone and remains constant within the overshooting mixing zone at 298.000 Myr. Out of both zones this mechanism stops abruptly, and the elements that exhibit greater diffusivity outside this zone will be transported by advection, i.e., will be transported by the velocity of the fluid causing that the diffusion coefficient gradually

Table 6.1: Evolutive stages for DPV V495 Cen until ^4He depletion of the donor star and their main feautres.

	Stage	Age (Myr)	M (M_{\odot})	R_{\odot}	log T (K)	Ev. Process
Donor						
	Z.A.M.S.	0.000	3.400	2.183	4.116	Zero Age Main Sequence, Hydrogen burning.
	T.A.M.S.	52.370	3.399	2.359	4.111	Terminal age main sequence
	B	298.000	3.397	7.201	3.949	^1H depletion (Sub. giant).
	C	301.250	3.397	6.088	4.018	Increase of luminosity and temperature.
	D	301.335	3.395	7.287	3.955	Mass transfer.
	U_1	301.360	3.288	7.214	3.909	Inversion masses.
	E	301.420	2.732	6.980	3.755	Minimum value Roche lobe (Red giant).
	U_2	301.598	1.089	15.376	3.670	End of optically thick mass transfer.
	F	302.681	0.668	29.269	3.792	End of mass transfer stage.
	G	341.701	0.653	0.225	4.563	^4He depletion (W. D.).
Gainer						
	Z.A.M.S.	0.000	3.180	2.100	4.101	Zero Age Main Sequence
	T.A.M.S.	52.370	3.179	2.236	4.093	Terminal age main sequence
	b	299.000	3.179	4.299	4.011	^1H Enrichment
	c	301.580	5.337	4.203	4.241	End of rejuvenation stage
	d	301.670	5.595	3.671	4.246	Last hydrogen accretion from inner of the disc
	e	302.500	5.866	3.496	4.279	Main Sequence relocation
	f	304.000	5.886	3.773	4.266	^1H re-burning
	g	335.000	5.870	7.924	4.166	Sub giant
	h	337.600	5.867	7.380	4.202	Early horizontal branch
	i	337.826	5.867	78.509	3.620	Red clump
	j	341.701	5.778	145.470	3.573	^4He depletion (A. G. branch)

increase again until almost reaches the original values at the most outer layer of the star. It is possible that this events called advection has been able to mechanically grab a hold of electric charges and force currents to flow, which would leads to generation of seed magnetic field and the presence of magnetic fields outside the convective and overshooting mixing zones (Fig. 6.12, Top), as proposed by Biermann (1950). Thus, the advection has an important role when we deal with about stellar dynamo in the donor star.

Once both magnetic fields are generated, these move towards the convective core and we notice that the toroidal magnetic field dominates the poloidal magnetic field during all the evolution track. Since now the energy is transported by radiation (radiative zone), the ST diffusion coefficient becomes important, allowing the mixing to occur in the radial direction. This coefficient dominates over the Eulerian diffusion coefficient and is related to the poloidal magnetic field in their first moments. The greater variation of the toroidal and poloidal components occurs previous to the mass transfer at the upper limit of the overshooting mixing zone from 0.43 to 1.23 M_{\odot} (Fig. 6.12, center), causing a decrease of the diffusion coefficient ($\text{cm}^2 \text{s}^{-1}$) within of the convective core around of 11.8 units but allowing an increase of the overshooting mixing zone in almost 7 units too. We notice that since the hydrogen depletion until the current stage of V495 Cen, the magnetic fields toroidal and poloidal increased in 1.5 and 1.3 dex respectively (Fig. 6.12, Bottom). The expected toroidal magnetic field strength at the surface of the donor should be between 0 to 100 G and, while the poloidal between 0 to 2000 G. Theses intervals were estimated agree to the magnetic

field strengths found by Leal-Ferreira et al. (2013) and Vlemmings et al. (2005) in evolve and late type stars. We noted that the obtained values close to the surface for the toroidal magnetic field $B_\phi \sim 15$ G and to poloidal magnetic field $B_r \sim 1900$ G are coherent with the expected values.. Also the diffusivity of some elements inhibits the presence of magnetic fields and the appearance of these could be related to the advection, generating magnetic seeds and later the respective magnetic fields.

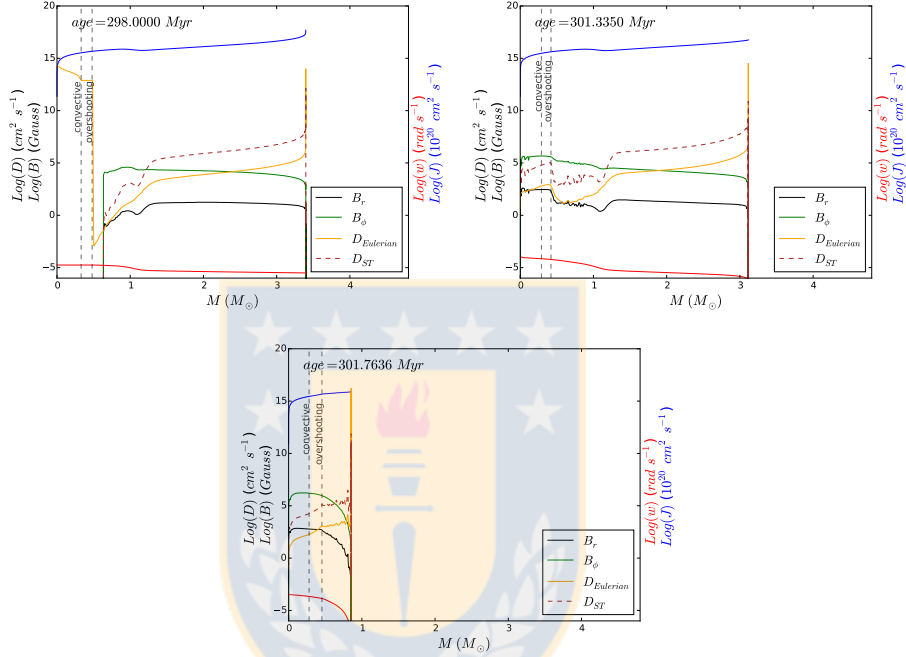


Figure 6.12: Three profiles of the magnetic fields generated by the Tayler-Spruit dynamo in the poloidal (radial) and toroidal (azimuthal) components to the donor star. From top to bottom the profiles are hydrogen depletion, mass transfer and current stage of the system. The Eulerian diffusion coefficient (yellow) out of the convective zone is stopping and allow to the Spruit-Taylor (ST) diffusion coefficient (Brown-dashed) work within radiative zone. The poloidal magnetic field (black) is modeled by the diffusion ST coefficient, while the toroidal magnetic field (green) is dominant as is expected. The angular momentum and velocity are represented in blue and red, respectively.

6.7 Discussion

The Spruit-Taylor dynamo model implemented in MESA, shows how magnetic fields can be produced in a layer outside the convection and overshooting zones. At the same time the rotation and internal movement of the star contribute as an energy source for the process of generating magnetic fields. We know that using a particular dynamo model does not guarantee us to predict the second photometric variability of the DPVs. However, we understood that the presence of magnetic fields

within the donor is definitely justified. Therefore, we try to forecast the magnetic evolution of the DPV using the characteristics of an almost conservative mass transport. The differential rotation can be produced by a torque like a stellar wind or by internal evolution of the star in a certain way correct, and it is the start to produce the first predictive models for DPVs (Schleicher & Mennickent, 2017).

Unfortunately, still we do not know what type of dynamo is most appropriate for these systems, without forgetting the mechanisms that drive their duration and variation of amplitude in the long cycle. Thus it leaves us with the following open question: how do we accurately predict a dynamo solution which describes the second photometric variability of the DPVs? As a potentially useful insight, we notice that the intensity of the magnetic fields at the three different stages computed with our model for V495 Centauri are in agreement with the magnetic field strengths found by Leal-Ferreira et al. (2013) and Vlemmings et al. (2005) in evolve and late type stars.

The main uncertainties associated to our simulations are associated to the initial stellar parameters like masses, orbital period and luminosities. We intended different combinations of these parameters to fit the observed configuration of V 495 Centauri. As the MESA code follows standard and well established stellar evolution theory, the predominant errors come from the observed masses, radii and luminosities, being the orbital period the best determined parameter. On the other hand, the different dynamo models included in the MESA code follow physical prescriptions with relative importance depending on the stellar evolutionary stage. The basic assumption here is the veracity of these prescriptions. The errors associated to the dynamo in MESA are less important compared with the errors associated to the overall evolutionary track (controlled basically by nuclear evolution) and far less than those related to the observed data.

6.8 Conclusions

In this work we have presented a detailed view of the evolutionary stages of the close interacting binary V495 Cen, following the evolution with the code MESA. We also compared the results of this evolutionary route with the published parameters of the binary, finding the best representative model. The main results of our research are:

- The model suggests that the orbital period is stable during the evolution as single stars, until the primary star fills the Roche lobe, causing an abrupt variation and increase during the mass transfer process.
- The Donor star shows a maximum of its spin-up during the end phase of the optically thick mass transfer and the model confirmed that the rejuvenation of the gainer star is principally produced by mass transfer.
- The hydrogen enrichment on the gainer star causes rejuvenation of the accretor and a relocation within the main sequence. This process causes the gainer to be more massive and compacted than expected for a star of the same mass.
- The luminosity of the donor decreases one order of magnitude during 0.18 Myr, due that the deeper layers need expand for adjusting quickly the mass lost, while the gainer star increases the temperature by 10000 K, causing an increase of one order of magnitude of the luminosity, but both processes are not related to the DPV second photometric variation.
- The central density of the donor increases gradually between mass transfer (D) and the end of the optically thick mass transfer (U_2).

- Outside of convective and overshooting mixing zones, the advection has an important role on the generation of currents mechanic, probably causing the generation of seed magnetic field and the appearance of magnetic fields within of donor star. Therefore the convection is not necessary for the generation of the stellar dynamos.
- The best model, indicate that the DPV V495 Cen is found with age 301.7636 Myr, $M_d = 0.913 M_\odot$ and $M_g = 5.651 M_\odot$, and is the result of the evolution and mass transfer of two stars of initial masses $M_{i,d} = 3.40 M_\odot$ and $M_{i,g} = 3.18 M_\odot$ and initial orbital period 3.9 days.
- Since most DPVs have an early B-type gainer and a A/F/G giant donor, they probably follow similar evolutionary routes starting with a pair of main sequence, intermediate mass stars, orbiting the center of mass in few days, for evolving into a semidetached configuration after the evolution and radius increase of the initially more massive component (Mennickent et al., 2016). This work suggests that the case study of V 495 Cen can be observed as representative for the enter population of DPVs, or at least, for most of these systems.





Chapter 7

Conclusions

This thesis aimed to perform various photometric, spectroscopic and numerical modeling analyzes in three Galactic DPV stars. Through of a photometric analysis these DPV was determined that each one corresponds to different orbital periods respectively. The first system is DD CMa and belongs to the lower boundary of the orbital period, the HD 50526 is located in the central group, while V495 Cen belongs to the upper boundary of the orbital period. Wherein we determined their ephemeris, and disentangled the long and sub-orbital cycles in each case respectively. Through high resolution spectroscopic analysis, we obtained the orbital and fundamental parameters of each system, allowing us to characterize and explain in detail their current evolutionary processes. Using the stellar evolution code MESA, and the orbital and fundamental parameters obtained in each system, we have numerically modeled the DPV with the more larger orbital period, in order to explain the most number of mechanisms and evolutionary processes related to the life of a DPV. The individual conclusions of each study were summarized at the end of each chapter. Therefore in this section a general conclusion of this thesis will be delivered.

Table 7.1: Results of mass/radius ratio of three different DPVs at their current stage respectively.

	DD CMa	err	HD 50526	err	V495 Cen	err
P_o (d)	2.008	0.000	6.701	0.001	33.492	0.002
a (R_\odot)	13.610	0.100	28.500	0.020	82.800	0.300
M_h (M_\odot)	6.600	0.070	5.860	0.020	5.760	0.300
M_c (M_\odot)	1.810	0.006	1.050	0.020	0.910	0.200
R_d (R_\odot)	5.400	0.100	14.900	0.020	40.200	1.300
$\left(\frac{M_d}{R_d}\right)_c$	1.988	0.520	1.655	0.150	1.280	0.880

- While we was inspecting the ASAS Catalogue, we found a group of blue variable stars belonging to the Milky Way, of which the most of them were re-cataloged as Double Periodic Variables stars and we have increased by 5 the number of DPVs known to date. These are binary stars showed a second photometric variability, wherein the second cycle was easily observed at the photometric data as function of the Heliocentric Julian Days (HJD). The Double Periodic Variables DD CMa with an extreme short period of 2.0084 ± 0.0001 d and V495 Cen with a long orbital period of 33.492 ± 0.002 d, allow us redefine the range of

orbital periods of these systems, wherein the long cycle is in average ~ 33 times larger than the orbital period (see eq. 7.1) but with a lower limit of 28 and an upper limit of 44 times larger than the orbital period and their orbital periods run between 2.0084 to 100 days, see equation 7.1:

$$P_l \approx 33_{-5}^{+11} P_o \quad (7.1)$$

- A relevant factor to discuss the mass loss is the evidence of close nebulosity around a binary system. Unfortunately the analyzed DPVs did not presented evidence of nebulosity when these were analyzed using the WISE image survey.
- The binary systems: UX Cnc, TYC 6083-192-1, TYC 8638-2548-1, the year 2014 were cataloged as Double Periodic Variable. However these were re-cataloged as RS Canum Venaticorum-type binary systems, due to the nature of their very long periods, comparable with the time baseline, their small long-cycle amplitudes and the very red color by (Mennickent et al., 2016).
- The enigmatic TYC 5353-1137-1 is other binary system that belong to the group DPV of shortest orbital periods. Its orbital period is of 2.028 d and the long period of 60.455 d. This system shown a semiregular amplitude of the light curve and when it was phased using the orbital period at three photometric datasets, apparently was observed an effect of switch off-on of the long cycle, whose effect was observed for first time in these type of systems. This DPV is an optimal target to perform a spectropolarimetry study and understand the mechanism based on cycles of magnetic dynamo in the donor star.
- From the equivalent width analysis performed on the $H\alpha$ profile for the DPV DD CMa, we noted a cyclical variation of $0.5P_o$ orbital period with mean $19.4229 \pm 4.805 \text{ \AA}$ and an amplitude of $21.4656 \pm 6.433 \text{ \AA}$, which reinforces the hypothesis of cyclic variation on the structure of the accretion disk proposed by Garcés L et al. (2018).
- The following three DPV-stars; DD CMa, HD 50526, V495 Cen are in a semi-detached stage, wherein the more evolved component start the mass transfer toward the hotter companion through the Lagrange point L_1 , principally by Roche Lobe Over Flow (RLOF). Every one formed an concave and geometrically thick accretion disk surround the hot star, whose size depends of primary radius, orbital separation and the initial mass ratio.
- The models of HR diagram developed with MESA code for HD 50526 and V495 Cen, showed that during the accretion mass the gainer star presents a rejuvenation stage and its evolution track was relatively parallel to the main sequence. However, the system V495 Cen at the end of the optically thick mass transfer, the gainer star continue accreting material, principally hydrogen from the disc and start a return and this relocate within main sequence but with a greater mass and orbital velocity than the initial one. At this stage we propose that the DPV is a precursors of an early-type Be star or of a rapidly rotating massive stars.
- For the case of V495 Cen, once that onset the mass ratio inversion, the gainer star has created a hot spot on the edge of the accretion disk. During this moment the donor star moves to the minimum value of the Roche lobe and the thermohaline process dominates to the new star that presents a decreased convective core. Later, the spin-up of the gainer and the orbital period of the system has increased until reach a maximum value. Finally, when the donor star arrive to end of the phase of optically thick mass transfer the gainer onset a process of

decrease of the spin-up until reach the rotational stability. Therefore, we confirms that the mass transfer is the principal mechanism related to the spin-up of the gainer star together to the decrease of the convective core of the donor star.

- As we well know the B type stars have not corona and lack of a convective layer in outer, causing great mass loss by strong winds. Also, we know that their energy generation is concentrated at the core, which mean that the convection zone is close to th core, is for this reason that the life of these star is relatively short of a few million or tens of million years. The performed model with MESA for V495 Cen shown that the convective core of the gainer increase its size almost the double during and post mass transfer. This would provoke a decrease at the mass loss by winds in the outer zones of the star, causing a constant mixing between the hydrogen and Helium due to the nuclear fusion. Thus, the mechanism of mass transfer would increase the life of the B-type star and would challenge all kinds of logic with respect to the evolutionary life of a single B-type star and could be the reason why always the accretor maintains its spectral type. We must emphasize that the oldest stars are convective-type.
- The masses of single B dwarf stars of the main sequence run between 3.29 to $17 M_{\odot}$ and their radii between 2.7 to $10.0 R_{\odot}$ approximately and their M/R ratio always is greater than 1 [Silaj et al. \(2014\)](#). From our model developed with MESA both for HD 50526 and V495 Cen, we noted that the mass transfer \dot{M} , is directly related with the M/R ratio and we noted that this relationship M/R is greater when the orbital period is of few days while that for orbital periods of some tens days it decrease.
- At the model for V495 Cen, outside of convective and overshooting mixing zones of the donor star, the advection has an important role to generate currents mechanic, generating magnetic seeds field and the appearance of magnetic fields within of the donor star. Therefore, we thought that is a partial evidence to relate the long cycle of V495 Cen with magnetic dynamo cycles of a donor star.



Bibliography

- Applegate, J. H., & Patterson, J. 1987, *apjl*, 322, [L99](#)
- Baker, N., & Kippenhahn, R. 1959, *zap*, 48, [140](#)
- Baliunas, S. L., Nesme-Ribes, E., Sokoloff, D., & Soon, W. H. 1996, *apj*, 460, [848](#)
- Barría, D., Mennickent, R. E., Schmidtobreick, L., et al. 2013, *A&A*, 552, [A63](#)
- Barría, D., Mennickent, R. E., Graczyk, D., & Kołaczkowski, Z. 2014, *A&A*, 567, [A140](#)
- Bayo, A., Rodrigo, C., Barrado Y Navascués, D., et al. 2008, *A&A*, 492, [277](#)
- Bloeker, T. 1995, *aap*, 297, [727](#)
- Biermann, L. 1950, *Zeitschrift Naturforschung Teil A*, 5, [65](#)
- Bisikalo, D. V., Boyarchuk, A. A., Chechetkin, V. M., Kuznetsov, O. A., & Molteni, D. 1998, *mnras*, 300, [39](#)
- Bisikalo, D. V., Boyarchuk, A. A., Chechetkin, V. M., Kuznetsov, O. A., & Molteni, D. 1999, *Astronomy Reports*, 43, [797](#)
- Bisikalo, D. V., Boyarchuk, A. A., Kaigorodov, P. V., & Kuznetsov, O. A. 2003, *Astronomy Reports*, 47, [809](#)
- Budaj, J. 2011, *aj*, 141, [59](#)
- Burger, H. L., & Katz, J. I. 1983, *apj*, 265, [393](#)
- Caleo, A., Balbus, S. A., & Tognelli, E. 2016, *mnras*, 460, [338](#)
- Cardelli, J. A., Clayton, G. C., & Mathis, J. S. 1989, *Interstellar Dust*, 135, [5](#)
- Castelli, F., & Kurucz, R. L. 2004, [arXiv:astro-ph/0405087](#)
- Charbonneau, P. 1995, *ApJS*, 101, [309](#)
- Charbonneau, P. 2013, *Solar and Stellar Dynamos: Saas-Fee Advanced Course 39 Swiss Society for Astrophysics and Astronomy, Saas-Fee Advanced Courses, Volume 39*. ISBN 978-3-642-32092-7. Springer-Verlag Berlin Heidelberg, 2013, [39](#)
- Charbonnel, C., & Zahn, J.-P. 2007, *aap*, 476, [L29](#)
- Clausen, J. V. 2004, *nar*, 48, [679](#)

- Deschamps, R., Braun, K., Jorissen, A., et al. 2015, *A&A*, 577, [A55](#)
- Djurašević, G. 1996, *Ap&SS*, 243, [413](#)
- Djurašević, G. 1992, *Ap&SS*, 197, [17](#)
- de Jager, C., Nieuwenhuijzen, H., & van der Hucht, K. A. 1988, *aaps*, 72, [259](#)
- de Mink, S. E., Sana, H., Langer, N., Izzard, R. G., & Schneider, F. R. N. 2014, *apj*, 782, [7](#)
- Eggenberger, P., Meynet, G., Maeder, A., et al. 2010, *aap*, 519, [A116](#)
- Eggleton, P. P. 1971, *mnras*, 151, [351](#)
- Eggleton, P. P. 1983, *apj*, 268, [368](#)
- Eggleton, P. 2006, *Evolutionary Processes in Binary and Multiple Stars*, by Peter Eggleton, pp. . ISBN 0521855578. Cambridge, UK: Cambridge University Press, [2006](#)
- Ekström, S., Georgy, C., Eggenberger, P., et al. 2012, *A&A*, 537, [A146](#)
- Fitzpatrick, E. L., & Massa, D. 2005, *aj*, 130, [1127](#)
- Fitzgerald, M. P. 1970, *A&A*, 4, [234](#)
- Flower, P. J. 1996, *apj*, 469, [355](#)
- Frank, J., King, A., & Raine, D. J. 2002, *Accretion Power in Astrophysics*, by Juhan Frank and Andrew King and Derek Raine, pp. 398. ISBN 0521620538. Cambridge, UK: Cambridge University Press, February 2002., [398](#)
- Fricke, K. 1968, *zap*, 68, [317](#)
- Garcés L, J., Mennickent, R. E., Djurašević, G., Poleski, R., & Soszyński, I. 2018, *mnras*, 477, [L11](#)
- Garrido, H. E., Mennickent, R. E., Djurašević, G., et al. 2013, *mnras*, 428, [1594](#)
- Glebbeeck, E., Gaburov, E., de Mink, S. E., Pols, O. R., & Portegies Zwart, S. F. 2009, *aap*, 497, [255](#)
- Goldreich, P., & Schubert, G. 1967, *apj*, 150, [571](#)
- González, J. F., & Levato, H. 2006, *A&A*, 448, [283](#)
- Heger, A., Langer, N., & Woosley, S. E. 2000, *apj*, 528, [368](#)
- Heger, A., Woosley, S. E., & Spruit, H. C. 2005, *apj*, 626, [350](#)
- Herbig, G. H. 1993, *apj*, 407, [142](#)
- Hilditch, R. W. 2001, *An Introduction to Close Binary Stars*, by R. W. Hilditch, pp. 392. ISBN 0521241065. Cambridge, UK: Cambridge University Press, March 2001., [392](#)
- Houk, N. 1978, *Ann Arbor : Dept. of Astronomy, University of Michigan : distributed by University Microfilms International*, [1978](#)
- Iben, I., Jr. 1967, *ARA&A*, 5, [571](#)

- Jetsu, L., & Porceddu, S. 2015, PLoS ONE, [10](#)
- Jones, C. A. 2008, Course 2 Dynamo theory, 88, [45](#)
- Kato, S. 1966, pasj, 18, [374](#)
- Kippenhahn, R., & Weigert, A. 1967, zap, 65, [251](#)
- Kippenhahn, R. 1974, Late Stages of Stellar Evolution, 66, [20](#)
- Kippenhahn, R., Weigert, A., & Weiss, A. 2012, Stellar Structure and Evolution: , Astronomy and Astrophysics Library. ISBN 978-3-642-30255-8. Springer-Verlag Berlin Heidelberg, [2012](#)
- Kolb, U., & Ritter, H. 1990, A&A, 236, [385](#)
- Lauterborn, D. 1970, aap, 7, [150](#)
- Leal-Ferreira, M. L., Vlemmings, W. H. T., Kembell, A., & Amiri, N. 2013, aap, 554, [A134](#)
- Lebreton, Y., Montalbán, J., Godart, M., et al. 2009, Communications in Asteroseismology, 158, [277](#)
- Lucy, L. B., & Sweeney, M. A. 1971, AJ, 76, [544](#)
- Lucy, L. B. 1967, zap, 65, [89](#)
- Maeder, A. 2009, Physics, Formation and Evolution of Rotating Stars: , Astronomy and Astrophysics Library. ISBN 978-3-540-76948-4. Springer Berlin Heidelberg, [2009](#)
- Martin, P. G., & Whittet, D. C. B. 1990, apj, 357, [113](#)
- Meakin, C. A., & Arnett, D. 2007, apj, 667, [448](#)
- Meintjes, P. J. 2004, mnras, 352, [416](#)
- Mennickent, R. E., Schleicher, D. R. G., & San Martín-Pérez, R. 2018, pasp, 130, [094203](#)
- Mennickent, R. E. 2017, Serbian Astronomical Journal, 194, [1](#)
- Mennickent, R. E., Otero, S., & Kołaczowski, Z. 2016, mnras, 455, [1728](#)
- Mennickent, R. E., Zharikov, S., Cabezas, M., & Djurašević, G. 2016, mnras, 461, [1674](#)
- Mennickent, R. E., Djurašević, G., Cabezas, M., et al. 2015, Living Together: Planets, Host Stars and Binaries, 496, [175](#)
- Mennickent, R. E., Djurašević, G., Cabezas, M., et al. 2015, mnras, 448, [1137](#)
- Mennickent, R. E., Djurašević, G., Cabezas, M., et al. 2015, New Windows on Massive Stars, 307, [125](#)
- Mennickent, R. E. 2014, pasp, 126, [821](#)
- Mennickent, R. E., & Rosales, J. 2014, Information Bulletin on Variable Stars, 6116, [1](#)
- Mennickent, R. E. 2013, Central European Astrophysical Bulletin, 37, [41](#)
- Mennickent, R. E., & Djurašević, G. 2013, mnras, 432, [799](#)

- Mennickent, R. E., & Rosales, J. 2014, *Information Bulletin on Variable Stars*, 6116, [1](#)
- Mennickent, R. E., Djurašević, G., Kołaczkowski, Z., & Michalska, G. 2012, *mnras*, 421, [862](#)
- Mennickent, R. E., Kołaczkowski, Z., Djurašević, G., Diaz, M., & Niemczura, E. 2012, *From Interacting Binaries to Exoplanets: Essential Modeling Tools*, 282, [317](#)
- Mennickent, R. E., Kołaczkowski, Z., Djurasevic, G., et al. 2012, *mnras*, 427, [607](#)
- Mennickent, R. E., Kołaczkowski, Z., Graczyk, D., & Ojeda, J. 2010, *mnras*, 405, [1947](#)
- Mennickent, R. E., & Kołaczkowski, Z. 2009, *Revista Mexicana de Astronomia y Astrofisica Conference Series*, 35, [166](#)
- Mennickent, R. E., Kołaczkowski, Z., Michalska, G., et al. 2008, *mnras*, 389, [1605](#)
- Mennickent, R. E., Pietrzyński, G., Diaz, M., & Gieren, W. 2003, *A&A*, 399, [L47](#)
- Nieuwenhuijzen, H., & de Jager, C. 1990, *aap*, 231, [134](#)
- Nugis, T., & Lamers, H. J. G. L. M. 2000, *aap*, 360, [227](#)
- Paczynski, B., & Proszynski, M. 1986, *apj*, 302, [519](#)
- Pawlak, M., Graczyk, D., Soszyński, I., et al. 2013, *actaa*, 63, [323](#)
- Paxton, B. 2004, *pasp*, 116, [699](#)
- Paxton, B., Bildsten, L., Dotter, A., et al. 2011, *apjs*, 192, [3](#)
- Paxton, B., Cantiello, M., Arras, P., et al. 2013, *apjs*, 208, [4](#)
- Paxton, B., Marchant, P., Schwab, J., et al. 2015, *apjs*, 220, [15](#)
- Paxton, B., Schwab, J., Bauer, E. B., et al. 2018, *apjs*, 234, [34](#)
- Peterson, W. M., Mutel, R. L., Güdel, M., & Goss, W. M. 2010, *nat*, 463, [207](#)
- Pickering, E. C. 1890, *mnras*, 50, [296](#)
- Prialnik, D., & Kovetz, A. 1995, *apj*, 445, [789](#)
- Pojmanski, G. 1997, *AcA*, 47, [467](#)
- Poleski, R., Soszyński, I., Udalski, A., et al. 2010, *AcA*, 60, [179](#)
- Rafert, J. B., & Twigg, L. W. 1980, *mnras*, 193, [79](#)
- Regev, O., Umurhan, O. M., & Yecko, P. A. 2016, *Modern Fluid Dynamics for Physics and Astrophysics*. Series: Graduate Texts in Physics, ISBN: ISBN 978-1-4939-3163-7/ISBN. Springer New York (New York, NY), Edited by Oded Regev, Orkan M. Umurhan and Philip A. Yecko,
- Reimers, D. 1975, *Memoires of the Societe Royale des Sciences de Liege*, 8, [369](#)
- Rosales Guzmán, J. A., Mennickent, R. E., Djurašević, G., Araya, I., & Curé, M. 2018, *mnras*, 476, [3039](#)
- Rosales, J. A., Mennickent, R. E. 2018, *Information Bulletin on Variable Stars*, 6248, [1](#)

- Rosales G., J., & Mennickent, R. E. 2017, *Information Bulletin on Variable Stars*, 6207, [1](#)
- Ruciński, S. M. 1969, *actaa*, 19, [245](#)
- Sarna, M. J., Muslimov, A., & Yerli, S. K. 1997, *mnras*, 286, [209](#)
- Schleicher, D. R. G., & Mennickent, R. E. 2017, *aap*, 602, [A109](#)
- Schaller, G., Schaerer, D., Meynet, G., & Maeder, A. 1992, *A&AS*, 96, [269](#)
- Schlafly, E. F., & Finkbeiner, D. P. 2011, *Apj*, 737, [103](#)
- Schlegel, D. J., Finkbeiner, D. P., & Davis, M. 1998, *Apj*, 500, [525](#)
- Silaj, J., Jones, C. E., Sigut, T. A. A., & Tycner, C. 2014, *apj*, 795, [82](#)
- Soberman, G. E., Phinney, E. S., & van den Heuvel, E. P. J. 1997, *aap*, 327, [620](#)
- Soderhjelm, S. 1980, *aap*, 89, [100](#)
- Soon, W. H., Baliunas, S. L., & Zhang, Q. 1993, *apjl*, 414, [L33](#)
- Spruit, H. C. 2002, *aap*, 381, [923](#)
- Stellingwerf, R. F. 1978, *apj*, 224, [953](#)
- Tassoul, J.-L. 2000, *Stellar rotation / Jean-Louis Tassoul*. Cambridge ; New York : Cambridge University Press, 2000. (Cambridge astrophysics series ; 36)
- Tassoul, J.-L. 1978, *Princeton Series in Astrophysics*, Princeton: University Press, [1978](#)
- Tauris, T. M., & van den Heuvel, E. P. J. 2006, *Compact stellar X-ray sources*, 39, [623](#)
- Tout, C. A., & Hall, D. S. 1991, *mnras*, 253, [9](#)
- Torres, G. 2010, *aj*, 140, [1158](#)
- Ulrich, R. K. 1972, *apj*, 172, [165](#)
- van Rensbergen, W., De Greve, J. P., De Loore, C., & Mennekens, N. 2008, *VizieR Online Data Catalog*, [348](#)
- van Rensbergen, W., de Greve, J. P., Mennekens, N., Jansen, K., & de Loore, C. 2011, *aap*, 528, [A16](#)
- van Rensbergen, W., De Greve, J. P., De Loore, C., & Mennekens, N. 2008, *A&A*, 487, [1129](#)
- Vauclair, S. 2008, *The Art of Modeling Stars in the 21st Century*, 252, [97](#)
- Vink, J. S., de Koter, A., & Lamers, H. J. G. L. M. 2001, *aap*, 369, [574](#)
- Vlemmings, W. H. T., van Langevelde, H. J., & Diamond, P. J. 2005, *aap*, 434, [1029](#)
- von Zeipel, H. 1924, *mnras*, 84, [665](#)
- Wasiutynski, J. 1946, *Astrophysica Norvegica*, 4, [1](#)
- Wright, E. L., Eisenhardt, P. R. M., Mainzer, A. K., et al. 2010, *aj*, 140, [1868](#)

Woods, T. E., Ivanova, N., van der Sluys, M. V., & Chaichenets, S. 2012, *apj*, 744, 12

Zahn, J.-P. 1992, *aap*, 265, 115

Zahn, J.-P. 1977, *A&A*, 57, 383

Zahn, J.-P. 1975, *A&A*, 41, 329



Curriculum Vitae



Jaime A. Rosales Guzmán
jrosales@astro-udec.cl

Jaime Rosales was born July 21th of 1982 at commune of Providencia, Santiago of Chile. The year 2009 he moved to Concepción city, where he later on began his studies at the Universidad de Concepción. He obtained his Bachelor in Astronomy (December 2013), the next year he completed the requirements to become a Professional Astronomer (similar to Master's degree). The year 2015 he started a PhD at the Universidad de Concepción under supervision of Dr. Ronald Mennickent Cid, wherein he wrote his Doctoral thesis titled “Double Periodic Variable stars: a challenging to evolutionary process of close binary stars”. Currently he is working with new DPV stars and numerical modeling while waiting for a Postdoctoral position at the University of Cambridge.

7.1 List of publications

- Mennickent, R. E., & Rosales, J. **2014**, Information Bulletin on Variable Stars, 6116, **1**

- Mennickent, R. E., Djurašević, G., Cabezas, M., et al. **2015**, *New Windows on Massive Stars*, 307, [125](#)
- Mennickent, R. E., Djurašević, G., Cabezas, M., et al. **2015**, *mnras*, 448, [1137](#)
- Mennickent, R. E., Djurasevic, G., Cabezas, M., et al. **2015**, *Living Together: Planets, Host Stars and Binaries*, 496, [175](#)
- Rosales G., J., & Mennickent, R. E. **2017**, *Information Bulletin on Variable Stars*, 6207, [1](#)
- Mennickent, R. E., Djurasevic, G., Cabezas, M., et al. **2017**, *VizieR Online Data Catalog*, [744](#)
- Rosales Guzmán, J. A., Mennickent, R. E., Djurašević, G., Araya, I., & Curé, M. **2018**, *mnras*, 476, [3039](#)
- Rosales, J. A., Mennickent, R. E. **2018**, *Information Bulletin on Variable Stars*, 6248, [1](#)
- an Martín-Pérez, R. I., Schleicher, D. R. G., Mennickent, R. E., & Rosales, J. A. **2018**, [arXiv:1812.01669](#)
- Rosales, J. A., Mennickent, R. E., Schleicher, D. R. G., & Senhadji, A. A. **2019**, *mnras*, 483, [862](#)

Upcoming publications (A1)

- Rosales et al., Mennickent, R. E, Djurasevic, G. **2018**: Analyzing the long term variability of the hot Algol HD 50526 (sent)
- Rosales et al., Mennickent, R. E, Djurasevic, G. **2018**: A new sub-orbital period in DD CMA with partial evidence of accretion disk (In preparation)

Conferences attended

- Rosales, J. R. E. Mennickent, 2012, SOCHIAS, Viña del Mar, Chile: Photometric search of disks around DPV stars (Oral contribution).
- Rosales, J. R., 2014, Herbig Ae/Be stars workshop, ESO & RAS, Santiago, Chile (Participant).
- Rosales, J., 2015, 22th Young Scientists' Conference on Astronomy and Space Physics (YSC), Kiev, Ukraine: Photometric search for new DPVs using ASAS's Catalogue and Spectroscopic Analysis with CHIRON (Oral contribution).
- Rosales, J., 2015, SOCHIAS, Puerto Varas, Chile: Photometric search for new DPVs using ASAS's Catalogue (Poster).
- Rosales, J. et al., 2016, 23th Young Scientists' Conference on Astronomy and Space Physics (YSC), Kiev, Ukrain: Spectroscopic study of the system V495 Centauri (Oral contribution).
- Rosales, J. A. et al., 2018, 25th Young Scientists' Conference on Astronomy and Space Physics (YSC), Kiev, Ukraine: Analyzing the long term variability of the Double Periodic Variable HD 50526 (Oral contribution).

- Rosales, J. A. et al., 2018, 25th Young Scientists' Conference on Astronomy and Space Physics (YSC), Kiev, Ukraine: Evolutionary process of the Double Periodic Variable V495 Centauri (Oral contribution).
- Rosales, J. A. et al., 2018, SOCHIAS, La Serena, Chile: Analyzing the long term variability of the Double Periodic Variable HD 50526 (Oral contribution).
- Rosales, J. A. et al., 2018, SOCHIAS, La Serena, Chile: Evolutionary process of the Double Periodic Variable V495 Centauri (Poster).

Summer schools attended

- ESO/NEON Observing School at La Silla, 2016, Santiago - La Serena, Chile: summer school of astronomical observation, reduction and data analysis.
- MESA Summer School, 2017, Santa Bárbara, University of California (UCSB), United States: summer school of numerical modeling of stellar evolution.

